ULTRAFAST ANTIFERROMAGNETIC SPIN DYNAMICS IN HIGH MAGNETIC FIELDS

IRINA DOLGIKH

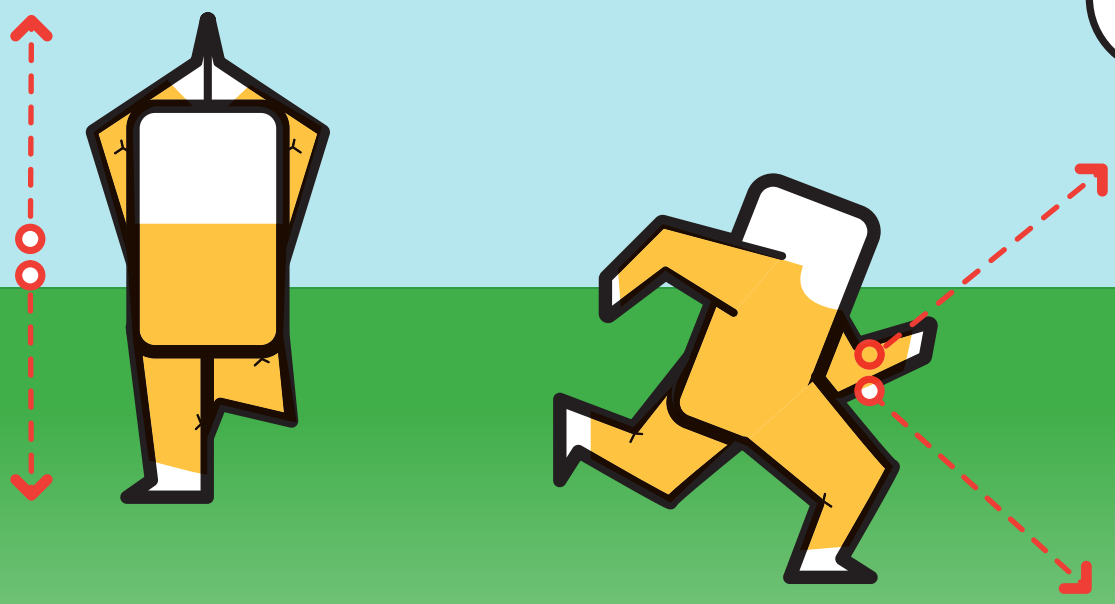

Institute for Molecules and Materials

RADBOUD UNIVERSITY PRESS

Radboud Dissertation Series

Ultrafast antiferromagnetic spin dynamics in high magnetic fields

Irina Dolgikh

The work described in this dissertation was carried out at the Faculty of Science of the Radboud University Nijmegen and is partly financed by the Dutch Organisation for Scientific Research (NWO).

Author: Irina Dolgikh
Title: Ultrafast antiferromagnetic spin dynamics in high magnetic fields

Radboud Dissertations Series
ISSN: 2950-2772 (Online); 2950-2780 (Print)

Published by RADBOUD UNIVERSITY PRESS
Postbus 9100, 6500 HA Nijmegen, The Netherlands
www.radbouduniversitypress.nl

Design: Proefschrift AIO | Irina Dolgikh
Cover: Proefschrift-aio.nl | Guus Gijben
Printing: DPN Rikken/Pumbo

ISBN: 9789465150192
DOI: 10.54195/9789465150192
Free download at:
www.boekenbestellen.nl/radboud-university-press/dissertations

RADBOUD
UNIVERSITY
PRESS

Ultrafast antiferromagnetic spin dynamics in high magnetic fields

Proefschrift ter verkrijging van de graad van doctor
aan de Radboud Universiteit Nijmegen
op gezag van de rector magnificus prof. dr. J.M. Sanders,
volgens besluit van het college voor promoties
in het openbaar te verdedigen op

dinsdag 3 december 2024
om 12:30 uur precies

door

Irina Alexeevna Dolgikh
geboren op 3 mei 1994
te Kazan, Rusland

Promotoren:
prof. dr. A.V. Kimel
prof. dr. P. C. M. Christianen

Manuscriptcommissie:
prof. dr. A.I. Kirilyuk
prof. dr. C. Ciccarelli (University
of Cambridge, Verenigd Koninkrijk)
prof. dr. ir. P.H.M. van Loosdrecht
(Universität zu Köln, Duitsland)

To the memory of my grandfather Nickolay Zamega who first supported and mentored me on the path to physics and lifelong learning.

Preface

This was a long journey full of ups and downs, as in many PhD trajectories. The path to science is a path to the unknown, just like it was in the era of geographical discoveries. The footprints that we make here can lead others further, bringing us closer to understanding nature.

I found it important to think about the contribution to the science that is made. And even if you are not the one who made a final step, it is already great to just go and try, even if it does not work out in the end.

The book that you are holding in your hands, dear reader, was written by me but realized due to the combined efforts of multiple people. Some of them were participating in the conduction of the experiments, some in discussions, some in the theoretical background of the findings, some in storytelling and writing, and some in emotional support. Ultimately, all these people made this book possible. It can be exhaustive to mention everyone as these are two large scientific groups: Ultrafast Spectroscopy of Correlated Materials and High Magnetic Field Laboratory. However, I would like to thank the people who have had the most substantial impact on me during this path.

First of all, I want to thank my supervisors, Alexey and Peter. I'm really happy to finally be writing this acknowledgement to both of you as part of my thesis.

Alexey, thank you for believing in me and giving me the chance to work with you. It took me a while to understand your vision and way of working, but it has helped me grow so much as a researcher. Your guidance has made me more confident and independent, and your dedication to our group has been inspiring. We've all learned a lot from you about how to overcome challenges and achieve our goals. I also really appreciate your constant enthusiasm and all the time you spent helping me improve my writing, even when it was challenging!

Peter, I'll always remember your positive attitude and how easy it became to come to you for help this past year. Your advice and tips were super helpful and very scrupulous, and our discussions always made things clearer. You have a good skill in noticing even small details. It helped not only in interpreting results but also in finding all typos in this thesis. Thank you for being so supportive and for asking good questions.

I'm so grateful to both of you for all your support and for everything

you've done to help me grow and complete this thesis.

Let us move to those who were sitting with me on the night shifts, troubleshooting when I was stuck, gave me a hand and winked when frustration was coming. To colleagues and friends all-in-one. I'm grateful to every single group member and the atmosphere you were creating.

When I got to Nijmegen, it was not easy to find an apartment. Gladly, the group has Marilou. She helps with literally everything above research. The kindest woman with a wide smile and a big heart. Thank you! However, before the very first option was available for me and my husband, our colleague Eugene Mashkovich took us in at his home for a week. Now, after years, he is one of our best friends and we were bringing up our kids together. Thank you for being a great person, a deep thinker, and a sensible experimenter, whom people can easily ask for advice.

On my first working day, I joined the night shift of Anna Pogrebna, Kiran Prabhakara and Fabio Formisano. It was also Halloween night, and Anna came dressed in a costume and treated us with some snacks. This is the way she is. Enthusiastic and cheerful. And she always managed to radiate this wherever she went. In addition to that, I also enjoyed our board game sessions, which sometimes lasted until the morning just like the experiments.

Kiran is a very thorough and diplomatic person. I was extremely grateful to him for being like that at my first magnet time. Kiran, I would definitely have been stressed without your presence there. Also, thank you for explaining to me the way of carrying out the experiments combined with magnet installation. And for being there to guide us if necessary even when you were finalizing your thesis. Which is quite tough, because it meant not sleeping at nights again.

When you hear someone's ironic Italian voice in the lab, you should know that it is Fabio. And despite it being impossible not to have disputes with him, I have to admit it was fun working with him. I'll always remember his signature wink and how easily he handles challenges and moves on.

I choose an office with very positive people. Easy-going and sensible person Anna Gatilova has become my best friend. Due to her tips and tricks, I quickly delved into group flow, experimental procedures, and analysis. Thank you for giving me a starter boost at this time.

Another shiny smile in our office was Guido Bonfiglio. You were the one I took my first cryogenic lessons from and after office some climbing ones. I would like to thank Chris Szerenos for his deep philosophy that I wasn't even able to fully grasp at the early stage of my PhD.

Not only my office, but the whole SSI-USCM group was full of good people, ready to help. Kshiti Mishra together with Kiran were the first to take me for lunch. Later on, I always enjoyed her company for her wittiness and visibility. Kirill Grishunin was the person I always called when something went wrong and I couldn't figure out why. Thank you,

Kirill, for being so supportive - it really matters. I'll never forget calling you late in tears over a broken balanced detector. I was upset because it was the second detector that had been damaged in my hands in a short time. You even came to the university to calm me down. It was such a relief to discover it was an electrical problem and not my fault. I often relied on your deep knowledge of electrical engineering, and I cannot imagine handling these things without you.

One day Qiao Li shared a FeRh sample with me so that I could measure something for his paper. Back then he said that he has more of them and who knows maybe I'll build my PhD on it. I was laughing thinking that it was less probable... Qiao, I heard about research on the existence of extrasensory abilities. You definitely should participate as a volunteer! So, thank you also for being easily addressable in the lab, for your help with the paper, for being so calm and confident during our magnet time and for the wisdom of an old man that you have got for some unknown reason. Thanks to you and later on also to your wife Xinyue Li for organising events for us. Xinyue, you are a very open and active person, and also a responsible researcher. I am grateful for the time I've spent with you and for your support and understanding.

Iliya Razdolskii, we have common roots (the bachelor and master lab) and it was a pleasant surprise to meet during my PhD path a person that I heard legends of during my master's studies.

Thomas Blank, you surprised me with your dedication and intelligence. Thank you for keeping me alive and pushing me to go on at our magnet time when I was close to collapsing.

Timur Gareev, I was happy to realise that I found a board game mate in you. Thank you for your infectious laughter and navigation skills in Venice. The last one partially applies to Thomas Metzger. Thank you guys for that fun journey!

Nickolay Khokhlov, it took me some time to find the right words to thank you. Maybe because there are so many reasons and also because you became my friend even before you joined the group. I was just happy you did join us despite the unpleasant circumstances. Of course, I also appreciate your high expertise in the field, which you readily share with others.

One more boost for the group was Dima Afanasiev. I got to know you a few years before it happened and admired your enthusiasm. Now it has grown even more (how is that possible?) and reached an unprecedented scale. Thank you for fruitful discussions as well.

I would like to also thank Dinar Khusyainov, Lucas van Gerven, Victoriia Radovskaia and Vlad Bilyk.

I would like to thank the technicians for their patience, accessibility and assistance. Sergey Semin, thank you for doing everything by the book and being strict about the rules in the lab. Chris Berkhout, thank you for your

sense of humor and help with cryogenics. Kamyar Saeedi, you are a very good addition to that team as far as I noticed. Thank you for your work.

Peter Alberts, in addition to optics, you used to help me search for something throughout the whole building quite often. Special appreciation for photoshoots with the magnet and for my CV (also for this thesis). And just for being a person to whom you come with a smile despite having a technical problem. The same feeling I had approaching Lijnis Nelemans. It was a pleasure to watch your surgical work with the mechanics. And thank you for speaking Dutch with me to help me practice. Frits Janssen, thank you for your cheerfulness. I must admit that the technical support that we have in HFML is incredibly good.

At the beginning of my work at HFML, I learned the operation of the installation from Jonathan Buhót. He has very good teaching skills. It was funny that I wanted to see everything that can go wrong to learn how to handle it, so I was the only person at his magnet times who was happy to see an error or a magnet trip. Thank you also for repairing my bike and taking me out of some other problems. You are a very kind and generous person.

Bence Bernáth, my friend, thank you for the music you used to set while working in the lab, for our full of discussions and scientific dreams walks in Malden with baby strollers and for your support.

To the person with whom I shared a mechanical probe, Vishal Bechai, thank you for being such a responsible experimenter, keeping the toolbox in order and maintaining the documentation. You were an example to me; I always checked with you on all these things. Also, thank you and Koen van den Hoven for being such good neighbors in our optical room. Kingshuk Mikhuti spread out even to my part of that room and performed experiments all over the place. Kingshuk, you are also a perfect magnet body for me. It was really comfortable, easy, and interesting to work with you! I hope you are not going to be as hardworking as you are now, it has to slow down a bit at some point.

Another example of an incredibly energetic person is Sandra Kleuskens. I have no idea how she manages everything: working at HFML (we all know what that means), organizing all possible activities, doing sports every day, and representing all of us to the senior staff. Thank you for being attentive to me, for our walks and talks, and for creating the right atmosphere in the group.

I have to admit that we have an amazing girls team at HFML. Sanne Kristensen and Femke Bangma, it was a pleasure to have you around. Roos Leenen, we both finally completed our PhDs by the end of 2024. Thank you for your excellent interpersonal skills, support in cryogenics, our board game evenings, for occasionally looking after my son, and for the wonderful marriage feast you held for all of us.

One of sudden, Elvina Dilmieva has also become a part of HFML team.

We met in Grenoble doing an experiment at synchrotron together and became friends. In general, it is not surprising that difficulties bring people together. I'm glad you've started working with us. And special thanks for your support during my second maternity period.

Hannah Willenberg, I will not forget making ginger cookies under your supervision. You are the person in the company of whom the Dutch say "gezellig". All the best for your PhD trajectory.

My first office neighbor was Claudius Müller. Thank you for all the useful tips and your kindness. After COVID times, I moved to the office with Thom Ottenbros, Arwin Kool, and Kingshuk. I have heard so many interesting stories about the field of superconductors there! Special thanks for the constant supply of sweets. Your company made me go to work with a smile.

I would also like to acknowledge Andrea Marchese, Mariana Ballotin and Maarten van Delft, Jasper Linnartz, Maurice Bal, Davide Pizzirani, Sasha Zheliuk and Sven Badoux.

There are also external people who participated in making this thesis possible. Aleksandr Buzdakov, thank tou for the theory and the ability to consult with you for the further projects. Raj Medapalli, you are so kind to supply us with plenty of FeRh samples! Also, thank you for your revisions and assistance in submitting our paper to npj Spintronics. Shingo Yamamoto, thank you for being my first guest user. Robert and Paul, it was incredibly interesting to work with you on your portable laser system. I've got a lot of insights from both our magnet times.

I'm grateful to my previous group, Nonlinear Optics of Nanostructures and Photonic Crystals. Particularly, to the head Tatiana Murzina and my first supervisor Irina Kolmychek. I'd like to thank them not only for everything I learned from them but also for how they guided me in the right direction in my career.

Gladly, now I'm a part of an amazing group, Physics of Nanostructures at Eindhoven Technical University. Special thanks to Reinoud Lavrijsen for the great opportunity to work there and to finalize this thesis.

During my PhD path, I have met people very important to me. Those, without whose support I can't imaging this to come true. Dasha Sylgacheva, we are from the same university but met each other only during your visits to the USCM group at the beginning of my PhD. So great that you did this research and I got to know such a bright and kind person. Oliwia and Marcin Duchnowski, we were learning Dutch together but eventually became neighbors and close friends. Despite not being scientists, you taught me a good approach to life and kept supporting me during the difficult times. Liesbeth Pierson, thank you for the French and Dutch lessons and for your boundless kindness. Also, thanks for offering me alternatives to the PhD path - it made me feel safe. Bektur, thanks for your always incredible stories, I am happy to know you. Andrey and Olga,

who could guess that such bad circumstancies as getting a support from university about the war in our motherland, can help to find such good friends. Thank you for always being up for something, for the support, for understanding and sharing parenting with us.

Now about the people who constantly tolerated me: Family. Dear Sasha, without you I would 100% get a burn-out very soon. It is so important to have the support of a person who knows every detail of your work. Someone who understands you fully. Someone, ready to bring you to the lab and/or back in the middle of the night or very early morning. Someone in front of whom you can safely cry and be calmed down. Someone who has to listen to all possible presentations first. And this is just the beginning of the list. So, thanks for being the best husband I can ever dream of for already 10 years.

Thanks to my two small boys: Daniel and Mihail. You have changed my life. Twice. It can't be said deeper, I love you, boys, you are my treasure.

To my mother Emma. Thank you so much for almost every day support, for believing in me, for coming to us to help in spite of all that collapse that was happening in the world during this period. Thanks for being even ready to move to another country to stay in touch. I am very proud of you and your strength.

In general, we are very lucky to have such parents. Olga, Denis and already grown-up Angelina, thank you for taking care of us, for spending all your possible vacations with us. Thank you for your immense love. Incredible grandparents Galina and Nugzar in their 70s came to us yearly for a few months to help with kids and household. During this visits I could fully recharge and feel myself a little girl again.

Thank you, my grandmother Ludmila and uncle Alexander for bringing me up, for everything that's in it. I am who I am because of you and our beloved Nickolay. I love both of you. Also thanks to the big uncle Dima, who was ready to defend us against all possible troubles. I'd like to thank my farther Alexey too for keeping in touch.

Johan, I'm happy you've joined our family. Thank you for your kindness and cheerfulness.

Dear committee members, thank you for taking the time to read and assess this thesis.

And to you, dear reader, thank you for opening this book, whether you're here to find your name in the acknowledgments or to delve into the culmination of six years of research.

Contents

Chapter 1

Introduction

Magnetic fields produced by the Earth's outer core surround us, which enables us to navigate using a compass, and also some animals can feel it. See for example [1]. But our weak planetary field of about 50 μT can not be compared with those produced by the pulsar (10^7 to 10^9 T) or magnetar (10^{10} to 10^{11} T) [2]. Complex magnetic behaviours take place in many not fully studied processes from the formation of stars to the features of quantum materials, such as high-temperature superconductors and topological insulators. Understanding magnetism contributes to our knowledge of the universe.

A magnetic field has emerged as an invaluable experimental tool, unveiling not only the intricate mechanisms dictating physical processes in condensed matter but also pioneering new frontiers across various other domains in modern science, from material science and quantum technology to chemistry and biology. In this thesis, we will describe fundamental research, which became possible thanks to magnets producing high DC magnetic fields. Such magnets are unique and exist in just a few places in the world besides HFML-FELIX in Nijmegen (see Table 1.1): LNCMI in Grenoble, France (up to 37 T); NHFML in Tallahassee, USA (up to 45 T); CHMFL in Hefei, China (up to 45.2 T), the TML, Japan (up to 35 T); the HFLSM in Sendai, Japan (up to 30 T).

In particular, this thesis is dedicated to the topic of ultrafast spin dy-

LNCMI Grenoble, France	NHFML Tallahassee, USA	CHMFL Hefei, China	TML Tsukuba, Japan	HFLSM Sendai, Japan	HFML Nijmegen, the Netherlands
37 T	45 T	45.2 T	35 T	30 T	38 T

Table 1.1: High magnetic field facilities throughout the world, that provide DC magnetic fields.

namics in antiferromagnetic materials. Ultrafast spin dynamics, also referred to as ultrafast magnetism and femtomagnetism, is a relatively young but rapidly developing research field that aims to understand spin dynamics in magnetically ordered materials excited on a timescale much shorter than the characteristic time required for media to reach thermodynamic equilibrium (thermalisation time). In condensed matter physics, this time is typically in the range of 1-100 ps [3–5]. While state-of-the-art theories in magnetism are predominantly based on equilibrium thermodynamics and corresponding (adiabatic) approximations, such an ultrafast stimulus brings media into a strongly non-equilibrium state, where the conventional description of magnetic phenomena in terms of non-equilibrium thermodynamics is no longer valid. During almost 3 decades of fundamental studies of ultrafast magnetism, magnetic materials with a mutually antiparallel coupling of spins (ferri- and antiferromagnets) have proven to be among the most appealing in the research field, as they show counter-intuitive phenomena, such as laser-induced helicity-dependent switching (HD-AOS) [6], toggle switching by optical pulses [7] or ultrashort electrical current pulses [8].

It has been recently realized that the rich magnetic field (H) - temperature (T) phase diagram of ferri- and antiferromagnets hosts several magnetic phases [9–12] and thus offers a plethora of opportunities for fundamental studies of ultrafast magnetism in these materials.

The goal of this thesis is to benefit from the high magnetic fields available at HFML-FELIX at Radboud University to explore ultrafast spin dynamics in a large area of the H-T phase diagram of materials with antiferromagnetically coupled spins.

1.1 Magnetism

A magnetic field is one of the main experimental tools in contemporary material science. Practically all materials respond to external magnetic fields. The ability to respond to a magnetic field is described by the magnetic susceptibility, χ, which is a material-specific property. Merely a century ago, materials were categorizable into three primary classes based on their magnetic susceptibility: ferromagnets (with $\chi > 1$), paramagnets (with $|\chi| << 1$ and $\chi > 0$) and diamagnets (with $|\chi| << 1$ and $\chi < 0$). The susceptibility relates the external magnetic field $\vec{H}$ to the magnetization $\vec{M}$, which the field induces in the medium $\vec{M} = \chi\vec{H}$. In the case when the susceptibility is low, the magnetic response of the material is small as well. However, even materials traditionally considered as 'non-magnetic' display a minimal but measurable response when exposed to magnetic fields, reflecting the fundamental principle that electromagnetic interactions affect all matter to some extent [13]. The magnetic susceptibility depends not only on temperature and pressure but also on the external magnetic field

itself. For instance, a material in its superconducting phase exhibits ideal diamagnetic behaviour ($\chi = -1$). However, the application of a magnetic field can disrupt this state, leading the material into a regime where $\chi << 1$, thereby extinguishing superconductivity.

1.1.1 Magnetic interactions

The magnetic susceptibility is a macroscopic property and not necessarily tells much about the origin of the magnetic response of a material. To this end, to understand the microscopic origin of (ferro)magnetism, we need to address the internal fields in the material. In general, condensed matter systems are very complex and their behaviour is defined by mutual interactions of continuously moving constituting atoms, but the application of a mean-field approximation allows us to significantly simplify the physical description giving it a simple and intuitive form. Such a mean-field theory relies on averaging all magnetic interactions, resulting in a thermodynamically defined effective field. The magnetic moment of an individual atom originates from both unoccupied orbital states as well as uncompensated spins. More particularly, the magnetic moment of an atom is defined through both the spin and orbital moments of electrons. It can be defined as:

$$\vec{m} = -\frac{\mu_{\mathrm{B}}}{\hbar}(2 < \vec{S} > + < \vec{L} >), \tag{1.1}$$

where $< \vec{S} >$ and $< \vec{L} >$ are the expectation values of the spin and orbital angular momenta for all considered electron states in the atom, μ_{B} is the Bohr magneton and $\hbar$ the Planck's constant. The spin magnetic moment gives a contribution to the total moment, which is two times that of the orbital magnetic moment. In general, the magnetism of atoms is mainly given by the spin of electrons, with only a small contribution from orbital momentum. In the first approximation, the orbital contribution can even be neglected and appears only in the corresponding Hamiltonian as a result of spin-orbit interaction. This is because of a phenomenon called "quenching of orbital momentum" in condensed matter systems [14]. The electrostatic field, created by the surrounding ions lifts the degeneracy of orbital states leading to full ($\vec{L}$=0) or partial quenching of the orbital momentum, making the electron's spin the dominant contribution of the magnetic moment in Eq. 1.1.

Also, spin-orbit coupling can play a role in the total magnetic moment. It typically involves an interaction between the electron's spin and its orbital angular momentum in the presence of the electrostatic field of the nucleus, leading to an extra term in the Hamiltonian:

$$\mathcal{H}_{\mathrm{so}} = \zeta_{nl}(r)\vec{S} \cdot \vec{L} \tag{1.2}$$

The spin-orbit coupling constant $\zeta_{nl}(r)$ depends on the radial positions and spins of the electrons. This interaction provides the coupling of the spin

system to the lattice. Typically, in condensed matter, the energy associated with the spin-orbit coupling is of the order of 10-100 meV [15].

There is a much stronger interaction experienced by spins in condensed matter systems, which can be as strong as 1 eV. It is called exchange interaction. The corresponding term in the Hamiltonian can be effectively described by the following Heisenberg Hamiltonian:

$$\mathcal{H}_{\text{exch}} = -\sum_{i \neq j}^{N} J_{ij} S_i S_j \tag{1.3}$$

The sum is weighted with the exchange integral J_{ij}. S_i and S_j are the spins of two electrons. It reflects the energy associated with a change in quantum states between the two electrons. It arises from the fact that when wavefunctions of two indistinguishable particles (fermions or bosons) overlap, the expectation value of the distance between the particles will depend on the nature of the particles and their quantum numbers. In particular, for two electrons (i.e. fermions) having identical sets of quantum numbers the expectation value is larger than for two electrons whose spins are opposite. For bosons the situation is opposite, and the distance is smaller. The distance between two quantum particles with overlapping wavefunctions must thus depend on the mutual orientation of their spins. Together with the Coloumb interaction, the spin-dependent distance results in a spin-dependent contribution to the interaction between the particles. Spin-dependent energy means that the thermodynamic equilibrium favours such alignment of spins of the particles with overlapping wavefunctions for which the exchange energy is minimized. This interaction is responsible for the alignment of spins and spin order in condensed matter systems [16].

Spins interact with external magnetic fields via the Zeeman interaction. Assuming the magnetic field $\vec{H}$ applied along the z direction, the Zeeman term in the Hamiltonian can be written as:

$$\mathcal{H}_{\text{zee}} = -\mu_0 \vec{m} \cdot \vec{H} = -\frac{\mu_0 \mu_{\text{B}}}{\hbar}(2 < S_{\text{z}} > + < L_{\text{z}} >) H_{\text{z}} \tag{1.4}$$

Here $< S_{\text{z}} >$, $< L_{\text{z}} >$, and H_{z} are projections of the spin, orbital momentum and external magnetic field on the z axis. In this situation, the magnetic moment tends to align along the field direction. Thus, due to the Zeeman interaction, initially, randomly oriented internal moments of paramagnets align along the external magnetic field.

1.1.2 Correlation between magnetism and crystal structure

The interactions described above act between electrons, so their mutual distance and the density of states can directly influence the interaction

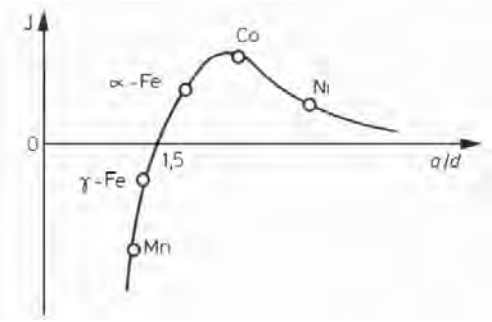

Figure 1.1: The exchange integral J versus the interatomic distance a over the size d of a 3d orbital (the so-called Bethe-Slater diagram.) [17].

strength. Thus, the band structure directly correlates with magnetic properties. Narrow electronic bands imply electron localization. The wavefunction overlap integrals decrease with the number of electrons, so magnetism emerges in the second part of the transition metal series. The best-known ferromagnets are transition metals such as Fe, Co and Ni, which have a more than half-filled 3d-orbital. The Stoner criterion states that both a strong electron-electron interaction (high exchange constant J) and a high density of states at the Fermi level $N(E_\mathrm{F})$ lead to ferromagnetism when $JN(E_\mathrm{F}) > 1$ per atom. This condition indicates that the electron-electron interaction energy associated with the exchange interaction is greater than the system's thermal energy or other competing energies to promote parallel spin alignment. The Stoner criterion exceeds one only for Fe, Co and Ni. There is a correlation between the nearest-neighbour distance and magnetic order in the 3d transition metals, which is demonstrated in the Bethe-Slater diagram (Fig. 1.1). However, electron localization should not be extremely high to still provide an overlap between the wavefunctions of the electrons from neighbouring atoms; otherwise, thermal fluctuations overwhelm the exchange interaction, magnetic order melts and the system becomes paramagnetic.

It is interesting that although the exchange interaction for Mn is not null, the exchange integral is negative (see Fig. 1.1) and thus it does not favour mutually parallel i.e. ferromagnetic alignment of spins. Instead, neighbouring spins align mutually antiparallel such that the net magnetic moment is zero. This is a relatively new class of magnetic materials, called antiferromagnetic (AFM), which was discovered only in the 20th century by Louis Néel, who was awarded the Nobel Prize for this discovery.

Interestingly, Mn-containing compounds can have different magnetic order, depending on the interatomic distances [18, 19]. Accordingly, the materials can show a phase transition between ferro- and antiferromagnetic phases under applied pressure and changing the lattice parameter.

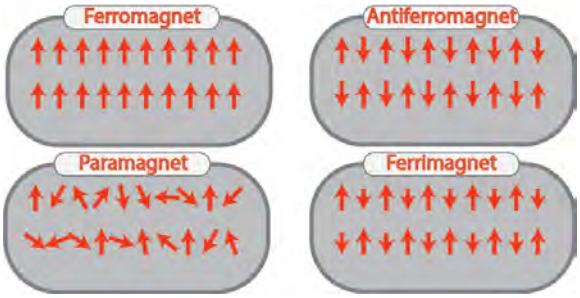

Figure 1.2: Schematic representation of the different magnetic phases described in the text.

Combining all the components mentioned above, to describe the magnetic behaviour of a material we can write the following Hamiltonian:

$$\mathcal{H} = \mathcal{H}_{\text{so}} + \mathcal{H}_{\text{exch}} + \mathcal{H}_{\text{zee}} \tag{1.5}$$

Thus, the whole crystal structure plays a role in the magnetic order, and not only the interatomic distance. The arrangement of ions in the crystal creates preferred directions for spins due to the spin-orbit interaction, resulting in magnetic anisotropy. The energy needed to rotate the magnetization from an "easy" to a "hard" axis is defined as the magnetic anisotropy energy (MAE). Due to the relative weakness of the spin-orbit interaction, the MAE is usually small (of the order of 10^{-2} to 1 meV/atom) [15].

Of course, the inclusion of particular terms in the Hamiltonian and the level of their complexity would strongly depend not only on the studied system but also on the external parameters. What would change in the magnetic material upon varying the external magnetic field and temperature?

1.2 Thermodynamical approach

1.2.1 Critical behavior of ferromagnets

When we talk about magnetic materials the first type of materials that come to mind are ferromagnets (Fig. 1.2). Indeed, ferromagnetic (FM) materials are characterized by a large magnetic moment, and a spontaneous magnetization due to the internal exchange interaction. A positive sign of the exchange integral in Eq. 1.3 corresponds to the parallel alignment of spins.

Already the application of a low external magnetic field is sufficient to realign the spins along the field direction. Saturation of the total magnetization is easily reached, and removal of the external field will not lead to the relaxation of the spins back to isotropic alignment. The system

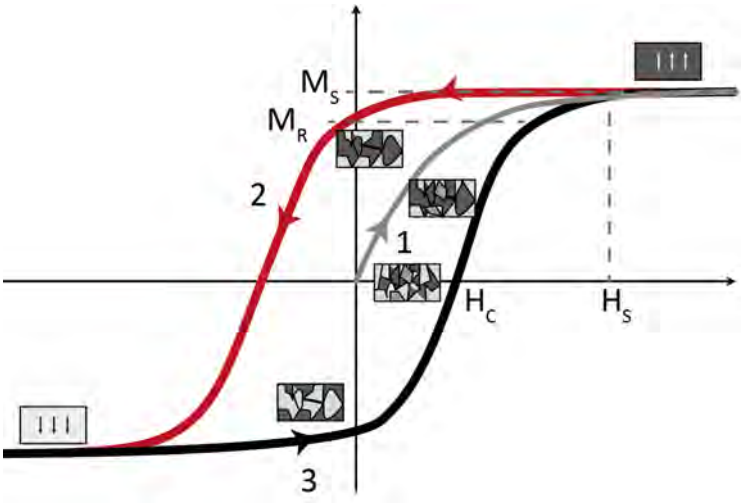

Figure 1.3: The qualitative $\vec{M}(\vec{H})$ behaviour in ferromagnetic material. Insets demonstrate relative domain growth in an external magnetic field.

shows a remanent magnetization at $\vec{H} = 0$ and in order to reverse it, an opposite magnetic field has to be applied. The field needed to reduce the magnetization to zero is called the coercive field. This phenomenon causes a hysteresis loop in the $\vec{M}(\vec{H})$ dependence (Fig. 1.3). Thus, the system has a memory of the direction of the applied field.

The shape of the magnetization curve and the possibility of accessing the internal area with variation of the field amplitude suggest the existence of different pathways of the realignment process. This is indeed the case, as there are multiple areas of homogeneously aligned magnetization in a ferromagnetic sample, the so-called domains. The domain structure appears to minimize the energy needed for the stray magnetic field that goes outside the material. Thus, the application of a magnetic field favours the alignment of the domains with the same magnetization direction supporting their growth.

It is known, that a temperature increase destroys magnetic order and thus destroys spontaneous magnetization.

This behaviour can be explained in an elegant way using the principles of thermodynamics.

A magnetic phase is usually stable in a certain range of the thermodynamic variables, such as the temperature, the magnetization, the external magnetic field and the entropy S. The stability of the phase is then reached at the minimum of the free energy potential:

$$F = U - TS, \tag{1.6}$$

where U is the internal energy, which includes contributions from the ex-

change interaction, anisotropy and the Zeeman effect. So the internal energy of a magnetic medium, with constant volume and a number of particles, depends on $\vec{M}$, $\vec{H}$, S and T.

Fig. 1.4 shows a typical example of several representative free energy potentials as a function of magnetization, a common order parameter in magnetism, for three different temperatures. At temperature T_1, minima of F occur at finite magnetization, one of which is indicated by a grey circle. Upon changing temperature (T_2) the local minimum in the free energy potential begins to flatten, indicating a destabilization of the existing state. Upon reaching the critical temperature (T_3), the potential minimum occurs at zero magnetization (red circle), depicting the transition of the system transition to a new phase. In this scenario, the material acquires easy plane anisotropy, with the M_z component remaining stable at zero, illustrating a significant alteration in its magnetic behaviour.

Varying the external parameters leads to competition between different states in order to minimize the free energy. Increasing the temperature adds thermal fluctuations and applying an external magnetic field causes alignment of the spins. The ranges of the parameters within which the phase is stable can be plotted as a phase diagram that visualizes the conditions for the different phases and the critical points where transitions take place.

Phases can co-exist if their thermodynamic parameters from Eq. 1.6 are equal. There are two types of phase transitions - first and second order. At a first-order phase transition the parameters, that are a first derivative of the free energy in Eq. 1.6, (i.e. S, V, $\vec{M}$), change abruptly. For instance, a jump in $\vec{M}$ leads to hysteresis, which is a signature of a first-order phase transition. In some cases, the first derivatives of the free energy are equal for competing phases, and only the second derivatives change abruptly. Then the transition is smooth as a function of the first derivative variables, and no hysteresis occurs. Such transitions are of second order.

Phase transitions can be understood by observing a change in an order parameter, a concept introduced by Landau in his theory of phase transitions [20]. The transition point is defined as the moment when this parameter, which reflects an asymmetry of the system, turns to zero due to variations in external parameters. In this formalism, the thermodynamic potential is represented as a polynomial with even-order terms of the order parameter, and the coefficients determine the phase transition order. In magnetism, the order parameter is usually either the normalized magnetization vector or the antiferromagnetic vector, defined below.

Let us consider the free energy in the presence of the external magnetic field $\vec{H}$.

$$F(M;H) = F(M;0) - \frac{\mu_0}{2}(\vec{H} + \vec{M})^2 \tag{1.7}$$

$F(M;0)$ contains all internal energy of the system without an applied magnetic field.

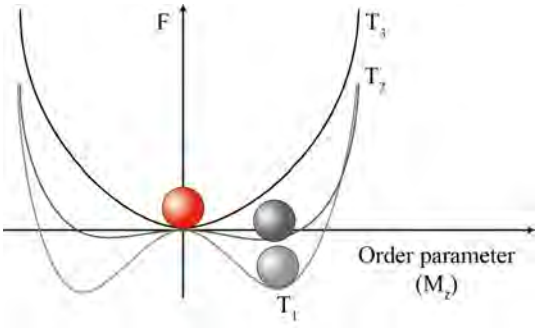

Figure 1.4: Schematic dependence of a typical evolution of the free energy potential on an order parameter, describing a phase transition as a function of temperature.

Increasing the temperature to a value where thermal fluctuations overcome the spin alignment, a ferromagnetic to paramagnetic phase transition occurs, which was first described by Pierre Curie. Therefore, the transition temperature is called the Curie temperature T_{C}.

Landau showed that in the vicinity of the Curie temperature, where the magnetization $\frac{|\vec{M}(T)|}{M(0)} << 1$ it is possible [21] to expand the expression in the powers of $\vec{M}$ with coefficients A and B, which can vary only with temperature or pressure. A is assumed to be positive above T_{C} and crossed zero at $T = T_{\mathrm{C}}$. When $\vec{M}||\vec{H}$ and having in mind that the potential has to be invariant under a gauge transformation, the expansion of the free energy will contain only even powers of the magnetization amplitude M, magnetic field H or combinations thereof:

$$F = F_0 + AM^2 + BM^4 - \frac{\mu_0 H^2}{2} - \mu_0 MH - \frac{\mu_0 M^2}{2} \tag{1.8}$$

Above the Curie temperature the coefficient $A = a(T - T_{\mathrm{C}})$, where a is a temperature-independent positive constant. Then after differentiation of F with constant H, $2AM + 4BM^3 = H$. Thus, close to the Curie temperature in the absence of the field $M(T)$ can be found as

$$M(T) = \sqrt{a(T_{\mathrm{C}} - T)/2B}, \tag{1.9}$$

where the coefficient B is nonzero and positive.

This expression holds only in the vicinity of the Curie temperature. To describe the dependence far away from that region we would have to employ a more complex one from Weiss's molecular-field theory:

$$\frac{M}{M(0)} = \mathcal{B}_J\left(\frac{\mu_0(H + \beta M(T))}{kT}\right) \tag{1.10}$$

This is a transcendental equation with the Brillioun function $\mathcal{B}_J(x)$, where β is the molecular field constant, which acts as a coefficient relating the molecular field to the magnetization, expressed as $H_{\mathrm{W}} = \beta M$ [15].

Variation of the applied magnetic field can also lead to critical behaviour due to the presence of anisotropy. Generally, the latter is:

$$U_{\mathrm{an}} = \sum_{i \neq k}^{N} K_{ik} m_i m_k \tag{1.11}$$

Where K is the anisotropy constant and m_{ik} are unit vectors defining the direction of $\vec{M}$. For an uniaxial crystal, the sign of K will define the direction of easy magnetization as U_{an} reaches its minimum for different values of the angle θ between the magnetization and the z-axis, which is aligned with the symmetry axis:

$$U_{\mathrm{an}} = K \sin^2\theta \tag{1.12}$$

Let us consider the case of an easy-axis ferromagnet with $K = \frac{1}{2}\beta M^2$. When the external field has projections on both the x- and z- axes (assuming symmetry in the xy-plane) the thermodynamic potential will be modified into:

$$\begin{aligned} F = F_0(M) + \frac{1}{2}\beta M^2 \sin^2\theta - \\ -\mu_0 M(H_{\mathrm{x}}\sin\theta + H_{\mathrm{z}}\cos\theta) - \frac{\mu_0 H^2}{2} \end{aligned} \tag{1.13}$$

The condition $\partial F/\partial\theta = 0$ gives the parameters of the equilibrium:

$$\beta M \sin\theta\cos\theta = H_{\mathrm{x}}\cos\theta - H_{\mathrm{z}}\sin\theta \tag{1.14}$$

This equation can be solved for $\sin\theta$ but has either two or four real solutions, which means one or two possible directions of $\vec{M}$ depending on the value of H_{x} and H_z. When both $\partial F/\partial\theta = 0$ and $\partial^2 F/\partial\theta^2 = 0$ both cases occur. To find the critical H_{x} and H_{z} we can apply the second condition ($\partial^2 F/\partial\theta^2 = 0$) and solve the result for H:

$$H_{\mathrm{x}}^{2/3} + H_{\mathrm{z}}^{2/3} = (\beta M)^2/3 \tag{1.15}$$

The equation represents the astroid curve that limits the region where metastable states can exist. It means that the magnetic body can be separated in areas with $\vec{M}$ having one of its two possible directions. Such a unified area is a domain as shown in Fig. 1.3.

1.2.2 $H - T$ phase diagram of antiferromagnets

The exchange constant in the exchange interaction Hamiltonian can be negative. Then the antiparallel alignment of spins is preferable. In this

case, the antiferromagnetic lattice can be divided into sublattices with ions, whose spins are parallel to each other. Then for each sublattice, we can define a macroscopic magnetization, however, the total magnetization of the whole material (net magnetization) will be cancelled out.

In an antiferromagnet, the magnetization is defined through the antiferromagnetic vector $\vec{L} = \frac{\vec{M}_1 - \vec{M}_2}{2}$. Here $\vec{M}_1$ and $\vec{M}_2$ are the magnetizations of the two sublattices. The net magnetization $\vec{M} = \frac{\vec{M}_1 + \vec{M}_2}{2}$ is zero in the absence of an external magnetic field.

Analogous to ferromagnets, antiferromagnets have a critical temperature where the antiferromagnetic vector turns to zero. This temperature is named after Louis Néel, who has for the first time discussed antiferromagnetism as a class of magnetic materials.

The behaviour of antiferromagnets with a Néel temperature T_N can be qualitatively understood by considering the free energy potential in the vicinity of T_N as an expansion in amplitudes L and H with coefficients A, B, D, D':

$$\begin{aligned} F = F_0 + AL^2 + BL^4 + D(\vec{H}\cdot\vec{L})^2 + D'H^2L^2 - \\ -\frac{1}{2}\chi_\mathrm{p}H^2 + \frac{1}{2}\beta(L_x^2 + L_y^2) - \frac{1}{2}\gamma(H_\mathrm{x}^2 + H_\mathrm{y}^2) - \frac{\mu_0 H^2}{2} \end{aligned} \tag{1.16}$$

Here we use the expression for an uniaxial crystal. The susceptibility in the paramagnetic phase is denoted by χ_p. The constants β and γ account for the corrections due to relativistic interactions, which influence the crystallographic orientations of the vectors $\vec{L}$ and $\vec{H}$. The sign of the coefficient β defines the type of anisotropy. An easy axis type of behaviour requires A to cross zero at the Néel temperature, leading to a similar expression as for a ferromagnetic (newly defined equation 1.9 above) but now for L:

$$L = \sqrt{a(T_\mathrm{N} - T)/2B} \tag{1.17}$$

An easy-plane type of antiferromagnet requires a coefficient $A + \frac{1}{2}\beta$ in front of $(L_x^2 + L_y^2)$, where β is negative, to cross zero. This leads to a magnetic susceptibility in the antiferromagnetic phase that depends on the direction of the external magnetic field.

To describe this situation, we take $\vec{H}$ small, yet nonzero, so that the magnetization direction is defined, but not canted by the external magnetic field. If we take $\gamma = 0$, the susceptibility in paramagnetic phase χ_p is isotropic, leading to:

$$\vec{M} = \chi_\mathrm{p}\vec{H} - 2D\vec{L}(\vec{L}\cdot\vec{H}) - 2D'L^2\vec{H} \tag{1.18}$$

Then if $\vec{H} \perp \vec{L}$:

$$\begin{aligned} \vec{M} = \chi_\perp\vec{H},\ \chi_\perp &= \chi_\mathrm{p} - 2D'L^2 = \\ &= \chi_\mathrm{p} - (D'a/B)(T_\mathrm{N} - T) \end{aligned} \tag{1.19}$$

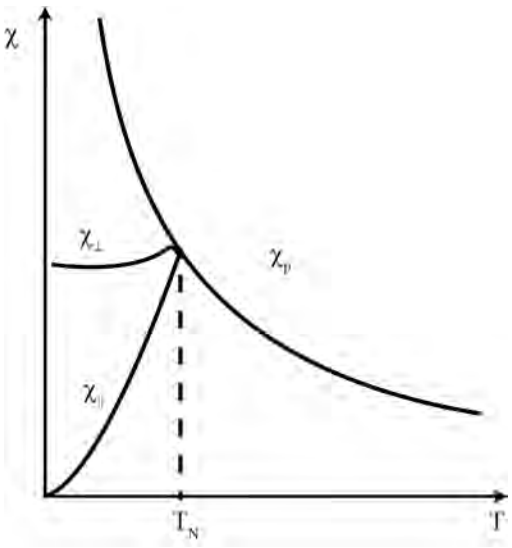

Figure 1.5: Susceptibility of an antiferromagnet for different orientations of the external magnetic field.

And for $\vec{H} \parallel \vec{L}$

$$\begin{aligned} \vec{M} = \chi_{\parallel}\vec{H},\ \chi_{\parallel} =& \chi_{\perp} - 2DL^2 = \\ =& \chi_{\mathrm{p}} - (D + D')a(T_{\mathrm{N}} - T)/B \end{aligned} \tag{1.20}$$

From these expressions, it follows that in antiferromagnets the susceptibility is finite at the Néel temperature, whereas in ferromagnets χ diverges at the Curie temperature $\chi \sim \frac{1}{T-T_{\mathrm{C}}}$ [20]. Figure 1.5 shows a typical example of the behaviour of the magnetic susceptibility of an antiferromagnet as a function of temperature, for two directions of the applied magnetic field.

Spin-flop

Eq. 1.16 shows that for antiferromagnetic and ferrimagnetic materials, orthogonal directions of the external field lead to different minima of F. When the magnetic field is applied along the antiferromagnetic vector, the material is insusceptible to the magnetic fields below some limit H_{SF}, the value of which is defined by the magnetic anisotropy and the exchange terms in the Hamiltonian. At H_{SF} the symmetry breaks and the antiferromagnetic vector changes its direction, such that it cants to an almost in-plane direction. This phenomenon is called spin-flop and it is the transition of the first order in antiferromagnetic, but can be of the second order in ferrimagnets. In this phase, the material is minimizing the Zeeman energy while still maintaining antiferromagnetic order.

To describe this effect we first consider $H < H_{\mathrm{SF}}$, such that the minimum of F in Eq.1.16 for the corresponding terms:

$$H_{\mathrm{z}}^2 DL^2 + L^2(-DH_{\mathrm{z}}^2 + 1/2\beta)\sin^2(\theta) \tag{1.21}$$

is reached for $\theta = 0$. Otherwise, it is $\theta \sim \frac{\pi}{2}$. From the potential the field is given by:

$$H_{\mathrm{SF}}^2 = \beta L^2/(\chi_\perp - \chi_\parallel) \tag{1.22}$$

To derive the exact value of the spin flop field, we need to consider the total energy of the system, the particular anisotropy energy and possibly higher-order terms in the expansion of the potential with respect to the magnetization. Minimization of the potential for the exact magnetic system with respect to θ can provide the functions $H_{\mathrm{SF}}(T)$ and $\theta(H;T)$. Applying a higher magnetic field leads to a further canting of the sublattices, i.e. the decrease of θ.

The classical example of a spin flop transition can be found in MnF_2 at ≈ 9 T [22], which is antiferromagnetic below the Néel temperature $T_{\mathrm{N}} = 67$ K. There is a correlation between the Néel temperature and the critical field for the spin flop. Indeed, both transitions occur when there is some competition with the exchange interaction. Either the Zeeman energy starts to rise in the applied field or the thermal fluctuations are high enough to ruin the antiferromagnetic order. For the same reason, the antiferromagnetic resonance can give an estimation of the spin flop field, where the lower mode disappears and the collinear phase loses stability. The spin-flop transition can be found also in ferrimagnetic materials, in which uncompensated sublattices can come from the same ions like Fe^{3+} in YIG [23], or even by different layers like in the case of Co-Gd (transition metal- rare earth material) [24]. In this case, the spin flop field is a function of temperature and reaches its minimum at the compensation temperature if it is present in the material.

Further increase of the external field aligns the sublattices. It occurs slowly and the field when such alignment is possible should be of the order of the exchange field. For example, in the case of YIG, it has appeared to be over 275 T [25, 26].

At the critical external field, the antiferromagnetic order disappears as a second-order phase transition. The value of this field is a function of temperature $H_{\mathrm{c}}(T)$, which should reach zero at T_{N}. When at low temperatures it is compared with the exchange field, close to T_{N} it can also be found from the potential Eq.1.16. Again, we have to consider two orientations of this field. In the case of $\vec{H} \perp \vec{L}$, the transition takes place when $A + D'H^2 = 0$:

$$H_{\mathrm{c}}^2 = a(T_{\mathrm{N}} - T)/D' \tag{1.23}$$

When the field is parallel to the z-axis, we have to consider the cases below the spin-flop field, where $\vec{L}$ is directed along z:

$$H_{\mathrm{c}}^2 = \frac{a}{D + D'}(T_{\mathrm{N}} - T) \tag{1.24}$$

In the high-field approximation, where the $\vec{L}$ components are already in plane:

$$H_c^2 = a/D'(T_N - T - \beta/2a) \tag{1.25}$$

For an easy-axis antiferromagnet, with $\beta > 0$, the field applied along the z-direction earlier destroys the antiferromagnetism.

Antiferromagnets can also exhibit significant magnetic moments per ion, like hematite, NiO or MnO. They can be not only metallic but also semiconducting, semimetalic and insulating, which is beneficial for the propagation of spin waves and, in some cases, these materials exhibit multiferroicity [27].

The absence of a net magnetization leads to a distinct behaviour in antiferromagnets compared to ferromagnets [28–30]. There are no stray fields, and the domain formation in antiferromagnets has other origins. There are certain difficulties in detecting the magnetic behaviour because common measurement techniques can only detect a macroscopic magnetization. Also, antiferromagnets are much less susceptible to the external field than ferromagnets. Together with inter-sublattice antiferromagnetic exchange interaction, it leads to faster magnetization dynamics (THz range), much larger internal exchange torques and magnon velocities [29]. Those effects can be reached as well in synthetic antiferromagnets consisting of antiferromagnetically coupled ferromagnetic layers [31].

Thus, antiferromagnets appeared to be promising for energy-efficient spin manipulation [32]. While developing tools for ultrafast magnetic recording, it was realised that the limit of the speed of angular momentum transfer restricts the possibilities to operate ferromagnets. On the other side, in antiferromagnetic materials, there is no need to wait until angular momentum goes from the spin system to the lattice, as it can directly redistribute within the compensated spin system of an antiferromagnet. Together with the absence of stray fields, it can result in the desired long propagation distance of magnons, which is important for applications in spintronics [33].

Ferrimagnets

The sublattices do not always need to have an equal magnetization. Materials with an antiferromagnetic exchange constant but different magnetic moments per sublattice are known as ferrimagnets (see Figure 1.2). The net magnetization is non-zero and the behaviour of such materials is easier to detect.

Different temperature dependencies of the magnetizations of the two sublattices lead to the appearance of the compensation temperature. At this particular temperature, the magnetizations of the sublattices are equal and the behaviour of the system becomes similar to that of an antiferromagnet. The compensation of the magnetisation and the angular momentum can occur at slightly different temperatures. Then, for example, the fast domain wall motion like in antiferromagnet occurs while the net moment

is still non-zero [34]. Also, the laser-induced magnetization switching was shown for a ferrimagnetic material as a result of ultrafast heating of the system above the compensation temperature [7, 35].

1.3 Spin dynamics

Spin dynamics in FM and AFM materials is totally different as a consequence of the peculiarities of their behaviour considered in the section above. The intrinsic dynamics in AFM materials can be significantly faster than in FM materials due to the stronger antiferromagnetic exchange interaction and higher frequency spin waves [32]. The antiparallel alignment of spins leads to more complex precession than in ferromagnets and can support several spin wave modes. These modes reflect in-phase and out-of-phase precessions of the sublattice magnetizations [36, 37].

Heating provided by an ultrafast laser pulse modifies the effective magnetic field $\vec{H}_{\text{eff}}$, in which the spin is situated. The time-dependent term in the effective external field $\vec{h}(t)$ leads to the dynamics of the magnetization $\vec{M}$.

1.3.1 Modelling spin dynamics in ferromagnets in terms of a single macrospin

Using mean-field theory and the macrospin approximation, we neglect individual spins in magnets and describe them in terms of a net magnetization - macrospin. In such a way the uniform regions of coherently moving spins can be considered as a whole, but the approximation leaves out the local interaction between spins and all sorts of inhomogeneities.

Magnetization dynamics can be triggered by a torque $-\gamma\vec{M} \times \vec{h}(t)$, where γ is the gyromagnetic ratio of the system, which launches a precessional motion according to the Landau-Lifschitz equation:

$$\dot{\vec{M}} = -\gamma\vec{M} \times \vec{H}_{\text{eff}} \tag{1.26}$$

where $\vec{H}_{\text{eff}}$ is the effective magnetic field defined via the derivative of the thermodynamic potential F:

$$\vec{H}_{\text{eff}} = -\frac{1}{\mu_0}\frac{\delta F}{\delta \vec{M}} \tag{1.27}$$

The total free energy includes the magnetic anisotropy energy, which in the expression for the effective field transforms into the anisotropy field H_{an}. It describes the field required to reorient the magnetization of a magnetic material from an easy to a hard axis. In ferromagnets, it can reach significant values of several Teslas, such as 8 T for NdFeB magnets [38].

1.3.2 Modelling spin dynamics in antiferromagnets in terms of two macrospins

The existence of more than one spin in antiferromagnets requires an extension of the eq. 1.26 [36, 39]. For an antiferromagnet with equal magnetizations of the sublattices $\vec{M}_1$ and $\vec{M}_2$, the dynamics is represented through the change of the antiferromagnetic vector $\vec{L}$. These equations usually consider normalized vectors such as $\vec{m}_i = \frac{\vec{M}_i}{M_0}$ with $i = 1, 2$. Then the effective field for a particular sublattice in the simple case of collinearity is given by:

$$\vec{H}_{\text{eff}_i} = \vec{H} - H_{\text{ex}}\vec{m}_j + \vec{H}_{\text{an}} \tag{1.28}$$

Thus, in contrast to ferromagnets, in antiferromagnets, H_{ex} enters the equation of motion. Since $H_{\text{ex}} >> H_{\text{an}}$, spin dynamics in antiferromagnets is much faster than in ferromagnets.

For a compensated antiferromagnet with damping α and with parallel spin alignment eq. 1.26 takes the form:

$$\dot{\vec{m}}_1 = -\gamma\vec{m}_1 \times \vec{H}_{\text{eff}_1} + \alpha\,\vec{m}_1 \times \dot{\vec{m}}_1 \tag{1.29}$$

$$\dot{\vec{m}}_2 = -\gamma\vec{m}_2 \times \vec{H}_{\text{eff}_2} + \alpha\,\vec{m}_2 \times \dot{\vec{m}}_2 \tag{1.30}$$

This system of equations can be rewritten in terms of the normalized antiferromagnetic vector $l = \frac{\vec{m}_1 - \vec{m}_2}{2}$ and the normalized net magnetization vector $\vec{m} = \frac{\vec{m}_1 + \vec{m}_2}{2}$, which fulfil the following relations:

$$\vec{m}^2 + \vec{l}^2 = 1; \quad \vec{m} \cdot \vec{l} = 0; \tag{1.31}$$

The dynamics of those vectors is then described by:

$$\dot{\vec{l}} = \gamma(H_{\text{ex}}\vec{m} \times \vec{l} - \vec{l} \times (\vec{h}(t) + \vec{H}_{\text{an}}) + \alpha(\vec{m} \times \dot{\vec{l}} + \vec{l} \times \dot{\vec{m}}) \tag{1.32}$$

$$\dot{\vec{m}} = -\gamma\,\vec{m} \times (\vec{h}(t) + \vec{H}_{\text{an}}) + \alpha\,\vec{l} \times \dot{\vec{l}} \tag{1.33}$$

We can redefine $\vec{h}(t) + \vec{H}_{\text{an}} = \vec{H}_t$. In principle, this system can be represented only through $\vec{l}$ and $\dot{\vec{l}}$:

$$\vec{m} = \frac{1}{H_{\text{ex}}}(\vec{H}_{\text{t}} - \vec{l}(\vec{H}_t\vec{l}) - \frac{1}{\gamma}\vec{l} \times \dot{\vec{l}} \tag{1.34}$$

$$\frac{d}{dt}[\vec{l} \times \dot{\vec{l}}] = \gamma\dot{h}(t) + \gamma^2 H_{\text{ex}}\vec{m} \times \vec{H}_{\text{t}} - \alpha\gamma H_{\text{ex}}\vec{l} \times \dot{\vec{l}} - \frac{d}{dt}(\vec{l}(\vec{H}_{\text{t}}\vec{l})) \tag{1.35}$$

Thus, $\vec{l} \times \dot{\vec{l}}$ leads to a change in the net magnetization and is essential for the description of the AFM dynamics. From the equations, we see that the AFM dynamics can be triggered by the changing external field $\dot{\vec{h}}(t) \neq 0$, which creates a torque.

Having in mind the ambition to manipulate magnetization with a laser pulse, it is also essential to understand how heat provided by the laser pulse can influence the magnetic order and how fast it happens.

1.3.3 Ultrafast demagnetization of ferromagnets - the birth of ultrafast magnetism

The pioneering work of ultrafast demagnetization in magnetic materials was done by Beaurepaire *et al.* on Ni [40]. They observed an ultrafast (subpicosecond) demagnetization of the film after excitation with the laser pulse. The fast magnetization quenching due to the laser excitation raised questions like how to accommodate the angular momentum conservation as it has to transfer somewhere from the aligned spins. All following experimental studies confirmed this timescale, however, the theoretical explanation of the process is still under debate.

The action of the laser pulse on the medium is typically considered in the framework of the 3-temperature (3T) model, unless non-thermal distributions, coherent dynamics, and strong coupling effects play a crucial role. On short timescales of picoseconds or subpicoseconds, the reaction of the different subsystems such as the electrons, phonons and spins can not be considered immediate and simultaneous. To be able to describe it, those buffers are assumed to gain energy separately before reaching the equilibrium, allowing us to consider the temperature of the subsystems as electronic temperature T_e, phononic or lattice temperature T_p and spin temperature T_s. The model describes the heat exchange between these subsystems over time, providing insights into the mechanisms of ultrafast demagnetization and the pathways through which light energy is redistributed in the material.

So, when an intense laser pulse arrives at the ordered magnetic phase it creates a strong excitation. Light waves interact with electron charges [3]. This interaction results in the generation of "hot electrons". Due to electron-electron scattering mechanisms, these electrons quickly thermalize, acquiring a new Fermi-Dirac distribution characterized by a higher effective temperature. Within this temporal regime, the electronic temperature experiences a substantial elevation, reaching values on the order of 10^3 K [41].

Subsequently, the "hot electrons" exchange the heat with spins and phonons until the corresponding temperatures of all these heat reservoirs are equilibrated. Demagnetization is thus a result of an increase of the spin temperature [42].

1.3.4 Laser-induced phase transitions

The energy of the laser pulse locally heats the material. It can be used to trigger the phase transitions across the critical temperature considered in the previous section. A laser pulse can serve as an ultrafast heater capable of triggering ultrafast dynamics also in the cases of heating ferrimagnet in the magnetic field across the compensation temperature or heating a magnetic material in the magnetic field applied antiparallel to the magne-

tization, as in the case of Heat Assisted Magnetic Recording, where the applied magnetic field is below the coercive field and thus is insufficient to reverse magnetization on its own. Moreover, there are many other complex effects able to switch the magnetization state of a medium.

The action of the laser pulse is aimed at particular terms in the free energy potential of Eqs. 1.8 and 1.16. It can disturb the exchange interaction term leading to the temporal reduction of the overall magnetization $\vec{M}$ or the antiferromagnetic vector $\vec{L}$. The specific mechanism of such perturbation can be different and requires studies on ultrafast magnetization dynamics.

Heating of the material through the Curie temperature is manifested in the ultrafast demagnetization. Typically, the dynamics in the vicinity of the Curie temperature in various compounds is slowed down, proceeding in two steps, which can take tens of picoseconds in total [43]. The transitions are considered in the framework of the three temperature model and contribute to the understanding of the demagnetization mechanisms [4].

It is more challenging to study demagnetization and phase transitions in materials with an antiferromagnetic exchange interaction. Ferrimagnetic materials that exhibit unusual phases in their phase diagrams make it more accessible and can reveal an unpredictable result as was with amorphous ferrimagnetic TbFeCo film [44, 45]. Above $T_{C1} \approx 420$ K there is an amorphous paramagnetic phase, however, with further heating, it gains a crystalline structure and becomes ferrimagnetic again at $T_{ac} \approx 570$ K. Laser-induced magnetization dynamics was observed in the vicinity of every transition (across T_{C1}, T_{ac} and the Curie temperature $T_{C2} \approx 720$ K). The crystallization occurred within 1 ps, however, the time of the transition to the paramagnetic state (full demagnetization across T_{C1}) was found to be ~ 10 ps. So, the transition takes place without a transition to an intermediate paramagnetic phase.

Apart from that, the other important term that can be modified during laser irradiation, is anisotropy. As was discussed previously, the anisotropy term is responsible for the direction of $\vec{M}$ and $\vec{L}$. It means that alternation of the anisotropy can induce profound effects, such as magnetization reorientation.

One of the prominent examples of the excited dynamics through the different antiferromagnetic phases is the spin reorientation by 90 degrees in $TmFeO_3$ [46]. The change of the equilibrium position for the magnetization is triggered by the modified anisotropy field, which in the vicinity of this transition is sensitive to the temperature change. Then the antiferromagnetic vector aims to reorient to this new position via the precessional motion.

Ferrimagnetic materials sometimes show a magnetization and angular momentum compensation temperature. The intricate impact of the laser in the vicinity of those temperatures [47] evolves in the reversal of $\vec{L}$, all-

optical magnetization switching and high-speed domain wall motion.

Iron garnets are very prominent insulating materials that can be manufactured to obtain compensation at a desired temperature [48]. Laser-induced magnetization heating through the compensation temperature was established a long time ago and proposed for the realization of a magneto-optical memory [49, 50]. The observations were done with a temporal resolution of μs. Only after 40 years with the development of ultrafast techniques it was possible to find out the nonthermal effects of the anisotropy change that led to switching on a fs timescale [51]. Thus, already at the timescale of the electronic transitions, it is possible to non-dissipatively manipulate the magnetic order in garnets in a wide range of optical parameters [52]. Still, the actual role of compensation temperatures in these materials is not yet fully clear. In GdFeCo alloys the frequency of the magnetization precession was drastically increased when the material was heated above the compensation temperature [53] and the complicated mechanism and different magnetization dynamics of the sublattices were revealed later [54].

In the presence of an external magnetic field, it is possible to observe the dynamics across different antiferromagnetic phases such as collinear and noncollinear ones. The dynamics below and above the spin-flop transition in ferrimagnetic GdFeCo show remarkable differences [55]. The demagnetization of the rare-earth sublattice caused the transition metal sublattice to reorient to a new equilibrium position. The dynamics appeared to be sensitive to the angle between the sublattices and was suppressed at higher magnetic field strength. The follow-up experiment was conducted on TbFeCo, where the signal from different sublattices was probed at a specific wavelength and the dynamics of the rare-earth sublattice was found to be significantly slower than the metallic one. The demagnetization in this case led to a heavily damped precession and a slow-down of the dynamics in the canted antiferromagnetic phase [56].

Thermal expansion or contraction coming from the local heating also influences the anisotropy and can be essential for magnetostructural transitions, like the one observed in FeRh. FeRh is antiferromagnetic at low temperatures and becomes ferromagnetic far below it loses order at the Curie temperature (see Fig. 1.6). Despite the material being rather simple in its structure, the origin of this transformation is highly debated and attracts a lot of attention in the scientific community [57]. By investigating this transition we can shed light on the mechanisms of magnetoelastic transitions in general. Besides that, the particular example of FeRh has a large magnetic moment in the FM phase ($\sim 4\mu_{\mathrm{B}}$) and an easily reachable temperature of the phase transition (~ 370 K).

By illumination of FeRh with a strong and short laser pulse, it is possible to heat the material across the AFM-FM phase transition temperature. Then ultrafast spectroscopy can detect how fast the ferromagnetic order is

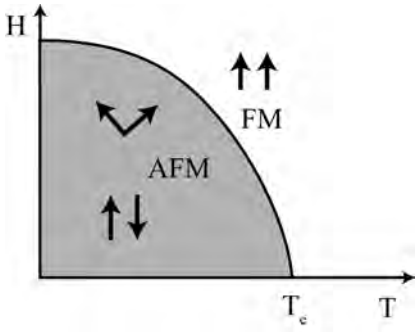

Figure 1.6: A schematic representation of the field-temperature phase diagram of FeRh, exhibiting an AFM phase at low temperatures and fields and a FM phase at high temperatures or magnetic fields.

built up. However, similar types of experiments showed diverse results. In some groups, the transition was observed on a timescale of a few hundred femtoseconds when they looked at the MOKE response [58]. Other groups stated that it actually happens much faster either in the electronic system of the material on a sub ps timescale [59] or in the magnetic one at the same time [60] or after a few tens of ps [61]. Some experiments also measured the response of the crystal lattice as the transition in FeRh is magnetoelastic, i.e. the unit cell expands by 3% at the phase transition. It is reported that significant structural changes occur on a timescale of hundreds of picoseconds [62]. However, afterwards, lattice dynamics was already registered on a ps timescale through XAS measurements [63] and even faster in XRD [64]. The rising controversy leads to many open questions related to how this phase transition evolves in FeRh.

Interaction of the exciting laser pulse with the magnetic medium can lead to various effects that can be properly studied only on a short timescale of perturbation. It is clear that generally, H plays a decisive role in F, however how it affects the ultrafast magnetization dynamics we still have to investigate.

1.4 Scope of this thesis

The thesis is dedicated to the poorly studied field of ultrafast magnetism across the rich phase diagram of magnets with antiferromagnetic coupling. It also discusses canted states of antiferromagnetic and ferrimagnetic materials, that are hard to reach with moderate external magnetic fields. In order to find an answer to how spins undergo reversal when high magnetic fields are applied, and what are the intricacies of the transition process from an antiferromagnetic to a ferromagnetic state we will employ the ultrafast

spectroscopy technique in high magnetic fields.

In Chapter 2 of this thesis, the experimental methods are introduced in detail. First, we describe static magnetization measurement techniques employed in the study such as the magneto-optical Kerr effect, SQUID and XMCD. Afterwards, the concept of the pump-probe scheme is presented. The Chapter is finalized with a description of the available tools for measurements at HFML-FELIX and the peculiarities of the experiment preparation.

Chapter 3 presents the study of laser-induced dynamics within collinear and non-collinear ferrimagnetic phases across the magnetization compensation temperature. Employing ultrafast heating of insulating LuIG, we will see whether the spin reorientation can be observed on a sub-ns timescale.

Chapters 4,5 and 6 will consider the laser-induced AFM to FM phase transition in FeRh. The peculiarities of this intriguing phenomenon are investigated in a wide range of external magnetic fields and temperatures. The characterization of the transition is also carried out in statics and compared between different measurement techniques.

Chapter 4 raises the question of the existence of a spin-flop transition of the antiferromagnetic FeRh at low temperatures and large magnetic fields. By the systematic study of the phase diagram, we are going to reveal all types of magnetization dynamics depending on the initial and the final magnetic state.

Follow-up experiments on a FeRh film are described in Chapter 5, where we include an additional parameter in the study of spin dynamics. We will investigate whether the ultimate speed of the phase transition can be modified under the application of strain. Also, we will consider other effects provoked by externally applied strain in regard to AFM-to-FM phase transition in FeRh.

The final sets of experiments presented in Chapter 6 are dedicated to the influence of the film thickness on the characteristic time and amplitude of the transient MOKE related to the nucleation and growth of FM domains at the AFM-to-FM phase transition and the full development of the Fm phase. Moreover, we will consider the oscillatory behaviour of the first stages of the laser-excited phase transition in films of various thicknesses.

To conclude the thesis we summarize the studies and provide a general outlook for further investigations in the area of magnetic phase transitions triggered by an ultrafast laser pulse.

Bibliography

[1] P. J. Hore and H. Mouritsen, Annual Review of Biophysics **45**, 299 (2016), ISSN 1936-122X, 1936-1238.

[2] C. J. White, A. Burrows, M. S. B. Coleman, and D. Vartanyan, The Astrophysical Journal **926**, 111 (2022), ISSN 0004-637X.

[3] J.-Y. Bigot, M. Vomir, and E. Beaurepaire, Nature Physics **5**, 515 (2009), ISSN 1745-2481.

[4] A. Manchon, Q. Li, L. Xu, and S. Zhang, Physical Review B **85**, 064408 (2012).

[5] S. Mathias, C. La-O-Vorakiat, P. Grychtol, P. Granitzka, E. Turgut, J. M. Shaw, R. Adam, H. T. Nembach, M. E. Siemens, S. Eich, et al., Proceedings of the National Academy of Sciences **109**, 4792 (2012), ISSN 0027-8424, 1091-6490.

[6] C. D. Stanciu, F. Hansteen, A. V. Kimel, A. Kirilyuk, A. Tsukamoto, A. Itoh, and Th. Rasing, Physical Review Letters **99**, 047601 (2007), ISSN 0031-9007, 1079-7114.

[7] T. Ostler, J. Barker, R. Evans, R. Chantrell, U. Atxitia, O. Chubykalo-Fesenko, S. El Moussaoui, L. Le Guyader, E. Mengotti, L. Heyderman, et al., Nature Communications **3**, 666 (2012), ISSN 2041-1723.

[8] Y. Shiota, T. Nozaki, F. Bonell, S. Murakami, T. Shinjo, and Y. Suzuki, Nature Materials **11**, 39 (2012), ISSN 1476-4660.

[9] N. J. Poulis, J. van den Handel, J. Ubbink, J. A. Poulis, and C. J. Gorter, Physical Review **82**, 552 (1951).

[10] F. B. Anderson and H. B. Callen, Physical Review **136**, A1068 (1964).

[11] L. Seabra, T. Momoi, P. Sindzingre, and N. Shannon, Physical Review B **84**, 214418 (2011).

[12] H.-F. Li, npj Computational Materials **2**, 1 (2016), ISSN 2057-3960.

[13] R. S. M. Rikken, R. J. M. Nolte, J. C. Maan, J. C. M. van Hest, D. A. Wilson, and P. C. M. Christianen, Soft Matter **10**, 1295 (2014).

[14] C. Kittel, *Introduction to Solid State Physics* (Wiley, 1986), ISBN 978-0-471-81636-2.

[15] J. Stöhr and H. Christoph Siegmann, *Magnetism: From Fundamentals to Nanoscale Dynamics* (Springer, Berlin, Heidelberg, 2006), ISBN 978-3-540-30282-7.

[16] D. J. Griffiths and D. F. Schroeter, *Introduction to Quantum Mechanics* (Cambridge University Press, 2018), ISBN 978-1-108-10034-2.

[17] K. Bán, A. Lovas, J. Kovac, and L. Novák, Proceedings of the 23rd International Colloquium of Advanced Manufacturing and Repair Technologies in Vehicle Industry (2006).

[18] R. C. Wayne and F. A. Smith, Journal of Physics and Chemistry of Solids **30**, 183 (1969), ISSN 0022-3697.

[19] T. Eriksson, L. Bergqvist, T. Burkert, S. Felton, R. Tellgren, P. Nordblad, O. Eriksson, and Y. Andersson, Physical Review B **71**, 174420 (2005).

[20] L. D. Landau, E. M. Lifshitz, and L. P. Pitaevskii, *Electrodynamics of Continuous Media: Volume 8* (Elsevier Science, 1995), ISBN 978-0-7506-2634-7.

[21] L. D. Landau and E. Lifschitz, *Statistical Physics*, https://shop.elsevier.com/books/statistical-physics/landau/978-0-08-057046-4 (1980).

[22] I. S. Jacobs, Journal of Applied Physics **32**, S61 (2009), ISSN 0021-8979.

[23] U. Köbler and A. Hoser, Solid State Communications **142**, 350 (2007), ISSN 0038-1098.

[24] D. Chen, Y. Xu, S. Tong, W. Zheng, Y. Sun, J. Lu, N. Lei, D. Wei, and J. Zhao, Physical Review Materials **6**, 014402 (2022).

[25] M. Guillot and H. Le Gall, physica status solidi (b) **77**, 121 (1976), ISSN 1521-3951.

[26] T. Goto, K. Nakao, and N. Miura, Physica B: Condensed Matter **155**, 285 (1989), ISSN 0921-4526.

[27] V. Baltz, A. Manchon, M. Tsoi, T. Moriyama, T. Ono, and Y. Tserkovnyak, Reviews of Modern Physics **90**, 015005 (2018).

[28] P. Němec, M. Fiebig, T. Kampfrath, and A. V. Kimel, Nature Physics **14**, 229 (2018), ISSN 1745-2481.

[29] O. Gomonay, V. Baltz, A. Brataas, and Y. Tserkovnyak, Nature Physics **14**, 213 (2018), ISSN 1745-2481.

[30] H. Y. Yuan, Z. Yuan, R. A. Duine, and X. R. Wang, Europhysics Letters **132**, 57001 (2021), ISSN 0295-5075.

[31] S.-H. Yang, K.-S. Ryu, and S. Parkin, Nature Nanotechnology **10**, 221 (2015), ISSN 1748-3395.

[32] N. Thielemann-Kühn, D. Schick, N. Pontius, C. Trabant, R. Mitzner, K. Holldack, H. Zabel, A. Föhlisch, and C. Schüßler-Langeheine, Physical Review Letters **119**, 197202 (2017), ISSN 0031-9007, 1079-7114.

[33] A. Ross, R. Lebrun, O. Gomonay, D. A. Grave, A. Kay, L. Baldrati, S. Becker, A. Qaiumzadeh, C. Ulloa, G. Jakob, et al., Nano Letters **20**, 306 (2020), ISSN 1530-6984.

[34] K.-J. Kim, S. K. Kim, Y. Hirata, S.-H. Oh, T. Tono, D.-H. Kim, T. Okuno, W. S. Ham, S. Kim, G. Go, et al., Nature Materials **16**, 1187 (2017), ISSN 1476-4660.

[35] C. S. Davies, G. Bonfiglio, K. Rode, J. Besbas, C. Banerjee, P. Stamenov, J. M. D. Coey, A. V. Kimel, and A. Kirilyuk, Physical Review Research **2**, 032044 (2020).

[36] B. A. Ivanov, Low Temperature Physics **40**, 91 (2014), ISSN 1063-777X.

[37] J. Han, R. Cheng, L. Liu, H. Ohno, and S. Fukami, Nature Materials **22**, 684 (2023), ISSN 1476-4660.

[38] C. H. De Groot and K. De Kort, Journal of Applied Physics **85**, 8312 (1999), ISSN 0021-8979, 1089-7550.

[39] A. V. Kimel, A. M. Kalashnikova, A. Pogrebna, and A. K. Zvezdin, Physics Reports **852**, 1 (2020), ISSN 0370-1573.

[40] E. Beaurepaire, J.-C. Merle, A. Daunois, and J.-Y. Bigot, Physical Review Letters **76**, 4250 (1996).

[41] E. Carpene, E. Mancini, C. Dallera, M. Brenna, E. Puppin, and S. De Silvestri, Physical Review B **78**, 174422 (2008).

[42] P. M. Oppeneer and A. Liebsch, Journal of Physics: Condensed Matter **16**, 5519 (2004), ISSN 0953-8984.

[43] T. Ogasawara, K. Ohgushi, Y. Tomioka, K. S. Takahashi, H. Okamoto, M. Kawasaki, and Y. Tokura, Physical Review Letters **94**, 087202 (2005).

[44] M. B. Agranat, S. I. Anhitkov, A. V. Kirillin, V. E. Fortov, S. I. Anisimov, A. B. Granovskiĭ, and P. S. Kondratenko, JETP Letters **67**, 953 (1998), ISSN 1090-6487.

[45] A. Kirilyuk, A. V. Kimel, and T. Rasing, Reviews of Modern Physics **82**, 2731 (2010).

[46] A. V. Kimel, A. Kirilyuk, A. Tsvetkov, R. V. Pisarev, and T. Rasing, Nature **429**, 850 (2004), ISSN 1476-4687.

[47] A. Kirilyuk, A. V. Kimel, and T. Rasing, Reports on Progress in Physics **76**, 026501 (2013), ISSN 0034-4885.

[48] T. Bayaraa, C. Xu, D. Campbell, and L. Bellaiche, Physical Review B **100**, 214412 (2019).

[49] J. T. Chang, J. F. Dillon, Jr., and U. F. Gianola, Journal of Applied Physics **36**, 1110 (1965), ISSN 0021-8979.

[50] J.-P. Krumme, P. Hansen, and K. Witter, Journal of Applied Physics **47**, 3681 (1976), ISSN 0021-8979.

[51] F. Hansteen, A. Kimel, A. Kirilyuk, and T. Rasing, Physical Review Letters **95**, 047402 (2005).

[52] A. Stupakiewicz, K. Szerenos, M. D. Davydova, K. A. Zvezdin, A. K. Zvezdin, A. Kirilyuk, and A. V. Kimel, Nature Communications **10**, 612 (2019), ISSN 2041-1723.

[53] C. D. Stanciu, A. V. Kimel, F. Hansteen, A. Tsukamoto, A. Itoh, A. Kirilyuk, and Th. Rasing, Physical Review B **73**, 220402 (2006), ISSN 1098-0121, 1550-235X.

[54] I. Radu, K. Vahaplar, C. Stamm, T. Kachel, N. Pontius, H. A. Dürr, T. A. Ostler, J. Barker, R. F. L. Evans, R. W. Chantrell, et al., Nature **472**, 205 (2011), ISSN 1476-4687.

[55] J. Becker, A. Tsukamoto, A. Kirilyuk, J. C. Maan, Th. Rasing, P. C. M. Christianen, and A. V. Kimel, Physical Review Letters **118**, 117203 (2017), ISSN 0031-9007, 1079-7114.

[56] A. Pogrebna, K. Prabhakara, M. Davydova, J. Becker, A. Tsukamoto, Th. Rasing, A. Kirilyuk, A. K. Zvezdin, P. C. M. Christianen, and A. Kimel, Physical Review B **100**, 174427 (2019), ISSN 2469-9950, 2469-9969.

[57] L. H. Lewis, C. H. Marrows, and S. Langridge, Journal of Physics D: Applied Physics **49**, 323002 (2016), ISSN 0022-3727, 1361-6463.

[58] N. Awari, A. Semisalova, J.-C. Deinert, K. Lenz, J. Lindner, E. Fullerton, V. Uhlíř, J. Li, B. Clemens, R. Carley, et al., Applied Physics Letters **117**, 122407 (2020), ISSN 0003-6951, 1077-3118.

[59] F. Pressacco, D. Sangalli, V. Uhlíř, D. Kutnyakhov, J. A. Arregi, S. Y. Agustsson, G. Brenner, H. Redlin, M. Heber, D. Vasilyev, et al., Nature Communications **12**, 5088 (2021), ISSN 2041-1723.

[60] G. Ju, J. Hohlfeld, B. Bergman, R. J. M. van de Veerdonk, O. N. Mryasov, J.-Y. Kim, X. Wu, D. Weller, and B. Koopmans, Physical Review Letters **93**, 197403 (2004), ISSN 0031-9007, 1079-7114.

[61] G. Li, R. Medapalli, J. H. Mentink, R. V. Mikhaylovskiy, T. G. H. Blank, S. K. K. Patel, A. K. Zvezdin, Th. Rasing, E. E. Fullerton, and A. V. Kimel, Nature Communications **13**, 2998 (2022), ISSN 2041-1723.

[62] F. Quirin, M. Vattilana, U. Shymanovich, A.-E. El-Kamhawy, A. Tarasevitch, J. Hohlfeld, D. von der Linde, and K. Sokolowski-Tinten, Physical Review B **85**, 020103 (2012), ISSN 1098-0121, 1550-235X.

[63] I. Radu, C. Stamm, N. Pontius, T. Kachel, P. Ramm, J.-U. Thiele, H. A. Dürr, and C. H. Back, Physical Review B **81**, 104415 (2010), ISSN 1098-0121, 1550-235X.

[64] M. Grimes, H. Ueda, D. Ozerov, F. Pressacco, S. Parchenko, A. Apseros, M. Scholz, Y. Kubota, T. Togashi, Y. Tanaka, et al., Scientific Reports **12**, 8584 (2022), ISSN 2045-2322.

Chapter 2

Experimental techniques

This chapter serves as a comprehensive introduction to the experimental techniques and methodologies employed throughout this thesis. First, we describe the details of magnetization measurements, an essential foundation for the subsequent chapters. We discuss the different techniques utilized in the experiments detailed in the following sections. Subsequently, we focus our attention on the combination of the ultrafast pump-probe experimental set-up in the visible spectrum with the high magnetic field installation. This unique instrumentation is situated in the HFML-FELIX laboratory in Nijmegen and enables us to investigate spin dynamics within magnetic systems while subjecting them to external magnetic fields of up to 30 T. We provide the details of the available equipment and configurations of the setup.

2.1 Magnetization measurements

There are a number of direct and indirect methods that are able to measure magnetization in a material. Direct techniques that can give absolute units of the magnetization are superconducting quantum interface device (SQUID) experiments, vibrating sample magnetometry (VSM), torque-magnetometry and AC-susceptibility. Indirect techniques that can track the behaviour of the magnetization with good precision, but in arbitrary units are magnetotransport, dilatometry, (X-ray) magnetic circular dichroism (MCD) and other magneto-optical techniques that rely on effects such as the Kerr and Faraday effect. Some of these techniques can measure the net magnetization of a sample or a film, whereas others are capable of determining the magnetization of sublattices in a magnetic crystal or the magnetization in an antiferromagnetic state. In the following, we describe the techniques that are used in this thesis.

2.1.1 SQUID

A superconducting quantum interface device is a magnetometer based on Josephson junctions in a superconducting ring and is commercially available as an automated system produced by several companies. It measures the current induced by a magnetic flux with the precision of a few femtotesla. This high sensitivity is an advantage and disadvantage at the same time because it makes the measurements susceptible to backgrounds and artefacts in the signal coming from defects and interfaces in the material under study, especially when it is composed of multiple layers. Therefore, one should always be careful in separating the contribution of the different components, such as substrates, capping layers and interfaces.

Once the background or spurious contributions are subtracted from the measured magnetization $\vec{M}$, expressed in emu, it has to be divided by the weight of the magnetic material. It can also be converted to the magnetic moment μ per ion or unit cell:

$$\mu(\mu_{\mathrm{B}}) = \frac{M \times W_{\mathrm{M}}}{\mu_{\mathrm{B}} N_{\mathrm{A}}}, \tag{2.1}$$

where $\mu_{\mathrm{B}} = 9.274 \times 10^{-21}$emu is the Bohr magneton, N_{A} is the Avogadro constant and W_{M} is the molecular weight, expressed in g/mol.

The data presented in the following chapters were obtained at the Institute of Problems of Chemical Physics of the Russian Academy of Science using a Quantum Design SQUID in the reciprocating sample option mode, which means that the sample was oscillating between the superconducting pick-up coils.

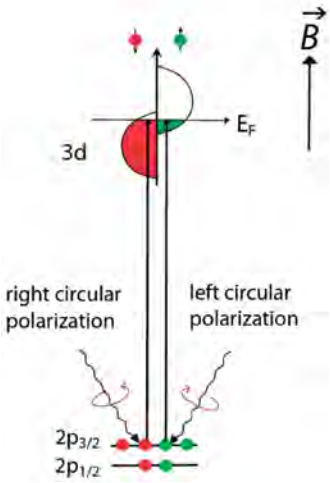

Figure 2.1: Illustration of the helicity-dependent X-ray photon absorption at the spin-orbit split $L_{2,3}$ edge of a transition metal.

2.1.2 XMCD

X-ray Magnetic Circular Dichroism is an indirect technique of monitoring magnetization. The overall sensitivity of the XMCD method is less than that of a SQUID, but XMCD can detect signals down to $0.001\mu_B$ [1]. On the other hand, XMCD has several advantages, mainly related to the element specificity of the method. The XMCD signal at a given energy is related to a certain absorption line of electrons in a particular shell of a particular element present in the material. So normally, before the actual XMCD measurements are performed, the X-ray absorption spectrum of an element under study is recorded in the vicinity of a core-shell electronic transition. This is called X-ray Absorption Near Edge Spectroscopy (XANES). The absorption integral intensities in XANES spectra reflect the partial density of empty states. As such, interfaces and substrates play a lesser role, unless it induces a magnetic moment in the studied material.

XMCD detects the difference between the absorption spectra of left and right circularly polarized X-ray beams, taken at an applied magnetic field, and is sensitive to the magnetic properties of a specific element.

In the case of K-edge transitions from a 1s state, occurring with spin conservation, a circularly polarized X-ray photon transfers its whole momentum into the orbital magnetic moment. The XMCD signal then arises from the local exchange fields of the final valence band state [2, 3]. In the presence of spin-orbit coupling, such as in $L_{2,3}$ edge transitions, the 2p electrons are excited to higher energy levels like 3d orbitals. Spin-orbit coupling causes a split into L_2 and L_3 edges due to different spin states. Circularly

polarized light, depending on its helicity, can influence the spin moment of 2p photoelectrons during these transitions. Thus, the $L_{2,3}$ edges are particularly sensitive to XMCD, offering insights into the material's magnetic moments (see Fig. 2.1).

Moreover, if the transition arose due to spin-orbit coupling and both spectra of the spin-orbit split edge are available, with XMCD it is possible to disentangle the spin and orbital moments of the ground state. From magneto-optical sum rules, it is possible to relate the dichroism intensity to the ground state expectation values of orbital and spin moments [4, 5]. It requires an integration over the whole absorption spectrum and also the XMCD spectrum. The way to estimate that for a specific excitation is well described for the dipole allowed transitions in multiple sources [1, 4–7].

Performing such a calculation it is possible to relate the XMCD measurement to the total magnetic moment value and/or spin and orbit moment. However, due to the complexity of the procedure and its interpretation, and the necessity to measure the spectrum at each external magnetic field strength, it is usually accepted to give the normalized XMCD vs. magnetic field dependencies that reflect the presence of the net magnetic moment of the particular ions.

2.1.3 MOKE

Other optical effects can be used to indirectly measure magnetization. Examples include the Faraday effect, Kerr effect, ellipticity, and linear dichroism. These effects occur because magnetized materials exhibit a specific optical response depending on the polarization of the incoming light. The variations in how right- and left-circularly polarized light is reflected, absorbed and transmitted lead to profound changes in the light's intensity and polarization after interacting with the material. This behaviour is similar to the origin of XMCD signals, as described above, but now occurs in the visible region of the optical spectrum.

The Kerr effect is a very convenient way to study magnetization dynamics in magnetic materials. Unlike the other mentioned magneto-optical effects, it is highly sensitive to changes in the amplitude and direction of the magnetization at the surface of a material. This provides real-time information about how the magnetization evolves over time after the local, pulsed optical excitation at the surface, making it suitable for investigating dynamic processes such as domain switching, ultrafast magnetization dynamics, and other rapid magnetic phenomena.

Types of MOKE

We will focus on the magneto-optical Kerr effect (MOKE), but if one needs to measure in the transmission geometry it is convenient to employ the Faraday effect. There are three types of MOKE depending on the orienta-

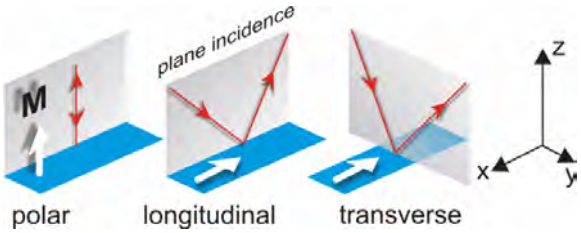

Figure 2.2: Illustration of different MOKE configurations: (a) polar, (b) longitudinal, (c) transverse. Adapted from [8]

.

tion of the wavevectors $\vec{k}$ of the incoming and reflected light beams and the orientation of the magnetization in the material: polar, longitudinal and transverse (see Fig. 2.2). Polar and longitudinal MOKE manifest themselves as a rotation of the polarization plane of light after its interaction with the medium, with out-of-plane (polar) or in-plane (longitudinal) magnetization. Transverse MOKE leads to changes in the intensity of light reflected from a material with in-plane magnetization.

Formalism of dielectric permittivity

To describe the interaction of the medium with the light we use the linear approximation of the electrical displacement $\vec{D} = \varepsilon_0 \varepsilon_{ij} \vec{E}$. Here the incoming light is considered as a monochromatic electromagnetic wave with an electric field $\vec{E}$. The properties of the medium are given by the tensor ε_{ij}, which is modified in the presence of a magnetization. ε_0 is the dielectric constant of vacuum. The tensor expresses symmetries of the medium and due to Onsager's principle [9], generally $\varepsilon_{ij} = \varepsilon_{ji}$. However, in the presence of a magnetic field, an antisymmetric part should be added to the tensor. In this thesis, we have primarily used polar MOKE, as it generally gives larger signals of polarization rotation. For this type of geometry, with light propagating in the $-z$-direction along the normal of the sample with an out-of-plane magnetization with amplitude M, the formalism is as follows:

$$\varepsilon_{ij} = \begin{bmatrix} \varepsilon_{xx}(\vec{M}) & \varepsilon_{xy}(\vec{M}) & 0 \\ -\varepsilon_{xy}(\vec{M}) & \varepsilon_{yy}(\vec{M}) & 0 \\ 0 & 0 & \varepsilon_{zz}(M) \end{bmatrix} \tag{2.2}$$

The diagonal components can depend on $\vec{M}$ and are an even function of it. The $xy-$ components are complex values and odd functions of $\vec{M}$. Those components affect the propagation speed and the reflection coefficients, which are different for the two opposite circular polarization components of the light wave, giving rise to the Faraday (in transmission) and polar MOKE (in reflection) effects.

The magneto-optical Faraday rotation angle can be expressed as [10]:

$$\theta_{\mathrm{F}} = V \cdot B \cdot d \tag{2.3}$$

Thus, it is proportional to the magnetic flux density B and the length of the beam path through the medium d. The coefficient V is called Verde constant and reflects the material parameters at the specific light wavelength. This expression shows indeed that the polarization rotation is an indirect measure of the magnetization. Values of the Kerr rotation for different media cannot be directly traced back to their magnetization values, because the connection of ε to $\vec{M}$ can be different for each medium and can have a distinct spectral dependence.

Detection of the polarization rotation

The polarization of the reflected beam cannot be detected directly. A photodiode measures the intensity of the light and to transform it into a polarization rotation we need to put an analyser in front of the detector. Then depending on the orientation of the axis of that analyser with the polarization plane of the light wave, the registered intensity will be: $I = I_0 \cos\phi$. Using photo-detectors, the light intensity is converted to electric current, which is further detected using the lock-in technique. Ideally, the sensitivity will be limited by the shot noise, defined by short-current in electric circuits $\sqrt{2e\Delta f}$, where e is the electronic charge, and Δf is the considered frequency width. To maximize the sensitivity of the intensity change to the polarization change and at the same time not to lose the sensitivity due to fluctuations of the laser intensity (laser noise), we have to either work with the optimal angle of the analyser, which is close to 90° or use a balanced scheme. In the latter case, we additionally compensate for the intensity fluctuations in the light beam [11]. For the realization of this scheme, two detectors are employed (Figure 2.3). Instead of the usual analyser, a Wollaston prism is used, which splits the light beam into two orthogonal linear polarization components. Then at $\phi = 45°$, the intensities in the two paths will be equal unless there is a polarization rotation of the reflected light induced by the magnetization in the sample arising from the Faraday or Kerr effect.

Typical experimental set-up for polar MOKE measurements

A typical polarimeter generally consists of a light source, polarizer, analyzer and detector. To improve the signal-to-noise often modulation techniques are used, such as polarization modulation with a photoelastic modulator, an acousto-optic modulator, magneto-optical modulator (Faraday cell) or an electro-optic modulator (Pockels cell). The choice for any of these modulators depends on the specific need in the frequency of the modulation and the spectral range. The highest frequency and fastest response time can

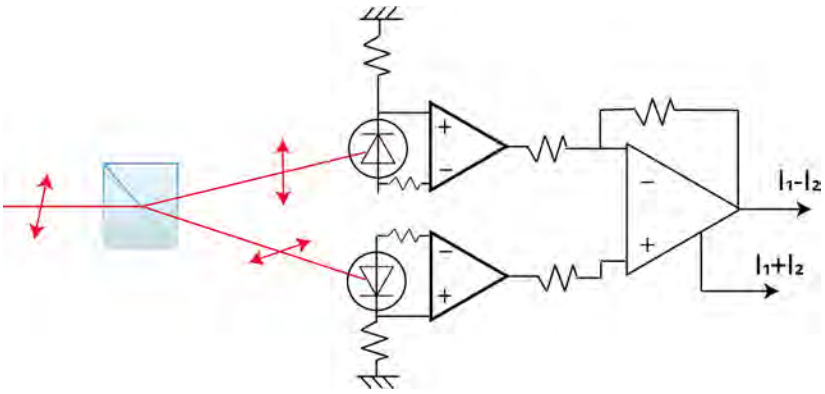

Figure 2.3: Differential scheme for balanced detection to measure polarization rotation. A Wollaston prism splits the light into beams with orthogonal linear polarization, which are detected by two photdiodes. Using a differential amplifier the sum and difference intensities can be monitored, as a measure of respectively the total intensity and the polarization rotation.

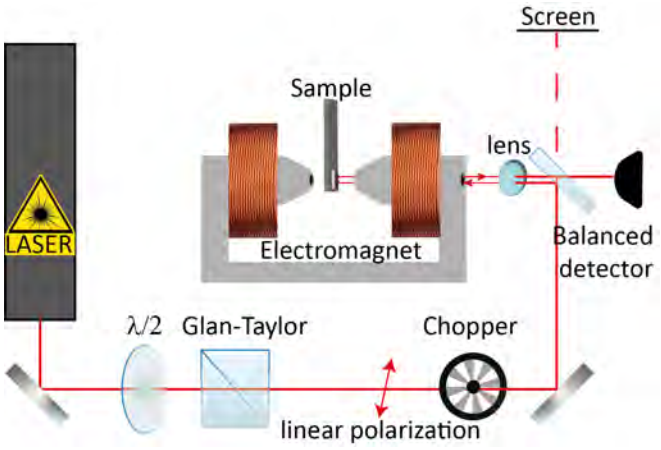

Figure 2.4: Experimental set-up for polarimetry.

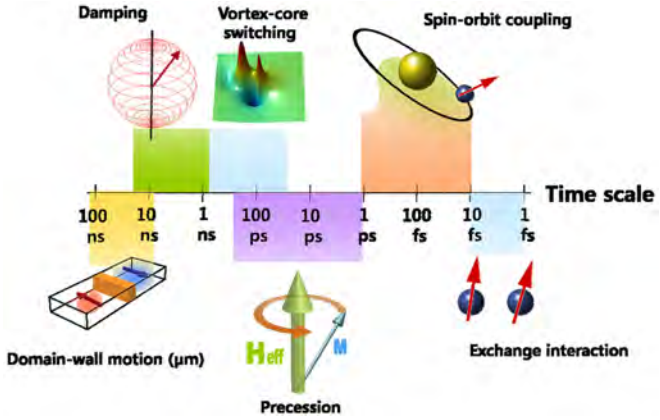

Figure 2.5: Illustration of the time-scale of magnetic phenomena. Adapted from [12]

be reached using Pockels cells, which is one of the components of ultrafast lasers, but because of their high cost, they are only used in cases where this fast response is essential. For our measurement of the Kerr rotation, we used a more simple device - a mechanical chopper. It modulates the intensity of the incoming light beam, up to frequencies of 500 Hz with a 50% duty cycle.

The setup employed for the static MOKE measurements presented in the current thesis is shown in Figure 2.4. We used a continuous wave HeNe laser with a wavelength of 632.8 nm. The beam was passed through a half-waveplate ($\lambda/2$) and a Glan-Taylor linear polarizer, to control the intensity and polarization of the incident light. To realize the polar MOKE configuration we used a 50/50 reflection/transmission beamsplitter, to guide the incoming light to the sample and the reflected light to the balanced detector. The magnetization in the sample was induced by an electromagnet with ferromagnetic iron cores with a maximum field strength of 1.8 T.

2.2 Ultrafast Spectroscopy set-up

2.2.1 Time-resolution in magnetization measurements obtained by light

Performing time-resolved measurements of the magnetization is a very powerful method to obtain information about the magnetic properties of materials. The characteristic timescales of different magnetic interactions, defined as interaction energy divided by the Planck constant, vary significantly. The strongest magnetic interaction, the exchange interaction, has the characteristic timescale of the order of femtoseconds. On the other

side, the terrestrial magnetic fields vary on a timescale of up to 50 million years [13]. As such, adding time resolution to the magnetization experiment opens up an opportunity to study the processes of distinct magnetic interactions, as illustrated in Figure 2.5.

In equilibrium, all systems are thermalised and it is possible to follow a particular property, like magnetization in our case, macroscopically. However, for a fast perturbation, it might take time to transfer the energy, or in the case of magnetization, the angular momentum, from one system to another, which is an inherent non-equilibrium process.

Classical thermodynamics cannot describe the processes on the subpicosecond level (Fig. 2.5), faster than the spin-orbit coupling and the exchange interaction. To describe such a system, it is usually divided into three reservoirs, i.e. the spins, the electrons and the lattice, where the temperature of each particular reservoir is considered separately, which is called the 3-temperature model [14].

Thus the processes that cause the magnetization of the medium to change, require an angular momentum transfer to the spin system. The resulting magnetization dynamics can be described by the Landau-Lifshitz equation (Chapter 1). This equation shows that to have a nonzero $\frac{d\vec{M}}{dt}$ requires a non-zero external or effective field and a net torque $\vec{M} \times \vec{H}$.

There are not many ways to trigger and detect processes on subpicosecond timescales, but optical spectroscopy using short light pulses can do this. The duration of the laser pulses defines the time resolution of the measurement. Ultrashort pulses can be readily generated nowadays by pulsed lasers and if needed to be compressed in time even more with external compressors and special fibres, however travelling big distances through the air the pulse can broaden in time. Usually, two light beams are used: one type to trigger the dynamics (excitation pump pulse) and the other to detect the changes (probe beam). The time difference between the arrival of the excitation pulse and the probe pulse can be changed by optical delay lines, to increase the optical path length for the probe or decrease the path length for the pump. In case of small signals, one set of pump-probe pulses is not sufficient, and multiple sets are used in a stroboscopic way with a repetition rate depending on the laser system. In this case it is assumed that after each pump-probe sequence the sample has relaxed back to the initial condition before the next pump pulse arrives.

The ability of MOKE as a measure of the real spin dynamics on ultrafast timescales is considered in Ref. [15]. It is found from first principle calculations in nickel that the magnetic and optic response has a one-to-one correspondence for pulses longer than 10 fs.

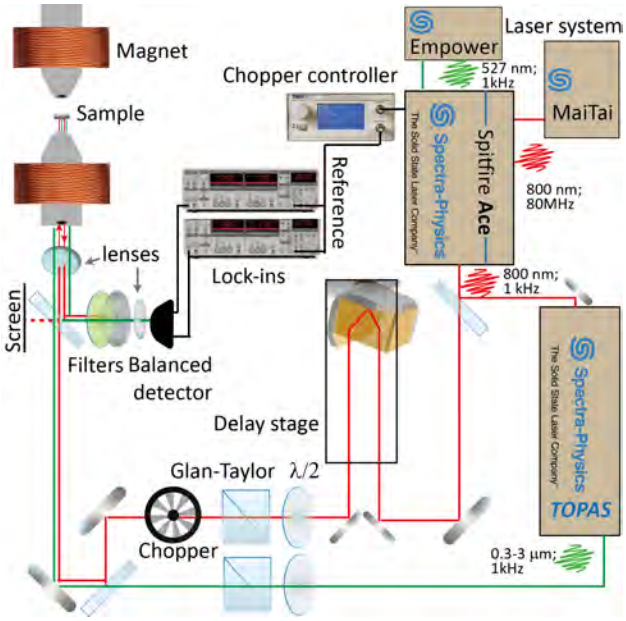

Figure 2.6: Scheme of the experimental realization of the pump-probe technique using a pulsed laser system.

2.2.2 Pump-probe scheme

The conceptual scheme of a two-coloured pump-probe MOKE experiment is shown in Figure 2.6. Two laser beams with different colours are directed onto the sample positioned in a magnet. One of them (the probe beam) is delayed using a retroreflector situated on a motor-driven delay stage. The power of the probe beam is set by a half waveplate ($\lambda/2$ and a Glan-Taylor linear polarizer in such a way that the intensity of the probe beam is significantly lower than that of the probe pulse. The probe beam is modulated by a mechanical chopper with a frequency of 500 Hz. The two beams are spatially overlapped at the beamsplitter and directed to the sample. A lens is used to focus both beams on the sample and after reflection to collimate the beam to guide it to the detection channel, which consists of a set of filters to cut the pump pulse and reduce the intensity of the signal beam to stay in the linear regime of the photodiodes. The signal at the chopper modulation frequency is filtered out by lock-in amplifiers that are connected to the intensity and polarization rotation channels of the balanced photodetector. The signals are recorded for every delay stage position converted in units of picoseconds.

The actual setup includes the following components:

1. Spectra-Physics laser system, starting with a light beam of a MaiTai Ti:Sapphire seed laser at 800 nm with a repetition rate of 80 MHz. Its pulses are amplified with a Spitfire ACE, a regenerative amplifier using a crystal as a gain medium. The crystal is situated in a resonator and the amount of passages through it is controlled by a Pockels cell. The crystal is pumped by an Empower Nd:YLF laser working at 527 nm and a repetition rate of 1 kHz. To obtain the second colour, we used an optical parametric amplifier, TOPAS prime, that can generate pulses in the wavelength range from 240 nm to 2600 nm. The extension of the TOPAS prime, NirUVis adds frequency mixing and separation of idler from the signal. The system is based on harmonic generation and sum frequency effects in the nonlinear crystals.

2. Delay stage from Physik Instrumente with C-863 Mercury Servo Controller allows to delay the beam for up to 3 ns.

3. Mechanical chopper MC2000 with ThorLabs controller that is responsible for the synchronization of the rotation frequency with the frequency of the laser.

4. Polarization optics, including half and/or quarter waveplates and Glan-Taylor polarizers. It allows to control the polarization state and power of the pump and probe beams separately.

5. Magnet, which has to produce an external magnetic field enough to induce the magnetization component in the sample in the direction corresponding to one of the MOKE configurations. We used either an electromagnet up to 1.8 T or a Florida-Bitter magnet up to 37 T.

6. Lenses before the sample and the detector.

7. Filters: Shortpass filter and Neutral Density filters if necessary.

8. Balanced detector with photodiodes for the visible range.

9. Lock-in amplifiers SR830 from Stanford Research Systems

2.2.3 Modulation and calibration

We use modulation of the laser beams by a mechanical chopper to increase the sensitivity of the measurement. Specifically, we separately measure the signal + background and the background alone to isolate the signal and achieve a higher signal-to-noise ratio. Every second pump pulse is cut with the mechanical chopper, meaning that the lock-in signal on the first harmonic (the repetition rate of the chopper) is the difference between the signal induced by the probe pulse that arrived shortly after the pump pulse and the signal due to the probe pulse that arrived in the absence of the

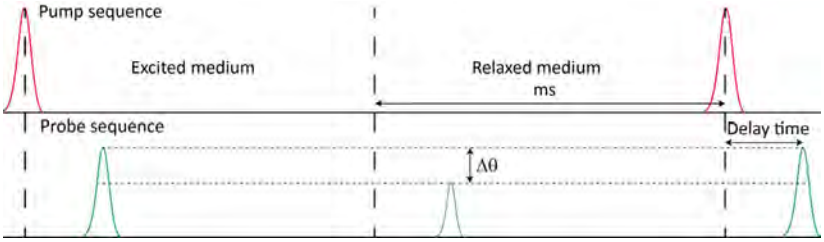

Figure 2.7: Illustration of the modulation with chopper

pump. This is exactly the change in the polarization rotation induced by the laser excitation (Fig. 2.7).

With the balanced detector, the intensity that we measure is proportional to the polarization rotation angle θ. As we use the Wollaston prism with 45° polarization orientation, the differential signal will be:

$$I_\theta = I_\mathrm{R}\cos^2(\theta+\pi/4) - I_\mathrm{R}\sin^2(\theta+\pi/4) = I_\mathrm{R}\sin(2\theta) \approx I_\mathrm{R}\cdot 2\theta \qquad (2.4)$$

Where I_R is the total intensity of the reflected light. Thus, to calibrate our signal we need to measure the total intensity of the reflected light I_R as well. This can be done on the double frequency 2ω, which is the repetition rate of the laser.

2.3 Instrumentation in High Magnetic Fields

At the High Magnetic Field Laboratory, ultrafast optical spectroscopy in the visible and near-infrared range can be performed on samples positioned in a Florida-Bitter magnet. This extends the possibility of studying ultrafast magnetization dynamics up to 37.5 T, where different magnetic phases can be achieved.

The combination is realized by directing the pump and probe beams in the centre of the magnet's bore, where the magnetic field strength is maximum (Fig. 2.8). The magnet is situated on the ground floor in the south magnet hall, right below the optical table on the first floor, and the beams are reflected down vertically in free space with the beamsplitter. Spatially overlapping beams reach the lens, just above the sample, with a focal length of 1 cm. The probe beam is focused into a 30 μm diameter spot on the sample surface. Due to chromatic aberrations, the pump beam has a slightly bigger spot size of 50 μm diameter. The reflected light is collected by the same lens and propagates back to the first floor, up to the mirror behind the beamsplitter. After that stage, the pump is filtered out, and the residual probe signal is registered with a balanced detector.

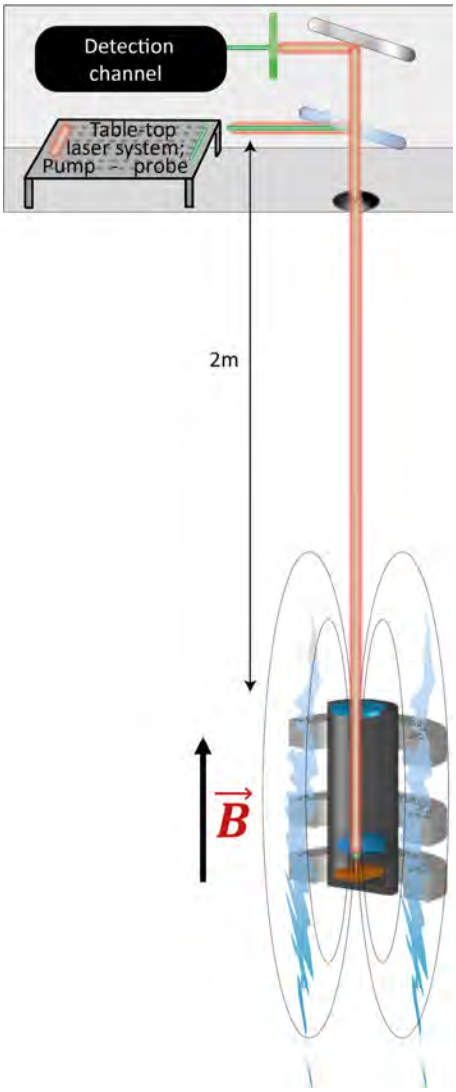

Figure 2.8: Sketch of the combination of the femtosecond pump-probe set-up with a 37.5 T Florida-Bitter magnet. The laser system is situated at the first floor of HFML, above the magnet in cell 2 on the ground floor.

2.3.1 Sample preparation and mechanical insert

The resulting polarization rotation is not entirely due to the MOKE signal of the sample, as the probe pulse propagates through a window at the top of the mechanical insert and the lens, which is also positioned in a magnetic field, causing an additional Faraday rotation. To this end, we compensate for this Faraday rotation in the lens, but to keep this field dependent background signal to a minimum, we use a special lens made of SFL6 glass, which has a low Faraday rotation.

To place the sample in the bore of the magnet and to be able to cool it down in temperature, a special liquid Helium bath cryostat and dedicated sample holders are used. The bath cryostat has a long narrow tail which fits in the bore of the magnet without touching it. It is non-magnetic up to the maximum field of the magnet. As we use free-beam optics and not fibers, any movement of the cryostat would cause a change in the optical signal, because the reflected beam would become misaligned. The best experimental results were obtained using a aluminum cryostat. The sample is mounted on a holder attached to a Carbon hollow insert. The insert is filled with Helium exchange gas to provide the required cooling. The distance from the centre of the magnetic field to the top of the cryostat has to be matched with the distance from the sample to the clamp between the sample chamber and the cryostat. This clamp can be shifted to allow precise positioning.

The mechanical insert has pins at the top, to which devices can be connected. The wires are rounding the tube down to the sample space. The devices have to be soldered and attached before each experiment. They include the resistance that has to be glued close to the sample and to make sure the distribution of the produced heat is homogeneous a second resistor is needed. In between them temperature sensor has to be installed. For our experiments, we use Cernox thermometers that are calibrated down to 4.2 K.

It has to be taken in mind that the shrinkage of all metallic parts due to the cooling leads to strains. Sample attachment has to be not extremely tight so as not to translate the strain from the thermal coefficient mismatch to the sample. At the same time, insufficient adhesion can lead to the movement of the magnetic sample in a sweeping magnetic field.

2.3.2 Polar MOKE implementation

The most straightforward configuration for the high field installation is the polar MOKE effect. The sample is fixed in the centre of a copper sample holder that can be screwed at the end of the carbon insert. The holder has a diameter of 13 mm and the sample has to fit in a circle of 12 mm in diameter. In this case the external magnetic field and the light wavevector are parallel to the normal of the sample surface (Faraday configuration).

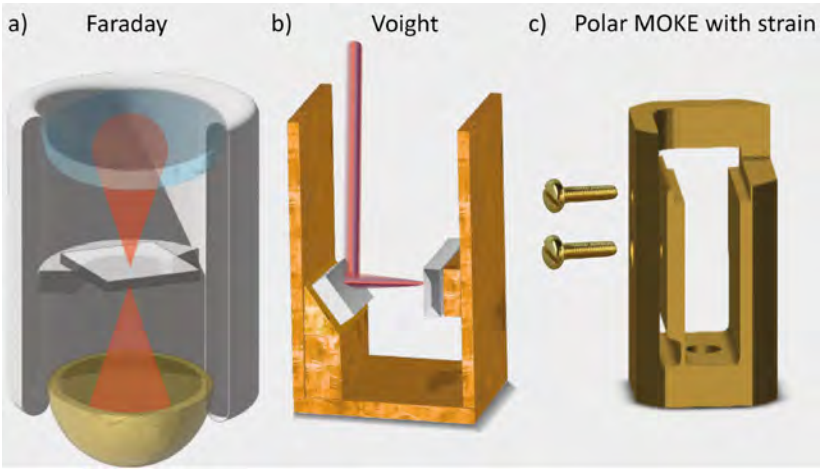

Figure 2.9: The sample holders compatible with the inserts that fit in the 32 mm bore of the 37.5 T Florida-Bitter magnet. Types of possible configurations for optical measurements: (a) Double transmission for the double Faraday effect; (b) Voigt geometry, where the sample plane is aligned along the external magnetic field; (c) Strain holder in polar MOKE configuration.

The position of the lens is defined before the sample is inserted in the cryostat with a cw laser. The reflected beam has to be well-collimated to reach the top of the mechanical probe. Apart from the simple copper holder, special sample holders, as shown in Figure 2.9, can be used, which are described in the next sections.

2.3.3 Faraday effect measurement

We developed a holder able to measure the Faraday effect in double transmission (Figure 2.9(a)). In this case, the natural optical activity is cancelled out and the Faraday effect is doubled. The focusing lens is positioned at 2 cm above a spherical mirror. The beam propagates through the sample, is reflected back by the spherical mirror, propagates once more through the sample and is collected by the lens. The focal distances of the mirror and lens are the same to ensure that the light propagates back the same way. A filter was inserted after the sample to prevent the transmitted pump beam to reach the sample a second time after ∼67 ps.

2.3.4 Voigt configuration holder

In the case when the magnetic field needs to be applied in the sample plane, a Voigt configuration holder is available (Figure 2.9(b)). It is developed in such a way that after a focusing lens, the beam reflects from a mirror at 45°.

The sample is attached to the wall and reflects the light back to the mirror, after which it is collected by the lens and guided back to the detector.

2.3.5 Application of strain

In Chapter 5 we performed an experiment in polar MOKE geometry with the application of strain. This was done using the holder schematically shown in Figure 2.9(c). Here the sample is clamped at the top part of the holder with two walls. By rotating the upper screw we could shift its position for a certain distance defined by the rotation angle of the screw. In this way, it is possible to push the wall towards the sample creating compression. The lower crew, on the other side, goes through the thread of the wall, pulling it away from the sample to the outer wall in that way inducing a tensile strain. The shift of the wall, which is attached to the sample can be calculated from the rotation angle of the screw allowing us to calibrate the amount of strain.

Bibliography

[1] A. Rogalev and F. Wilhelm, The Physics of Metals and Metallography **116**, 1285 (2015), ISSN 1555-6190.

[2] M. A. Laguna-Marco, C. Piquer, and J. Chaboy, Physical Review B **80**, 144419 (2009).

[3] F. Saito, T. Toyoda, T. Mori, M. Tanaka, K. Hirano, and S. Sasaki, Physica B: Condensed Matter **270**, 35 (1999), ISSN 0921-4526.

[4] P. Carra, B. T. Thole, M. Altarelli, and X. Wang, Physical Review Letters **70**, 694 (1993), ISSN 0031-9007.

[5] B. T. Thole, P. Carra, F. Sette, and G. van der Laan, Physical Review Letters **68**, 1943 (1992).

[6] F. Wilhelm, J. P. Sanchez, J.-P. Brison, D. Aoki, A. B. Shick, and A. Rogalev, Physical Review B **95**, 235147 (2017).

[7] G. van der Laan, Physical Review B **57**, 5250 (1998), ISSN 0163-1829, 1095-3795.

[8] A. Stupakiewicz, A. Chizhik, M. Tekielak, A. Zhukov, J. González, and A. Maziewski, The Review of scientific instruments **85**, 103702 (2014).

[9] L. Onsager, Physical Review **37**, 405 (1931).

[10] K. Sato and T. Ishibashi, Frontiers in Physics **10** (2022), ISSN 2296-424X.

[11] E. B. Aleksandrov and V. S. Zapasskiy, *Laser Magnetic Spectroscopy* (NAUKA, 1986).

[12] S.-K. Kim, Journal of Physics D: Applied Physics **43**, 264004 (2010), ISSN 0022-3727.

[13] R. T. Merrill, M. W. McElhinny, and P. L. McFadden, *The Magnetic Field of the Earth: Paleomagnetism, the Core, and the Deep Mantle* (Academic Press, 1998), ISBN 978-0-12-491246-5.

[14] A. Kirilyuk, A. V. Kimel, and T. Rasing, Reviews of Modern Physics **82**, 2731 (2010).

[15] G. P. Zhang, W. Hübner, G. Lefkidis, Y. Bai, and T. F. George, Nature Physics **5**, 499 (2009), ISSN 1745-2481.

Chapter 3

Spin dynamics driven by ultrafast laser-induced heating of iron garnet in high magnetic fields

Femtosecond laser excitation heats a ferrimagnetic iron garnet across the compensation temperature and decreases the magnetizations of the constituting Fe^{3+} sublattices. Here we explore the heat-induced magnetization dynamics in the ferrimagnet at different points in the $H - T$ phase diagram. For magnetic field strengths high enough to promote a state with non-collinear magnetizations of the sublattices, the dynamics occurs on a sub-ns time-scale, governed by the effective spin-lattice interaction throughout the whole Brillouin zone of the spin excitations. When the field is low and the magnetizations are collinear, the heating alone is not sufficient to initiate the dynamics. In that case, the dynamics can only start after the magnetizations experience an initial kick, which occurs on the time-scale of the spin-lattice interaction in the center of the Brillouin zone, leading to a substantial delay of the response of the spins to the thermal excitation. [1]

[1]Part of this work has been adapted from: I. A. Dolgikh, F. Formisano, K. H. Prabhakara, M. V. Logunov, A. K. Zvezdin, P. C. M. Christianen, and A. V. Kimel *Applied Physics Letters*, 120(1):012401, 2022

3.1 Introduction

As the essence of magnetization is angular momentum, heavy debates about the interplay between a crystal lattice and electron spins have always been at the core of ultrafast magnetism [1–5]. Ferrimagnets are very appealing materials for both fundamental studies of ultrafast magnetism as well as for future ultrafast magnetic data storage [5–7] and exhibit some of the most spectacular examples of ultrafast magnetism [8, 9]. Their magnetic structure can be changed substantially by changing temperature T and/or an applied magnetic field H. Hence, the $H-T$ phase diagram of ferrimagnets represents a rich playground to explore how the magnetization dynamics, driven by the spin-lattice interaction, changes upon changing the magnetic structure.

Iron garnet is a particularly appealing ferrimagnet because the time constant of the spin-lattice interactions varies over six orders of magnitude from $\sim$ 1 μs [10] to $\sim$ 250 ps [11, 12] and down to $\sim$ 1 ps [3, 13]. It is, therefore, an interesting question how the magnetic structure of the iron garnet can affect the magnetization dynamics driven by the spin-lattice interaction.

Here we explore the heat-induced magnetization dynamics in a ferrimagnetic iron garnet at different points in the $H-T$ phase diagram at fields up to 30 T. We show that for the high field state, with non-collinear magnetizations of the sublattices, the magnetization dynamics occurs on a sub-ns timescale. In this case, the heat transfer from the phonons to the spins, determined by the spin-lattice interaction throughout the whole Brillouin zone, decreases the length of the magnetizations and triggers their rotation. In contrast, at low magnetic fields, when the magnetizations are collinear, the heat-induced dynamics is substantially slower (>>1 ns). The rotation of the magnetizations can only start after an initial kick which occurs on the time-scale of the spin-lattice interaction in the center of the Brillouin zone.

3.2 Experimental details

3.2.1 Sample characterization

The sample chosen for our study is a ferrimagnetic insulator from the family of iron garnets - $(Lu_{2.2}Bi_{0.8})(Fe_{3.2}Ga_{1.0}Al_{0.8})O_{12}$. It is an 8 μm thick film, grown on a (111) gadolinium gallium garnet substrate using liquid-phase epitaxy. Although an iron garnet single crystal has a cubic magnetic anisotropy, thin films normally exhibit a uniaxial anisotropy during growth, with the easy-axis along the sample normal [14]. The Lu^{3+} ion has no magnetic moment. The Fe^{3+} ions with spin $S = 5/2$ occupy the tetrahedral and octahedral sites. The spins of ions in a similar environment couple

ferromagnetically, while the coupling between the spins of the octahedral and tetrahedral Fe^{3+} ions is antiferromagnetic.

In the parent compound $Lu_3Fe_5O_{12}$ below the Curie temperature ($T_C \sim$ 500 K), the net magnetization is dominated by the tetrahedral sublattice [15]. Substituting the Fe^{3+} ions in the tetrahedral positions with Ga^{3+} and Al^{3+} equilibrates the magnetizations of the sublattices at the so-called compensation temperature T_M [14]. The value of this temperature is defined by the doping and can vary in a broad range [16]. In particular, the sample studied here has $T_M = 50$ K, which was also confirmed by our measurements of the Faraday rotation. Thus, we obtained a two sublattice ferrimagnet without rare-earth magnetic ions and with a compensation point [17–19]. To enhance the magneto-optical effects, a part of the Lu^{3+} ions was substituted by Bi^{3+} [20].

3.2.2 Magnetic order of LuIG in the vicinity of the compensation temperature

Prior to the pump-probe experiments, we characterized the sample in fields up to 32 T using the static magneto-optical Faraday effect. Figure 3.1 shows that the sample causes a strong polarization rotation even at low magnetic fields $H << 1$ T. This behaviour evidences that the sample has a uniaxial magnetic anisotropy, with the easy axis along the sample normal, as well as a low coercive field. The loops reverse their sign around 50 K. As magneto-optical effects in iron garnets are dominated by the magnetization of the Fe^{3+} ions in the octahedral sublattice [21] and the equilibrium orientation of the net magnetization is parallel to the applied magnetic field, the flip of the hysteresis loop is a signature of crossing the compensation point T_M. An increase of the magnetic field above the threshold value $H_{SF} \sim \sqrt{(H_{an}H_{ex})}$ (H_{an} is the effective field of the uniaxial magnetic anisotropy and H_{ex} is the effective field of the inter-sublattice exchange interaction) leads to a spin-flop transition – the magnetizations of the two sublattices rotate over 90 degrees and get canted forming a non-collinear phase [22]. Due to the predominant sensitivity of magneto-optical effects to the spins of Fe^{3+} ions at the octahedral sites and the sensitivity of the Faraday effect, in particular, to the spins normal to the sample plane, the spin flop transition is seen in our measurements as a substantial reduction of the magneto-optical signal upon an increase of the field. In all measured hysteresis loops, one can distinguish such a decrease starting around 4 T. In particular, an increase of the field results in a gradual change of the magneto-optical signal. This behaviour usually corresponds to a second-order spin-flop phase transition [23]. Additionally, at fields much lower than 1 T and close to the compensation temperature, one can also distinguish an abrupt decrease of the signal. These low field features can originate from other phases stabilized either due to the interplay of uniaxial and

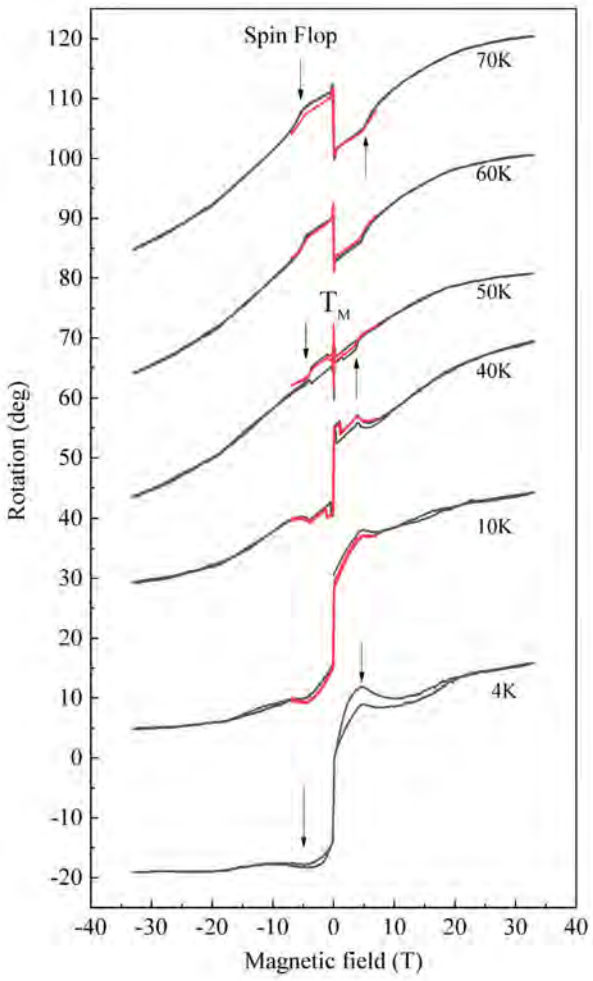

Figure 3.1: Double passage Faraday effect and the corresponding hysteresis loops in magnetic fields up to 32 T. The measurements were taken upon an increase of temperature. A reversal of the hysteresis loop occurs at the magnetization compensation temperature (T_M = 50 K). Arrows indicate the spin-flop fields. The red curves are measured up to 7 T using another experimental setup.

cubic magnetic anisotropies or simply due to inhomogeneities of the sample. The origin of these low field phases and their ultrafast laser-induced spin dynamics is beyond the scope of this work.

3.2.3 Ultrafast heating experiment

For the measurement of the ultrafast laser-induced magnetization dynamics, we employed an optical pump-probe technique combined with a DC magnet, capable of generating fields up to 37.5 T [24, 25].

Laser pulses with a duration of 100 fs were generated at a frequency of 1 kHz with a central photon energy of 1.5 eV. For this photon energy, the absorption coefficient of the studied iron garnet is relatively small ($\alpha = 280$ cm^{-1}). Part of the laser beam was used as a probe in our pump-probe experiment. The other part was used to generate 100 fs pulses with a central photon energy of 2.3 eV using a parametric amplifier. At this photon energy, the absorption coefficient of the sample is substantial ($\alpha = 2012$ cm^{-1}) and hence this beam was used as a pump. Both beams were spatially overlapped and focused on the sample into spots of approximately 50 μm in diameter. The fluence of the pump pulses was 25 mJ/cm^2, which is at least six times larger than the fluence of the probe pulses. The energies deposited by the pump and probe pulses into the medium are 0.4 μJ and 16 nJ, respectively. To be sensitive to the magnetization dynamics caused by the pump, we measured the polarization rotation of the probe beam due to the magneto-optical Faraday effect in a double-passage geometry. In particular, the polarization of the light reflected from the bottom surface of the sample was measured using a two-photodiode balanced detector. The corresponding rotation of the polarization measures the magnetization component normal to the sample. Lock-in detection allowed us to boost the sensitivity of our measurements (Chapter 2).

3.3 Magnetization dynamics in LuIG

Figure 3.2 shows time-resolved transients of the double Faraday effect after the sample was excited by the 100 fs laser pump. The measurements are performed at different temperatures, below and above T_M, in magnetic fields up to 30 T. Each of the measured dependencies is characterized by a rapid increase of the magneto-optical signal at a ps time-scale followed by a slower increase of the signal at a ns time-scale. Each of the transients was fitted with a sum of two exponential functions:

$$\Delta\theta(t) = A_1(e^{-t/\tau_1} - 1) + A_2(e^{-t/\tau_2} - 1) \tag{3.1}$$

where A_1 and A_2 are the amplitudes and τ_1 and τ_2 are the characteristic times of the sub-ps and ns dynamics, respectively. First, fitting only the dynamics faster than 10 ps we found that neither the amplitude A_1 nor

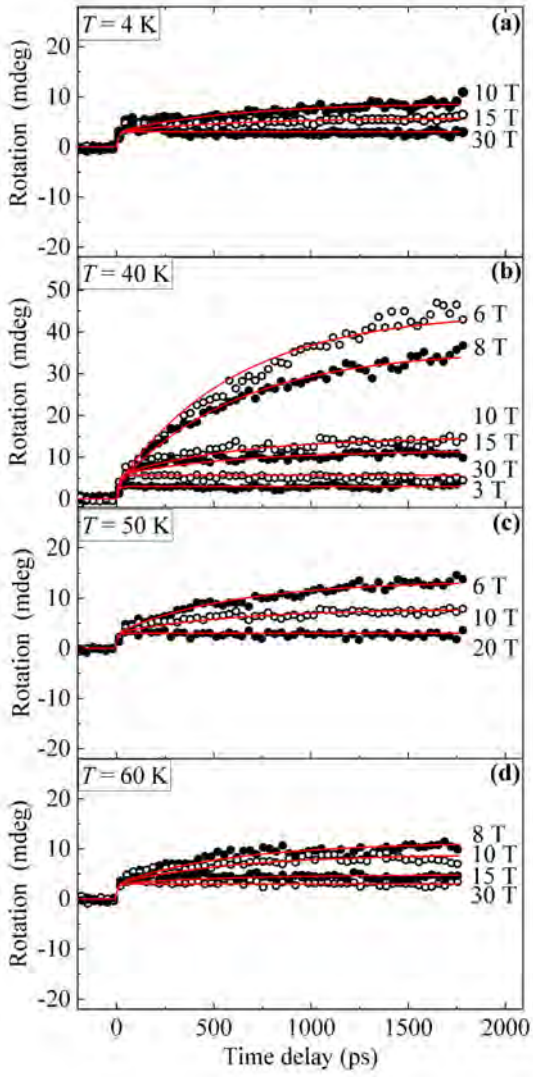

Figure 3.2: Laser-induced dynamics (symbols) of the double passage Faraday effect in external magnetic fields at (a) $T = 4$ K, $T << T_{\mathrm{M}}$; (b) $T = 40$ K, $T < T_{\mathrm{M}}$; (c) $T = 50$ K, $T \approx T_{\mathrm{M}}$; (d) $T = 60$ K, $T > T_{\mathrm{M}}$. Red lines correspond to the fits with the function given by Eq. 3.1. All the data can be fitted with $A_1 = 3$ mdeg, $\tau_1 = 1$ ps, $\tau_2 = 600$ ps having A_2 as the only free parameter.

the characteristic time τ_1 depend on the applied magnetic field strength or the temperature. Therefore, in contrast to the results reported in Ref. [3], this fast response cannot be assigned to the magnetization dynamics. Since the amplitude corresponds to just 0.05% of the total magneto-optical signal, this picosecond dynamics can simply be due to an artifact from a laser-induced transmissivity change and a dynamical recalibration of the detection scheme [26]. The term with the amplitude A_2 corresponds to the magneto-optical signal due to the magnetization dynamics. In principle, heat can trigger in the ferrimagnet both the longitudinal and transversal magnetization dynamics corresponding to a decrease of the magnetizations in size and their uniform rotation, respectively.

Keeping A_1 and τ_1 fixed and fitting the sub-nano and nano-second dynamics, we find that the characteristic time $\tau_2 \sim 1$ ns hardly changes with temperature or applied field strength and stays nearly constant throughout all experiments. This value of τ_2 is in good agreement with the characteristic time of the spin-lattice interaction in iron-garnets reported earlier and corresponds to the timescale at which the heat transfer between the lattice and the spins takes place [27]. Hence, it is reasonable to assign the nanosecond dynamics to be due to femtosecond laser-induced heating of the lattice, followed by equilibration of the lattice and spin temperatures on a time-scale of the spin-lattice interaction. If one assumes that the nanosecond dynamics is due to heating and analyzes the traces obtained above 5 T, a comparison of the amplitude A_2 of the laser-induced spin dynamics with the values of the static Faraday effect (see Fig. 1) suggests that a single laser pulse increases the spin temperature by about $\Delta T = 10 - 20$ K. Estimates of the laser-induced heating can also be obtained taking into account the pump fluence ($F = 25$ mJ/cm^2), the size of the pump beam ($S = 2 \times 10^{-5}$ cm^2), the thickness of the sample ($d = 8$ μm) and the specific heat capacity ($C_{\mathrm{M}} = 83$ $\frac{J}{\mathrm{mole}\times K}$ [28]). Neglecting the reflection of light from the sample, one finds that the estimated maximum temperature change is $\Delta T = F(1 - e^{-\alpha d})\frac{S}{\rho V C_{\mathrm{M}}} = 86$ K. Note that this estimation does not take into account the heat transfer in the sample from the laser-excited area. The amplitudes A_2 of the ns-dynamics are summarized in the inset of Fig. 3.3 and appear to be extremely sensitive to the external magnetic field and temperature. In particular, it has a clear singularity around 4 T and the observed dependencies of A_2 are in good agreement with the theoretically predicted amplitude of the laser-induced dynamics for the case of a ferrimagnet heated across the compensation temperature [29]. Hence, this agreement together with the estimates of ΔT allows us to conclude that the femtosecond laser pulse increases the sample temperature by at least 10 K and at $T = 40$ K heats the sample across the compensation temperature.

Figure 3.3 summarizes the main findings of our work. We have identified the fields of the spin-flop transition and found different magnetic phases in

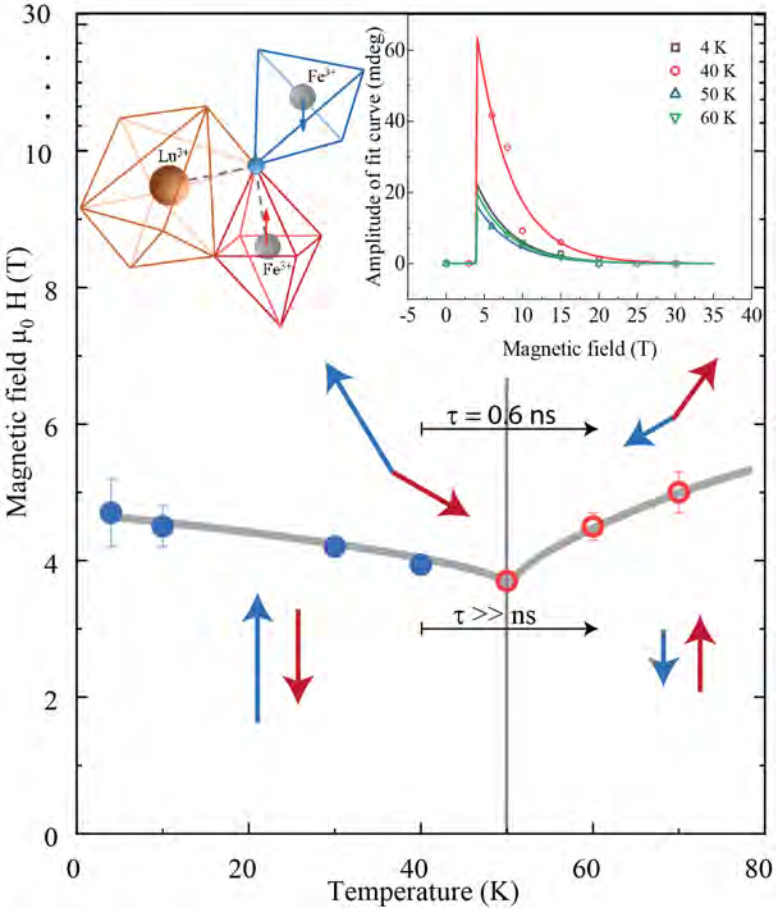

Figure 3.3: $H-T$ phase diagram of $(Lu_{2.2}Bi_{0.8})(Fe_{3.2}Ga_{1.0}Al_{0.8})O_{12}$. The values of the spin-flop field are determined from the field dependencies shown in Fig. 3.1. The blue and red arrows correspond to the tetrahedral and octahedral sublattices, respectively (see the inset in the left corner). Femtosecond laser pulses heat the iron garnet leading to a temperature increase of about 10 K (see horizontal arrows). Starting at $T = 40$ K, the heating brings the ferrimagnet across the compensation temperature and causes a reorientation of the magnetization of the sublattices. In the non-collinear and collinear phases, the reorientation takes substantially different times. Inset in the upper right corner shows the magnetic field dependence of the amplitude A_2 obtained from the fit of the magneto-optical transients in Fig. 3.2, using a double exponential decay (Eq. 3.1) and keeping other parameters fixed ($A_1 = 3$ mdeg, $\tau_1 = 1$ ps, $\tau_2 = 600$ ps). The solid lines are guides to the eye.

the $H - T$ phase diagram of $(Lu_{2.2}Bi_{0.8})(Fe_{3.2}Ga_{1.0}Al_{0.8})O_{12}$ iron garnet.

Femtosecond heating of the lattice brings the lattice out of equilibrium with the spin system (illustrated by the arrows in Fig. 3.3) and launches magnetization dynamics driven by the spin-lattice relaxation. By varying H and T we explored the magnetization dynamics in different points of the $H - T$ phase diagram. Our results reveal substantially different heat-induced magnetization dynamics below and above the spin flop field. For instance, at $T = 40$ K and $H = 6$ T, i.e. in the non-collinear phase, the heat-induced magnetization dynamics is rather pronounced and relatively slow.

3.4 Discussion

The time trace obtained upon heating the medium from the collinear phase across the compensation temperature (at $T = 40$ K and $H = 3$ T) is very different and represents the most counter-intuitive result. In this case, the heating reduces the magnetizations of the sublattices on a time-scale of the spin-lattice interaction. As the amplitude of the magnetization, in general, depends on the temperature of all spin waves, the sublattices reduce their magnetizations on the time-scale of effective spin-lattice interaction for spin-wave excitations throughout the whole Brillouin zone (0.6 ns). Increasing the temperature above T_M dramatically changes the ratio between the magnetizations of the sublattices. In particular, the magnetization of the octahedral sublattice starts to dominate and it means that the net magnetization is antiparallel with respect to the applied magnetic field. This state is energetically unfavorable. In order to reach the state of thermodynamic equilibrium, the magnetizations of the sublattices must be reversed. Remarkably, in contrast to intuitive expectations, we do not observe any dynamics up to 2 ns. In order to initiate the dynamics towards thermodynamic equilibrium, the magnetization of a given sublattice $\vec{M}$ must experience an initial kick so that $\vec{M} \times \vec{H} \neq 0$. In the non-collinear case, this inequality is always the case and the magnetization dynamics starts as soon as the magnetization is brought out of thermodynamic equilibrium. In the collinear phase, however, even if the magnetic field is pointing antiparallel with respect to the magnetization, $\vec{M} \times \vec{H} = 0$ and the magnetization dynamics cannot start. The dynamics can start only if due to fluctuations the magnetization is slightly tilted. This can only occur due to the spin-lattice interaction. However, in the case of homogeneous rotation of the magnetization of the whole sample, the corresponding excitation must have a zero wave-vector. Consequently, in this case, the spin-lattice interaction involves spin waves in the center of the Brillouin zone. This process occurs on a timescale much longer than 1 ns, certainly longer than the spin-lattice interaction for spin waves throughout the whole Brillouin zone. A similar mismatch in spin-lattice relaxation times deduced from

different experiments was also discussed in Ref. [26].

3.5 Summary

In conclusion, we have used femtosecond laser pulses to heat a ferrimagnetic iron garnet and increase the spin temperature on a timescale of 1 ns. The induced heating results in demagnetization of the antiferromagnetically coupled sublattices and causes a reorientation of their magnetizations in an external magnetic field. The amplitude of this reorientation is the largest just above the spin-flop field, where the magnetizations of the sublattices are in a non-collinear state. For small magnetic fields, below the spin-flop threshold, the nanosecond heating of the ferrimagnet across the compensation temperature brings the medium into a state with mutually antiparallel orientations of the applied field and net magnetization. The heating, however, is insufficient to launch the magnetization dynamics within the first 2 ns even if the applied field is as strong as 3 T.

Bibliography

[1] C. Dornes, Y. Acremann, M. Savoini, M. Kubli, M. J. Neugebauer, E. Abreu, L. Huber, G. Lantz, C. A. F. Vaz, H. Lemke, et al., Nature **565**, 209 (2019), ISSN 0028-0836, 1476-4687.

[2] B. Koopmans, J. J. M. Ruigrok, F. D. Longa, and W. J. M. de Jonge, Physical Review Letters **95**, 267207 (2005), ISSN 0031-9007, 1079-7114.

[3] S. F. Maehrlein, I. Radu, P. Maldonado, A. Paarmann, M. Gensch, A. M. Kalashnikova, R. V. Pisarev, M. Wolf, P. M. Oppeneer, J. Barker, et al., Science Advances **4**, eaar5164 (2018), ISSN 2375-2548.

[4] C. Stamm, T. Kachel, N. Pontius, R. Mitzner, T. Quast, K. Holldack, S. Khan, C. Lupulescu, E. F. Aziz, M. Wietstruk, et al., Nature Materials **6**, 740 (2007), ISSN 1476-4660.

[5] N. Thielemann-Kühn, D. Schick, N. Pontius, C. Trabant, R. Mitzner, K. Holldack, H. Zabel, A. Föhlisch, and C. Schüßler-Langeheine, Physical Review Letters **119**, 197202 (2017), ISSN 0031-9007, 1079-7114.

[6] K. Cai, Z. Zhu, J. M. Lee, R. Mishra, L. Ren, S. D. Pollard, P. He, G. Liang, K. L. Teo, and H. Yang, Nature Electronics **3**, 37 (2020), ISSN 2520-1131.

[7] C. S. Davies, K. H. Prabhakara, M. D. Davydova, K. A. Zvezdin, T. B. Shapaeva, S. Wang, A. K. Zvezdin, A. Kirilyuk, Th. Rasing, and A. V.

Kimel, Physical Review Letters **122**, 027202 (2019), ISSN 0031-9007, 1079-7114.

[8] C. D. Stanciu, A. Tsukamoto, A. V. Kimel, F. Hansteen, A. Kirilyuk, A. Itoh, and Th. Rasing, Physical Review Letters **99**, 217204 (2007), ISSN 0031-9007, 1079-7114.

[9] I. Radu, K. Vahaplar, C. Stamm, T. Kachel, N. Pontius, H. A. Dürr, T. A. Ostler, J. Barker, R. F. L. Evans, R. W. Chantrell, et al., Nature **472**, 205 (2011), ISSN 1476-4687.

[10] J. Xiao, G. E. W. Bauer, K.-c. Uchida, E. Saitoh, and S. Maekawa, Physical Review B **81**, 214418 (2010), ISSN 1098-0121, 1550-235X.

[11] M. Schreier, A. Kamra, M. Weiler, J. Xiao, G. E. W. Bauer, R. Gross, and S. T. B. Goennenwein, Physical Review B **88**, 094410 (2013), ISSN 1098-0121, 1550-235X.

[12] L. J. Cornelissen, K. J. H. Peters, G. E. W. Bauer, R. A. Duine, and B. J. van Wees, Physical Review B **94**, 014412 (2016), ISSN 2469-9950, 2469-9969.

[13] S. M. Rezende, R. L. Rodríguez-Suárez, R. O. Cunha, J. C. López Ortiz, and A. Azevedo, Journal of Magnetism and Magnetic Materials **400**, 171 (2016), ISSN 0304-8853.

[14] Yu. B. Kudasov, M. V. Logunov, R. V. Kozabaranov, I. V. Makarov, V. V. Platonov, O. M. Surdin, D. A. Maslov, A. S. Korshunov, E. Ya. Popov, and A. S. Svetlov, Physics of the Solid State **60**, 2207 (2018), ISSN 1063-7834, 1090-6460.

[15] C. D. Brandle and S. L. Blank, IEEE Transactions on Magnetics **12**, 14 (1976), ISSN 0018-9464, 1941-0069.

[16] P. Hansen, P. Röschmann, and W. Tolksdorf, Journal of Applied Physics **45**, 2728 (1974), ISSN 0021-8979, 1089-7550.

[17] M. Deb, P. Molho, B. Barbara, and J.-Y. Bigot, Physical Review B **97**, 134419 (2018), ISSN 2469-9950, 2469-9969.

[18] R. Radwański, Physica B+C **142**, 57 (1986), ISSN 03784363.

[19] M. Binder, A. Weber, O. Mosendz, G. Woltersdorf, M. Izquierdo, I. Neudecker, J. R. Dahn, T. D. Hatchard, J.-U. Thiele, C. H. Back, et al., Physical Review B **74**, 134404 (2006), ISSN 1098-0121, 1550-235X.

[20] C. F. Buhrer, Journal of Applied Physics **40**, 4500 (1969), ISSN 0021-8979, 1089-7550.

[21] A. K. Zvezdin and V. A. Kotov, *Modern Magnetooptics and Magnetooptical Materials* (CRC Press, 1997), ISBN 978-1-4200-5084-4.

[22] A. K. Zvezdin, in *Handbook of Magnetic Materials* (Elsevier, 1995), vol. 9, pp. 405–543.

[23] A. K. Zvezdin, M. D. Davydova, and K. A. Zvezdin, Physics-Uspekhi **61**, 1127 (2019).

[24] J. Becker, A. Tsukamoto, A. Kirilyuk, J. C. Maan, Th. Rasing, P. C. M. Christianen, and A. V. Kimel, Physical Review Letters **118**, 117203 (2017), ISSN 0031-9007, 1079-7114.

[25] A. Pogrebna, K. Prabhakara, M. Davydova, J. Becker, A. Tsukamoto, Th. Rasing, A. Kirilyuk, A. K. Zvezdin, P. C. M. Christianen, and A. Kimel, Physical Review B **100**, 174427 (2019), ISSN 2469-9950, 2469-9969.

[26] A. V. Kimel, R. V. Pisarev, J. Hohlfeld, and Th. Rasing, Physical Review Letters **89**, 287401 (2002), ISSN 0031-9007, 1079-7114.

[27] F. Hansteen, A. Kimel, A. Kirilyuk, and T. Rasing, Physical Review B **73**, 014421 (2006), ISSN 1098-0121, 1550-235X.

[28] A. B. Harris and H. Meyer, Physical Review **127**, 101 (1962), ISSN 0031-899X.

[29] M. D. Davydova, K. A. Zvezdin, A. V. Kimel, and A. K. Zvezdin, Journal of Physics: Condensed Matter **32**, 01LT01 (2020), ISSN 0953-8984, 1361-648X.

Chapter 4

Magneto-structural transition in FeRh

Ultrafast heating of FeRh by a femtosecond laser pulse launches a magneto-structural phase transition from an antiferromagnetic to a ferromagnetic state. Aiming to reveal the ultrafast kinetics of this transition, we studied magnetization dynamics with the help of the magneto-optical Kerr effect in a broad range of temperatures (from 4 K to 400 K) and magnetic fields (up to 25 T). Three different types of ultrafast magnetization dynamics were observed and, using a numerically calculated $H-T$ phase diagram, the differences were explained by different initial states of FeRh corresponding to a (i) collinear antiferromagnetic, (ii) canted antiferromagnetic and (iii) ferromagnetic alignment of spins. We argue that ultrafast heating of FeRh in the canted antiferromagnetic phase launches practically the fastest possible emergence of magnetization in this material. The magnetization emerges on a timescale of 3 ps, corresponding to the earlier reported timescale of the structural changes during the phase transition. [1]

[1]Part of this work has been adapted from: I. A. Dolgikh, T. G. H. Blank, A. G. Buzdakov, G. Li, K. H. Prabhakara, S. K. K. Patel, R. Medapalli, E. E. Fullerton, O. V. Koplak, J. H. Mentink, K. A. Zvezdin, A. K. Zvezdin, P. C. M. Christianen, and A. V. Kimel *arXiv preprint:2202.03931 (2022)* and from: A. G. Buzdakov, I. A. Dolgikh, K. A. Zvezdin, A. K. Zvezdin, K. Rubi, U. Zeitler, P. C. M. Christianen, T. Rasing, S. K. K. Patel, R. Medapalli, E. E. Fullerton, E. T. Dilmieva, and A. V. Kimel *Physical Review B 108.18 (2023): 184420*

4.1 Introduction

The metallic alloy FeRh stands out due to the counter-intuitive heat-induced ferromagnetism first reported in 1938 [1]. The material is antiferromagnetic at low temperatures and becomes ferromagnetic when heated above 370 K. The magnetic changes are accompanied by an expansion of the unit cell of FeRh. The nature of this heat-induced ferromagnetism in FeRh has been a subject of debates for about 60 years. The dispute of whether it is the change in the magnetic order that drives the lattice expansion or vice versa very much resembles the chicken-or-egg causality dilemma [2–6]. The very first hypothesis explaining the mechanism of the emerging ferromagnetism stated that the structural change leads to a sign change of the exchange integral and thus initiates changes of the order of the Fe-spins from antiferromagnetic to ferromagnetic [7]. However, very soon thereafter it was argued that this mechanism is inconsistent with the actual change of the lattice entropy. The latter, estimated from experimental data, appeared to be much less than the total entropy change [8]. Several computational studies proposed that the magneto-structural phase transition is entirely driven by processes in the spin system [9–13]. At the same time, one cannot ignore that according to recent calculations the changes in the lattice entropy and the total entropy during the phase transition in FeRh differ just by a factor of 3 [14] or are even comparable [3]. Several attempts have been done to detect the ultrafast kinetics during the phase transition using a femtosecond laser pulse as an ultrafast heater and tracing the laser-induced dynamics of the lattice and spins. However, even after these experiments, the dispute is far from being resolved. Refs. [15–17] claim that the changes in the spin system are faster than those in the lattice, while others [18–20] state that the lattice expands much earlier than the net magnetization emerges. In Ref. [21] it was even found that the electronic band structure changes on a subpicosecond timescale during laser-induced phase transition far before lattice or spins. Hence, the sequence and the actual mechanism of the magnetic and structural dynamics in the magneto-structural phase transition of FeRh remain unclear. Lacking efficient means to control the speed of the dynamics of the lattice or spins, this question has become a classical chicken-or-egg causality dilemma. In addition to these fundamental obstacles, in practice, the studies of FeRh are hampered by the co-existence of the low-temperature antiferromagnetic and the high-temperature ferromagnetic phases [22–24]. Although such a co-existence is very typical for first-order phase transitions, as in FeRh, it often leads to difficulties in interpreting the experimental data as discussed in Ref. [25]. Here we aim to understand the ultrafast magnetization dynamics during the magneto-structural phase transition in FeRh by performing time-resolved magneto-optical pump-probe measurements in an unprecedently broad range of temperatures (from 4 K to 400 K) and magnetic field strengths (from 0.125 T to 25 T). Increasing the magnetic field

up to 25 T is an efficient means to control the speed of the magnetization dynamics in FeRh, while decreasing the temperature down to 4 K affects the volume ratio of the co-existing ferro- and antiferromagnetic phases. In this chapter, we investigate the *H-T* phase diagram of FeRh by combining a numerical approach with static measurements of magnetic and magneto-optical properties. We also present the results of time-resolved magneto-optical measurements of the ultrafast magnetization dynamics in FeRh. Specifically, we demonstrate that the applied magnetic field can accelerate the emergence of the ferromagnetic phase, but only up to a certain limit, when the characteristic time is close to the timescale of the accompanying structural changes. Moreover, we observe that depending on the temperature and applied magnetic field, a femtosecond laser pulse can trigger three different types of ultrafast magnetization dynamics in FeRh, which correspond to different initial states of the spin order, namely collinear antiferromagnetic, canted antiferromagnetic, and ferromagnetic phases. These findings are supported by simulations showing that the observed changes in the magnetization dynamics are intrinsic to the simplistic two-spin model and are therefore a general feature of all antiferromagnets, not only FeRh. Additionally, we report on time-resolved measurements of the reflectivity, which provides insights into the dynamics of the structural changes in FeRh. This section further supports the hypothesis that the magnetic and structural changes during the phase transition occur simultaneously and in step with each other.

4.2 Sample

FeRh is a metallic compound with a CsCl crystal structure and a tetragonal magnetic unit cell. At low temperatures, in the absence of any external fields and at ambient pressure, the spins of the Fe atoms are aligned antiferromagnetically and have a net magnetic moment $m_{\mathrm{Fe}} \approx 3\ \mu_{\mathrm{B}}$ per atom, while the Rh atoms have no magnetic moment [26]. When increasing the temperature to around 370 K, a phase transition is triggered from the antiferromagnetic (AFM) to the ferromagnetic (FM) state. The parallel aligned magnetic moments of iron remain at $m_{\mathrm{Fe}} \approx 3\ \mu_{\mathrm{B}}$ per atom, while the Rh ions acquire an atomic magnetic moment of $m_{\mathrm{Rh}} \approx 1\ \mu_{\mathrm{B}}$ (see Fig. 4.1(b)) [27, 28].

These magnetic changes are accompanied by an expansion of the unit cell of about 1% [29], preserving the CsCl crystal structure [30]. The studied sample was a 40 nm thick, epitaxial $Fe_{50}Rh_{50}$ film deposited onto a MgO(001) single crystal substrate and then capped with a 5 nm thick Pt layer. The total volume of the FeRh(001) layer was estimated to be $2.9{\times}10^{-7}$ cm^3. More details on the structural characterization such as X-ray reflectometry, X-ray diffraction, and manufacturing procedure of the studied film are reported in Ref. [31]. Unlike bulk samples, thin films of

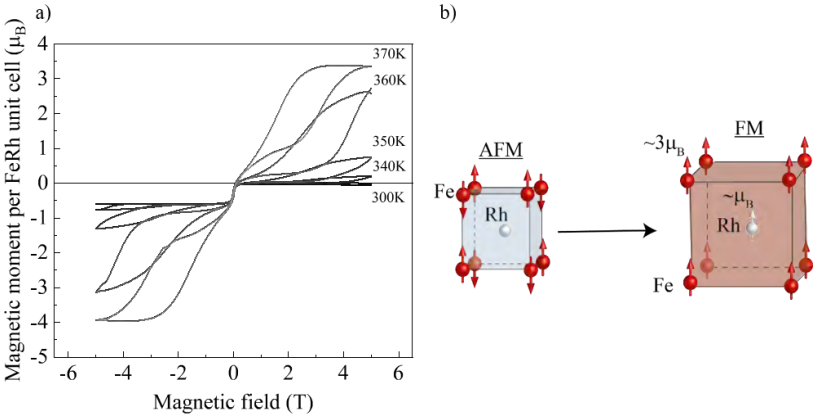

Figure 4.1: (a) Magnetization as a function of a magnetic field applied along the normal to the sample. Data was obtained using SQUID magnetometry of a FeRh thin film for temperatures from 300 K to 370 K. (b) Unit cell of FeRh with the schematics showing the changes during the magneto-structural phase transition from an anti-ferromagnetic (AFM) to a ferromagnetic (FM) state, accompanied by an expansion of the lattice.

FeRh may expand differently along different crystallographic axes [32].

4.3 $H - T$ phase diagram of FeRh

4.3.1 Magnetic characterization

It is known that applying an external magnetic field shifts the critical temperature at which the magneto-structural phase transition in FeRh occurs [9]. Figure 4.1 shows the magnetization curves of the studied FeRh sample. An external magnetic field was applied along the sample normal. The magnetic moment at different temperatures was recorded by a Quantum Design SQUID magnetometer in the reciprocal-sample-option (RSO) mode. The SQUID device measures the net magnetization of the whole sample. The data shown in the figure reveals a clear jump in the net magnetization at relatively low magnetic fields (below 1 T). This jump does not depend on the sample temperature and is usually attributed to the magnetic response of the first few FeRh layers at the interface with the MgO substrate. Due to the strain induced by the substrate, these layers cannot accommodate any volume change across the phase transition and remain in the FM phase also at lower temperatures. An applied magnetic field saturates the magnetization of these FM layers [32].

The SQUID data also shows that magnetic fields above 1 T can induce a significantly larger magnetization. The up- and down sweeps of the field

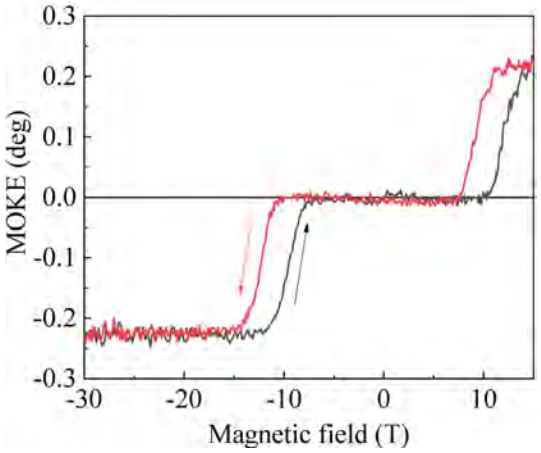

Figure 4.2: Polar magneto-optical Kerr effect (MOKE) in external magnetic fields up to 30 T. The polarization rotation is due to a magneto-optical Kerr effect measured at normal incidence at 300 K. Arrows indicate the direction of the magnetic field sweep.

reveals a hysteresis, which is associated with a field-induced first-order phase transition from an antiferromagnetic (AFM) to a ferromagnetic (FM) state. For fields up to 5 T, the phase transition is clearly seen in the range from 350 K to 370 K. At the same time, for temperatures below 370 K, 5 T it is not sufficient to saturate the magnetization of the sample. It means that even at 5 T and below 370 K the FM and AFM phases can co-exist.

The magnetic moment M measured in emu was recalibrated to the magnetic moment per unit cell μ in the units of the Bohr magneton μ_{B}, using $\mu = \frac{M[\mathrm{emu}]m_{\mathrm{mol}}[\mathrm{g/mole}]}{\mu_{\mathrm{B}}N_{\mathrm{A}}m[\mathrm{g}]}$, where N_{A} is Avogadro's number, m_{mol} is the molar mass and m is the mass of the FeRh film.

At 370 K and 3 T, the signal reaches saturation, meaning that the magnetization of the FeRh film is fully aligned by the external field along the normal to the sample, at a value close to the expected maximum ~ 4 μ_{B} per unit cell. Hence we assume that at 370 K a field of 3 T is sufficient to align the magnetization along the sample normal in the FM phase.

Figure 4.2 shows the results of static polar magneto-optical Kerr measurements at room temperature. The effect results in a polarization rotation of the reflected light, which is proportional to the normal component of the net magnetization in the sample. Light with a wavelength of 660 nm was used at normal incidence and with a magnetic field applied along the sample normal. The light beam was focused to a spot with a diameter of 50 μm. To extract the contribution of the FeRh film we have subtracted the background line. This line has been fitted to the slope of the MOKE signal after the phase transition is completed. It is seen that at 300 K the

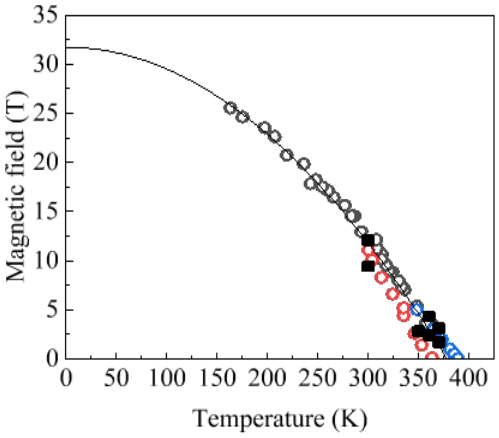

Figure 4.3: Critical magnetic field H_C that triggers the magneto-structural phase transition from the antiferromagnetic to ferromagnetic state in $Fe_{50}Rh_{50}$. The open circles illustrate previously obtained results of the critical magnetic field of the transition for samples of similar composition: black [9], red [30], and blue [33]. The black squares represent the SQUID and MOKE data for our sample as explained in the text. The black solid line describes the fit by the empirical law from [9] $H_C(T) = H_C(0)\left(1 - \left(\frac{T}{T_C}\right)^2\right)$, where $T_C = 378 \pm 2$ K and $H_C(0) = 31.7 \pm 0.6$ T.

magneto-optical signal is not sensitive to the FM phase at the interface with the substrate. The difference between the MOKE and SQUID magnetometry results is due to the fact that the magneto-optical Kerr effect probes the magnetization in a thin surface layer defined by the penetration depth of light which is about 10 nm, whereas the SQUID probes the magnetization in the entire sample. The difference in sensitivities between the polar MOKE and SQUID techniques becomes especially important in the case of thin film samples, where the magnetic properties are expected to be inhomogeneous over the film thickness [32].

Clearly, magnetic fields above 1 T induce a step-like change in the MOKE signal, similar to the SQUID measurements, including the presence of hysteresis, resulting from the magneto-structural first-order AFM-to-FM phase transition. To extract the magnetic fields at which the magneto-structural phase transition takes place, we took the first derivatives of the magnetization curves and deduced the average magnetic field between the fields corresponding to AFM-to-FM and FM-to-AFM transitions. We added these data points to the temperature dependence of the critical field H_C (see Fig. 4.3), obtained from earlier published data measured on FeRh samples with the same or similar compositions [9, 30, 33]. Although the

transition is expected to be accompanied by a temperature hysteresis [34], only one critical temperature has been reported in Refs [9, 30] from pulsed magnetic field experiments up to 28 T. The SQUID magnetometry data from Ref. [33] is included by plotting the averaged value of the two temperatures of the phase transition obtained from the heating and cooling curves. The black solid line represents a fit to all literature data as proposed in Ref. [9] to the expression:

$$H_{\mathrm{C}}(T) = H_{\mathrm{C}}(0)\left(1 - \left(\frac{T}{T_{\mathrm{C}}}\right)^2\right) \tag{4.1}$$

Parameters were found to be T_{C}= 378±2 K and $H_{\mathrm{C}}(0)$= 31.7 ± 0.6 T. Our SQUID magnetometry and MOKE results are consistent with the literature data, so we conclude that our MOKE measurements reliably probe the phase transition from the AFM to the FM state in FeRh.

4.3.2 Theoretical modelling

Even though FeRh H-T phase diagrams such as the one in Fig. 4.3 were discussed several times before [9, 12, 30, 33–41], it is clear that this diagram is not complete. If a magnetic field is applied perpendicular to the antiferromagnetic spins, the field cants spins over an angle defined by the ratio of the applied magnetic field to the effective field of the exchange interaction between the spins [42]. The canting angle increases with increasing the applied field. If the magnetic field is applied parallel to the antiferromagnetically coupled spins, these spins remain insensitive to the field until the so-called spin flop field H_{SF} is reached. In order to estimate H_{SF} for FeRh, in the work [43] we consider the corresponding thermodynamic potential similar to the one used in Ref. [25], but upgraded with terms accounting for magnetic anisotropy and the interaction of spins with the external magnetic field:

$$\begin{aligned} F_{\mathrm{eq}} = &-\left(J^{(2)}_{\mathrm{Fe-Fe}}(T) + \frac{\rho_J^2}{2\epsilon}\right)\left(\vec{M}_1\vec{M}_2\right)^2 - J^{(1)}_{\mathrm{Fe-Fe}}(T)\vec{M}_1\vec{M}_2 - \\ &- \vec{H}_0\left(\vec{M}_1 + \vec{M}_2\right) + K(T)V/2\left(\frac{\left(\vec{M}_1\widehat{\vec{z}}\right)^2}{\vec{M}_1^2} + \frac{\left(\vec{M}_2\widehat{\vec{z}}\right)^2}{\vec{M}_2^2}\right) \end{aligned} \tag{4.2}$$

Here $\vec{M}_1$, $\vec{M}_2$ ($\left|\vec{M}_1\right| = \left|\vec{M}_2\right| = M \approx 1.5\ \mu_{\mathrm{B}}$ per unit cell) are the magnetizations of the two iron sublattices with opposite spin in the AFM phase. In the first term ρ_J is a lattice-dependent exchange constant as proposed in Ref. [7], ϵ is the stiffness constant [7, 30, 44] and $J^{(2)}_{\mathrm{Fe-Fe}}(T)$ is an effective four-spin iron-iron exchange constant as introduced in Refs. [40,

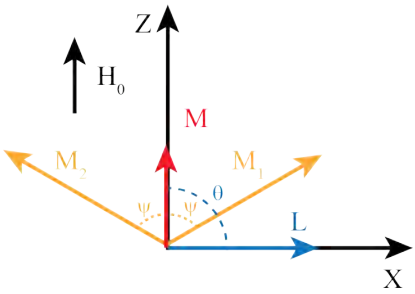

Figure 4.4: Coordinate system used for the calculations of the free energy. Here, ψ - the angle between $\vec{M}_i$ and the magnetization $\vec{M}=(\vec{M}_1+\vec{M}_2)/2$; θ is the angle of the antiferromagnetic vector $\vec{L}=(\vec{M}_1-\vec{M}_2)/2$ with respect to the z-axis. $\vec{H}_0$ denotes the direction of the external magnetic field.

41]. The second term is given by Heisenberg exchange with $J^{(1)}_{\mathrm{Fe-Fe}}(T)$ the temperature-dependent isotropic Heisenberg iron-iron exchange constant. The third term defines the interaction of $\vec{M}_1$ and $\vec{M}_2$ with the magnetic field $\vec{H}_0$ applied along the z-axis (see Fig. 4.4). The last term describes the magnetic anisotropy, where $K(T)$ is the constant of magnetic anisotropy, which is, in principle, temperature dependent. In this case, the anisotropy is defined such that it favours alignment of $\vec{M}_1$ and $\vec{M}_2$ along the z-axis. V is the unit cell volume.

Introducing the angle ψ as defined in Fig.4.4, we describe the orientations of the magnetizations of the Fe sublattices ($\vec{M}_1$ and $\vec{M}_2$) with respect to the magnetization $\vec{M}=(\vec{M}_1+\vec{M}_2)/2$. θ is the angle formed by the antiferromagnetic vector $\vec{L}=(\vec{M}_1-\vec{M}_2)/2$ and the z-axis. In the case of the "easy-axis" of magnetic anisotropy considered here, one gets $KV<0$, antiferromagnetic coupling favored by the two-spin exchange interaction $J^{(1)}_{\mathrm{Fe-Fe}}(T)<0$, and ferromagnetic coupling favored by the second exchange term $J_2=J^2_{\mathrm{Fe-Fe}}+\frac{\rho^2_J}{2\epsilon}>0$.

Minimization of this total free energy with respect to the angles ψ and θ gives the conditions for the equilibrium states. The collinear antiferromagnetic phase corresponds to ($\psi=\pi/2,\ \theta=0$) and the ferromagnetic phase to ($\psi=0, \theta=\pi/2$). In the canted antiferromagnetic phase in an external magnetic field equal to the spin-flop field H_{SF} one can just expect $\psi=\psi_{\mathrm{sf}},\ \theta=\pi/2$, where $\cos\ \psi_{\mathrm{sf}} \ll 1$. The spin flop angle can be found by implying the equilibrium conditions $\frac{\partial F_{\mathrm{sf}}(\psi_{\mathrm{sf}})}{\partial \psi_{\mathrm{sf}}}=0$ and neglecting terms of higher order:

$$\cos\ \psi_{\mathrm{sf}} = \frac{H_{\mathrm{SF}}}{2H_{\mathrm{ex}}-H_{\mathrm{an}}}, \tag{4.3}$$

Comparison of the free energies for canted and collinear antiferromagnetic states gives the spin-flop critical field:

$$H_{\mathrm{SF}} = \sqrt{H_{\mathrm{an}}/2(2H_{\mathrm{ex}} - H_{\mathrm{an}})} \approx \sqrt{H_{\mathrm{an}}H_{\mathrm{ex}}} \tag{4.4}$$

where $H_{\mathrm{ex}} \equiv -J_{\mathrm{eff}}M$, $J_{\mathrm{eff}} = J^1_{\mathrm{Fe-Fe}} - 2\left(J^{(2)}_{\mathrm{Fe-Fe}} + \frac{\rho_J^2}{2\epsilon}\right)M^2$, and the anisotropy field $H_{\mathrm{an}} = -\frac{KV}{M}$.

Using Eq. (4.3) and Eq. (4.4) it is possible to estimate H_{SF} and ψ_{sf} assuming J_{eff} of the order reported in Ref. [11]. From the numerical minimization of the thermodynamic potential given by Eq.(4.2) performed in Ref. [43], we can also analyze the whole H-T phase diagram. We assumed that $J_{\mathrm{eff}}(T)$ is linear with temperature and changes sign at the transition temperature, and the uniaxial anisotropy is out-of-plane.

We note, however, that there is no experimental data on the type and strength of the magnetic anisotropy in the antiferromagnetic phase of FeRh. However, thin magnetic films with zero magnetization, such as ferrimagnets at the compensation temperature, favour out-of-plane magnetic anisotropy due to the absence of demagnetizing fields and a dominant surface anisotropy contribution, resulting from the breaking of the inversion symmetry at the interfaces of the film. Such out-of-plane anisotropy in the AFM phase of FeRh is also predicted by computational studies in Refs. [45, 46]. Hence we assumed that the value for the constant of magnetic anisotropy K is of the order of those proposed in Refs.[46–48]. To further simplify the model, we assume that the magnetic anisotropy is temperature independent.

The actual parameters used in the thermodynamic potential are given by: $J^{(1)}_{\mathrm{Fe-Fe}}M^2 = 0.46 \cdot 10^{-14}(\mathrm{erg})$, $J_2M^4 = 0.23 \cdot 10^{-14}(\mathrm{erg})$, $K = 5 \cdot 10^6$ (erg/cc) and the resulting H-T phase diagram is shown in Figure 4.11a.

We see that the model reproduces all three expected phases: collinear antiferromagnetic (light blue area), canted antiferromagnetic (dark blue area), and ferromagnetic (brown area). The calculated critical fields of the phase transition to the FM state (transition from blue to brown areas) are remarkably close to those obtained in our experiment, although, in our model for most applied fields, this transition to the FM phase starts from the canted AFM phase, rather than from the collinear phase. Only in the low-field region, the model predicts a direct transition from the collinear AFM phase to the FM phase.

We note that the spin-flop transition (from the collinear AFM phase to the canted AFM phase) has not yet been reported for FeRh, but we envisage that its experimental observation must be seriously hampered by the relatively small angle of the spin canting just after the spin-flop $\psi_{\mathrm{sf}} = 5^\circ - 10^\circ$, estimated using our model.

One can argue that there is no real proof of the fact that in our experiment FeRh has a transition between collinear and canted AFM phases. However, at the same time, there is also no experimental proof that the magnetic anisotropy of antiferromagnetic FeRh is in-plane. In this case,

the fields applied in our experiment would tilt the spins even easier, but this canting has also never been reported experimentally (see also Fig. 4.2).

Hence the question about the peculiarities of this phase diagram justifies further experimental studies. To this end, in the following section, we report on our experimental study of the ultrafast magnetization dynamics, the results of which agree with the hypothesis that the AFM phase of FeRh has out-of-plane magnetic anisotropy and that a sufficiently high out-of-plane magnetic field triggers a spin-flop phase transition between the collinear and canted AFM phases.

4.3.3 XMCD characterization

The sample was additionally characterized with X-ray magnetic circular dichroism (XMCD) at the European Synchrotron Facility (ESRF) on beamline ID12 in Grenoble. This beamline is specifically designed for polarization-dependent X-ray absorption studies and utilizes the helical undulator HELIOS II, providing highly polarized X-ray radiation with a polarization rate above 97% and flexible left- and right-handed circular polarization. The first harmonic of the undulator spectrum was tuned to 3146 eV and 3004 eV for the Rh $L_{2,3}$ edges and to 7.1 keV for the Fe K-edge. Two sample configurations were utilized: normal incidence and grazing incidence. The X-ray spot size was around 300 μm in diameter (see Chapter 2 for more information on XMCD experiments).

X-ray absorption near-edge structure (XANES) spectra were measured with circular polarization in a magnetic field applied along the beam direction and the sample normal, using an Oxford instruments superconducting electromagnet. The XMCD spectra were obtained by taking the difference of the XANES spectra recorded with magnetic fields of opposite polarities (fields up and down) corresponding to the opposite circular polarizations, at various fixed temperatures and at magnetic fields up to 17 T using the fluorescent detection mode.

XANES on the Rh $L_{2,3}$ and Fe sites

Firstly, we measured the bare XANES spectra to be able to optimize the spectrum and tune the monochromator to the needed energy for XMCD detection. The spectra were corrected for the incomplete degree of circular polarization. The XMCD was measured at two different temperatures 3 K and 295 K and magnetic fields up to 17 T.

To derive the spin and orbital moments carried by the Rh 4d electrons, magneto-optical sum rules were applied to the experimental XMCD spectra [49, 50]:

$$M_{\mathrm{L}} = -\frac{2}{3}(A_3 + A_2)\frac{n_{4\mathrm{d}}}{\sigma_{\mathrm{tot}}} \tag{4.5}$$

$$M_S = -(A_3 - 2A_2)\frac{n_{4d}}{\sigma_{tot}} \tag{4.6}$$

To calculate the moments the integrated XMCD signals at the L_2 and L_3 edges (A_2 and A_3) are needed, as well as the number of holes in the Rh 4d band n_{4d} and the total absorption cross-section corresponding to 2p-4d transitions σ_{tot}.

Following the standard procedure [51, 52], the normalized X-ray absorption cross-section per 4d hole, $n_{4d}/\sigma_{tot} = 0.144$, was determined by subtracting the Ag-foil $L_{2,3}$ spectra from the experimental Rh $L_{2,3}$ spectra measured on the FeRh film and taking the theoretical value for the number of Rh 4d holes, 2.34 from Ref. [53].

Using this value, the Rh 4d spin and orbital magnetic moments were derived. For FeRh, the spin and orbital moments are equal to $0.89\mu_B$ and 0.08 μ_B, respectively, at $T = 295$ K. Using exactly the same procedure for the low temperature, the spin and orbital moments magnetic moment per Rh atom at 3 K and under 17 Tesla are equal to 0.19 μ_B and 0.01 μ_B, respectively.

From the XANES spectrum one can define the valence structure. The peak at the pre-edge region identifies the presence of small Fe oxidization [54]. The white line and the nonzero XMCD signal correspond to the 1s-4p dipolar electronic transition. The small XMCD response in comparison with the one on the Rh site, shows the Fe orbital magnetization [55].

Pure Rh ions are paramagnetic and also acquire a moment in an external magnetic field. For 3 K and 17 T the spin moment due to Pauli paramagnetism cannot exceed $0.0027\mu_B$ [56], which is almost two orders of magnitude lower in comparison with the obtained $0.19\mu_B$. However, it couldn't be referred to the ferromagnetism of Rh, observed in clusters ($0.067\mu_B$) [57]. Thus, we suggest that this moment reflects the canting of the Fe magnetization in high magnetic field.

XMCD on Fe and Rh site

As we can see from Fig. 4.5 and 4.6 the changes in the magnetization can be seen not only in Fe but also in Rh L_2 and L_3. Comparison of the XMCD signal at the Rh L_2 and Rh L_3 edges in Figure 4.7 results in the equivalence of the behaviour of the two lines. The data is taken at 3 K far below the phase transition, which allows us to see the canting of the sublattice magnetization. Taking into account that the changes occur on both edges, we can consider the temperature dependence of one of the lines with less noise.

Figure 4.8 demonstrates that the canting and the phase transition occur in both the Fe and Rh sublattices under the same conditions. Thus the evolution of the FeRh net magnetization is visible through the XMCD at any of those three absorption spectra. Due to a better signal-to-noise ratio, we will mainly analyse the results obtained at the Rh L_3 edge.

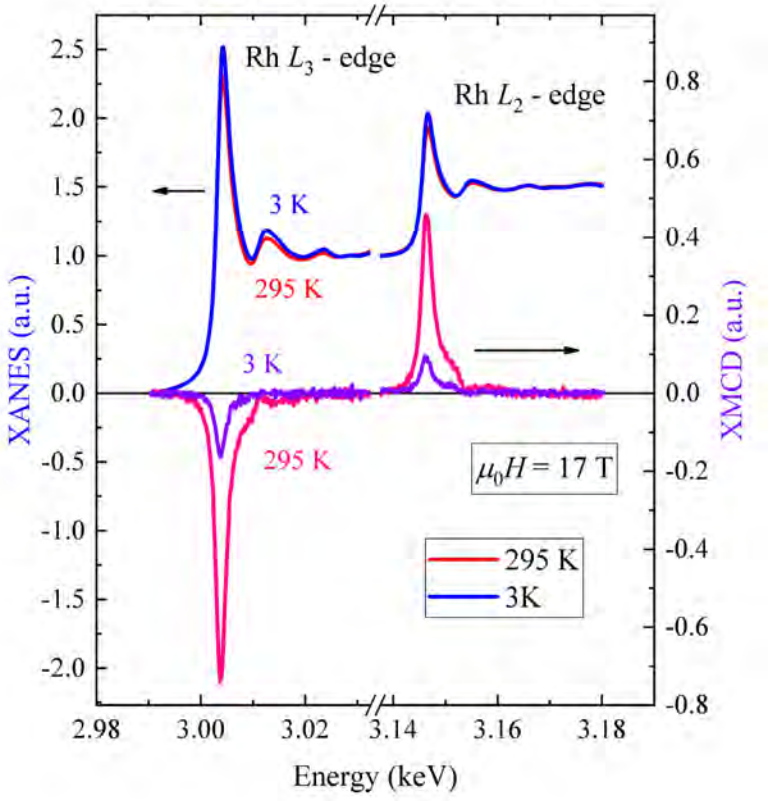

Figure 4.5: XANES and XMCD spectra for the Rh L_2 and L_3 edges at an external magnetic field of 17 T and temperatures 3 K and 295 K. These conditions correspond to FeRh in the antiferromagnetic (3 K) and ferromagnetic state (295 K).

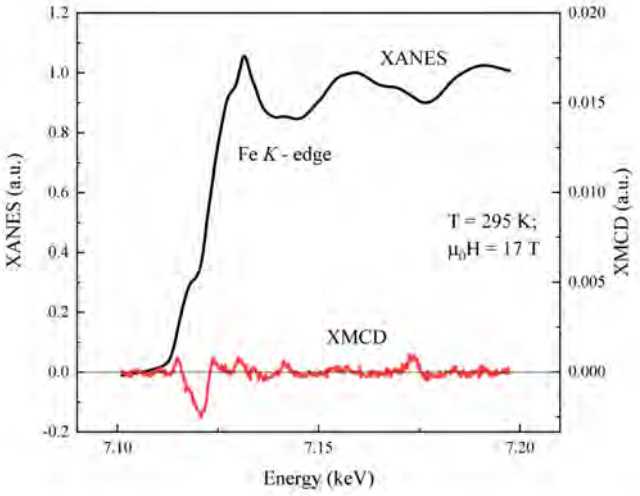

Figure 4.6: XANES and XMCD spectra for the Fe K edge at an external magnetic field of 17 T and room temperature (T = 295 K).

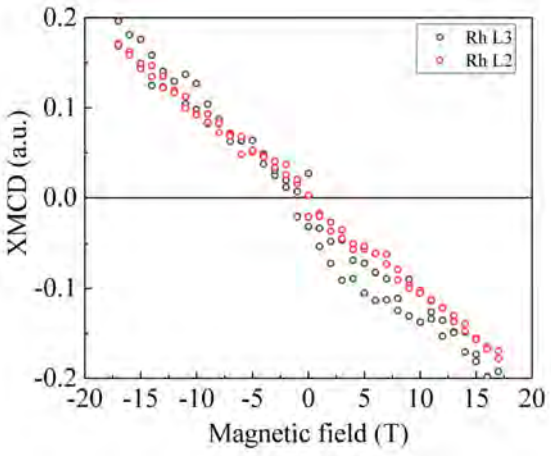

Figure 4.7: XMCD hysteresis at the Rh L_2 and L_3 edge of absorption at 3 K in arbitrary units. The external magnetic field is applied along the sample normal.

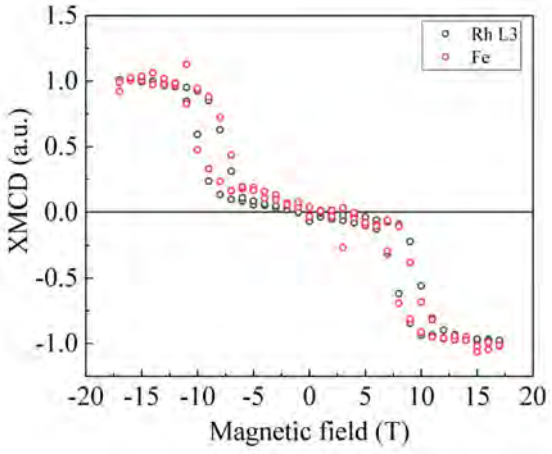

Figure 4.8: XMCD at the Fe and Rh L_3 sites at 325 K. The external magnetic field is applied along the sample normal.

Spin canting below the magnetostructural transiton

The temperature dependence of the XMCD in magnetic fields up to 17 T applied along the sample normal is presented in Figure 4.9. As expected the critical field is shifting to higher external fields with decreased temperature and is not observed within the 17 T range below 270 K. The spin canting before the phase transition does not change significantly with temperature. At 300 K and 325 K, we can observe the saturation of the magnetization and further canting does not occur which shows us that the slope can be indeed attributed to the deviation of the sublattice magnetization from the antiferromagnetic vector. The theoretical model described in Ref.[58] can fit the magnetic behaviour in the XMCD with the following parameters: the potential barrier between the AFM and FM phase $\beta^2 M^4/2E = 3 \times 10^8$[erg/cm^3], where β is the partial derivative of the Fe-Fe exchange with respect to the strain, M - amplitude of the net magnetization of the iron ions and E - Young's modulus; the coupling constant between the Fe and Rh spins $\lambda = 2.3 \times 10^3$[Oe $\cdot$ cm^3/emu], paramagnetic susceptibility of Rh $\chi_\mathrm{p} = 7.5 \times 10^{-4}$(emu/cm^3), and energy gap between the excited and ground state of Rh $\Delta = 600 \times k_\mathrm{b}$ (erg) (Fig. 4.10). However, the theoretical calculation cannot define the type of anisotropy as both sufficiently fit the experimental data. Nevertheless, the observed slopes below the phase transition demonstrate that the canted AFM phase is not suppressed and can be reached above 5 T.

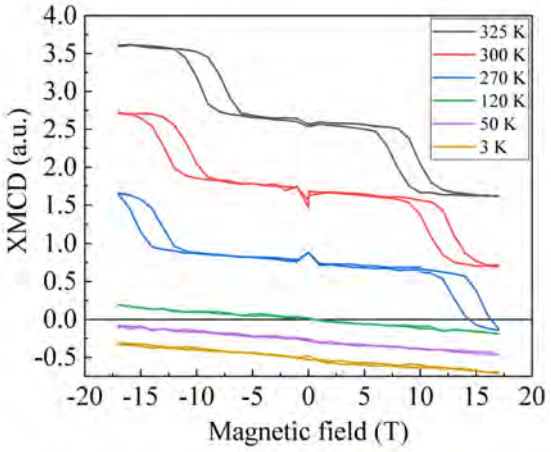

Figure 4.9: Temperature-Dependent XMCD Measurements at Rh L_3 Site. Temperatures are varied in the range from 3 K to 325 K. The external magnetic field is applied along the sample normal.

4.4 Experimental study of ultrafast magnetization dynamics

4.4.1 Experimental details

In order to study the ultrafast magnetization during the magneto-structural phase transition in FeRh, we employed the principle of pump-probe measurements. An intense femtosecond laser pulse (pump) is absorbed in the metallic FeRh and thus acts as an ultrafast heater. A delayed, less intense, but equally short laser pulse (probe) detects the magnetization of the FeRh film via the polar magneto-optical Kerr effect. Detecting the magneto-optical Kerr effect as a function of the time delay between the pump and the probe pulses measures the heat-induced magnetization dynamics with subpicosecond temporal resolution. It is conventionally accepted that for metals, such as FeRh, the magneto-optical Kerr effect is a reliable probe of the magnetization at least for time delays larger than 2 ps [59].

We employed an experimental setup for time-resolved magneto-optical measurements at the High Field Magnetic Laboratory (HFML) in Nijmegen [60]. An amplified Ti:sapphire laser and an Optical Parametric Amplifier (OPA) were employed as ultrafast light sources. The studied sample was put in a cryostat and a Florida-Bitter magnet. The latter allowed us to apply external magnetic fields along the sample normal as strong as 37.5 T. Optical measurements were carried out in the polar geometry of the

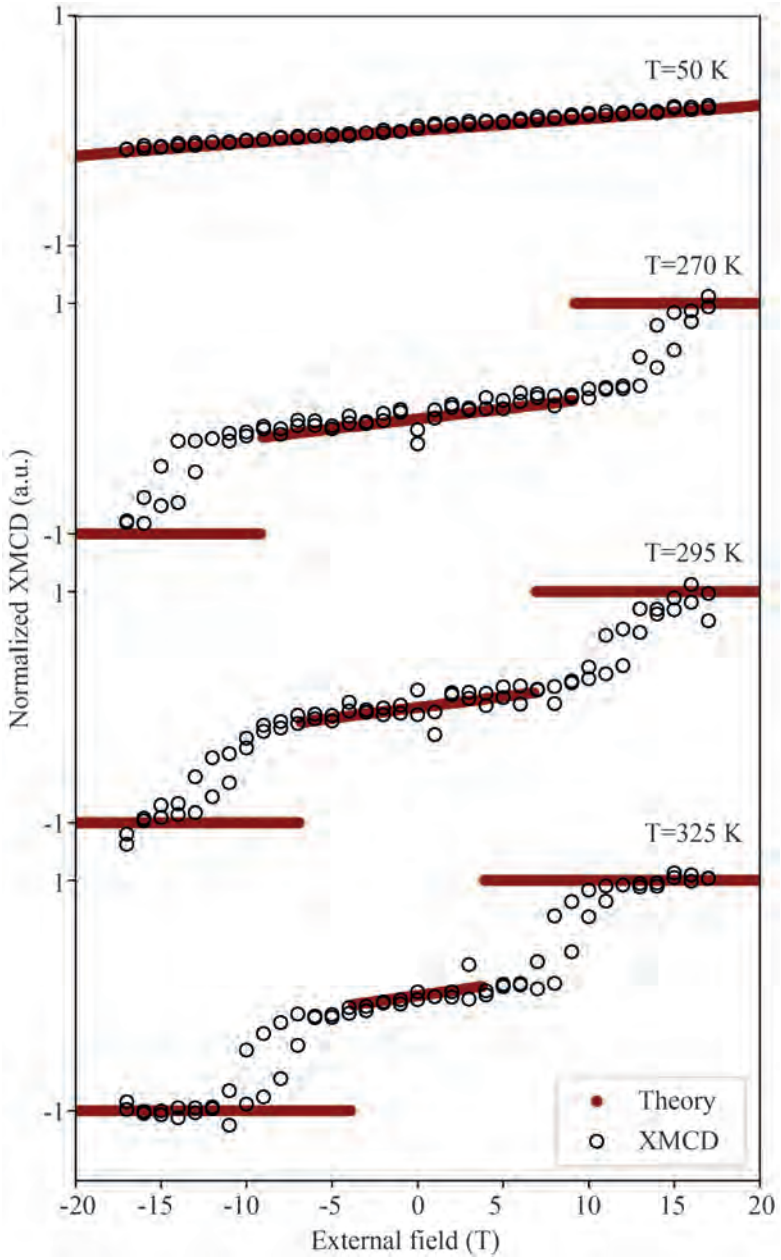

Figure 4.10: Experiment and calculation. Dots represent XMCD data from Fig 4.9 and lines are calculated net magnetization from the model introduced in Ref.[58]. The figure is adapted from Ref.[58] with permission.

magneto-optical Kerr effect with the pump and the probe at normal incidence to the sample. The pump pulse had a fluence of 4.1 mJ/cm^2 at a central wavelength of 800 nm (1.55 eV). The pump beam was focused on a spot of approximately 50 μm in diameter. The pump-induced magnetization dynamics was observed with probe pulses having a central photon energy of 1.9 eV (660 nm). We estimated the duration of the optical pulses at the sample to be around 150 fs.

Pump pulses were effectively absorbed in the sample. Taking into account the diameter of the focused pump (50 μm), the pump fluence (4.1 mJ/cm^2), the specific heat of FeRh (0.35 J/g K [35]), and assuming that the sample absorbs 20 % of the pump radiation [61], we estimate that a single pump laser pulse heats the upper 10 nm layer of the FeRh film by about 230 K. The pump-induced polarization rotation ($\Delta\theta$) due to the polar magneto-optical Kerr effect and the reflectivity change (ΔR) of the probe pulses reflected from the sample were detected with the help of a two-photodiode balanced detector.

4.4.2 Dependence on magnetic field and temperature

The horizontal black arrows in Figure 4.11(a) show that by properly choosing the values of the applied magnetic field $\vec{H}$ and temperature T, one should be able to start an ultrafast heating experiment from different phases. For instance, at $T = 200$ K and $H = 5$ T, heating over a range of 230 K should cause a phase transition from the collinear AFM to the FM phase (denoted by the route type 1 arrow). At $T = 200$ K and $H = 10$ T, the same heating should trigger a transition from the canted AF to the FM phases (route type 2). Finally, at 200 K and the highest field $H = 25$ T, the heating would partially destroy the ferromagnetic order leading to demagnetization (route type 3).

Interestingly, if the heating is ultrafast and realized with the help of fs-laser pulses [15, 16], each of these three routes must have distinctly different kinetics. Indeed, the dynamics of spin $\vec{S}$ in the effective exchange field of its neighbouring spins $\vec{H}_{\text{ex}}$ must obey the fundamental law of conservation of angular momentum $\frac{d\vec{S}}{dt} = -\gamma[\vec{S} \times \vec{H}_{\text{ex}}]$, where γ is the gyromagnetic ratio.

When the system is in the collinear antiferromagnetic state, an instantaneous change of the sign of the effective exchange interaction $\vec{H}_{\text{ex}}$ does not immediately launch spin dynamics. Since the spins are collinear, the torque acting on the spin is zero $[\vec{S} \times \vec{H}_{\text{ex}}] = 0$, and starting the spin dynamics requires an additional trigger leading to a latency $\Delta\tau$ as shown in Ref. [25]. When the antiferromagnet is in a canted state $[\vec{S} \times \vec{H}_{\text{ex}}] \neq 0$ a change of the exchange interaction will instantaneously launch the spin dynamics. Therefore, it is clear that the kinetics of the phase transition to the FM phase from the collinear and from the canted AFM phases must be substantially different. Finally, if FeRh is already in a FM phase, ultra-

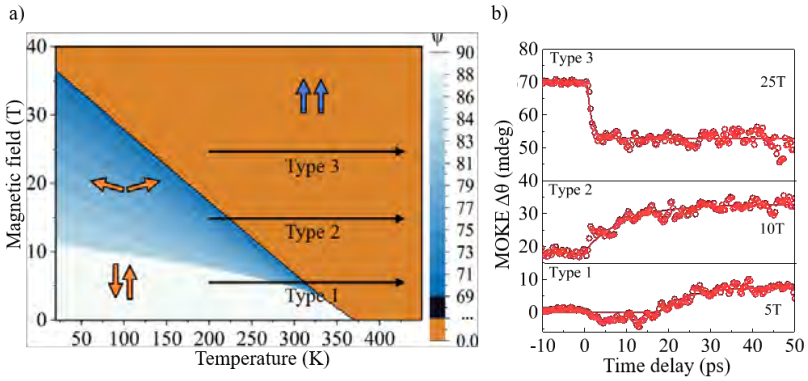

Figure 4.11: (a) Numerically calculated H-T phase diagram using the thermodynamic potential described in the text: light blue region – collinear AFM phase, dark blue region – canted AFM phase, brown region – FM phase. The horizontal black arrows schematically illustrate the three different types of pathways into the FM phase upon ultrafast laser heating at 200 K for 230 K, depending on whether the initial phase is collinear AFM (type 1), canted AFM (type 2) or FM (type 3). (b) The laser-induced change in the polarization rotation $\Delta\theta$ (red circles) shows the polar magneto-optical Kerr effect at applied magnetic fields of 5 T, 10 T, and 25 T corresponding to routes of types 1, 2, and 3, respectively. All the curves were taken at $T =$ 200 K. The solid red lines are fits with $\Delta\theta(t) = B_{\mathrm{M}}\left(1 - e^{-\frac{t-\Delta\tau}{\tau_{\mathrm{M}}}}\right)$, where $\tau_{\mathrm{M}} = 7 \pm 1.3$ ps for route 1, $\tau_{\mathrm{M}} = 8 \pm 0.5$ ps for route 2, and $\tau_{\mathrm{M}} = 760 \pm 110$ fs for route 3. For route 1, a latency appears in the dynamics, similar to Ref. [25], which is estimated to be $\Delta\tau = 17.9 \pm 0.6$ ps.

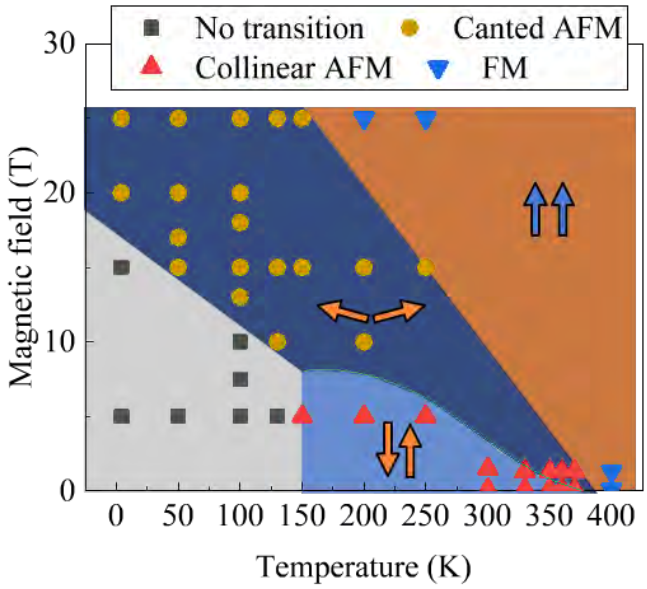

Figure 4.12: Phase diagram deduced from laser-induced dynamics of the magneto-optical Kerr effect represented in Fig. 4.17. Every time-resolved trace was assigned to a certain route type of ultrafast dynamics depending on the sign of the amplitude B_M and the presence of latency ($\Delta\tau$). In the blue area (and $\Delta\tau > 0$) laser excitation triggers dynamics along Route 1 (red triangles). In the dark blue area ($B_{\mathrm{M}} > 0$ and $\Delta\tau = 0$), the observed dynamics is assigned to Route 2 (brown circles). In the brown area ($B_{\mathrm{M}} < 0$ and $\Delta\tau = 0$), the dynamics is assigned to Route 3 (blue triangles). In the grey area, the dynamics showed too low amplitudes, which could not be reliably assigned to any of these three types (black squares).

fast heating with the help of a femtosecond laser pulse results in ultrafast demagnetization [31]. Aiming to reveal how the ultrafast magnetization dynamics actually change upon changing the initial phase, we perform a time-resolved pump-probe magneto-optical study of FeRh in fields up to 25 T at several base temperatures.

The resulting laser-induced dynamics for routes 1, 2, and 3 at $T = 200$ K in fields 5 T, 10 T, and 25 T are shown in Fig. 4.11(b) (red circles). At $H = 5$ T, the MOKE signal exhibits a profound latency $\Delta\tau$ similar to Ref. [25], until the MOKE signal starts to rise (similar behaviour can be observed at higher temperatures, see Fig. 4.16). The polarization rotation is fitted with the function $\Delta\theta(t) = B_{\mathrm{M}}\left(1 - e^{-\frac{t-\Delta\tau}{\tau_{\mathrm{M}}}}\right)$ (solid red curves in Fig 4.11(b). Here B_{M} andτ_{M} are the amplitude and the characteristic time corresponding to the laser-induced magnetic changes. From the fit of the data obtained at $H = 5$ T, we find that $B_{\mathrm{M}} > 0, \tau_{\mathrm{M}} = 7.0 \pm 1.3$ ps, and $\Delta\tau = 17.9 \pm 0.6$ ps. At $H = 10$ T, the observed dynamics is substantially different and no latency is seen ($B_{\mathrm{M}} > 0$, $\Delta\tau = 0$). The magnetization starts to grow immediately after the pump excitation and saturates with a characteristic time $\tau_{\mathrm{M}} = 8.0 \pm 0.5$ ps. Further increase of the magnetic field strength up to $H = 25$ T substantially changes the dynamics. The amplitude changes sign ($B_{\mathrm{M}} < 0$) and the dynamics acquires characteristic features of ultrafast demagnetization with a demagnetization time of $\tau_{\mathrm{M}} = 760 \pm 110$ fs ($\Delta\tau = 0$). These three types of dynamics can be attributed to the three types of routes shown in Fig. 4.11(a). To illustrate the behaviour within each of the three routes, we measured the laser-induced dynamics at various magnetic fields and temperatures. Each of the observed transients has been assigned to one of the three types shown in Fig. 4.11(b): type 1 ($B_{\mathrm{M}} > 0$, $\Delta\tau \neq 0$), type 2 ($B_{\mathrm{M}} > 0$, $\Delta\tau = 0$) and type 3 ($B_{\mathrm{M}} < 0$, $\Delta\tau = 0$). To simplify the assignment procedure, we neglect changes of $\Delta\theta$ less than 10% of the maximum demagnetization signal. For instance, the dynamics obtained at 200 K and 5 T, as shown in Fig 4.11(b), has been attributed to type 1, even though between 0 ps and 18 ps the signal is strictly speaking not zero. The results of the classification are shown in Fig. 4.12, where one can clearly distinguish three different regions for those cases when the dynamics exhibited a sufficiently high amplitude The resulting regions with routes of type 1, 2, and 3 are in close agreement with the regimes where we expected to find antiferromagnetic collinear, antiferromagnetic canted, and ferromagnetic starting phases (see Fig. 4.11(a)), respectively.

Hence, Figs. 4.11(a) and 4.12 support our hypothesis that by varying the external magnetic field one can substantially modify the dynamics triggered by ultrafast heating. Note that at low fields and low temperatures, transients could not be assigned to one of the three types (black squares in Fig 4.12). We believe that in this case, the pump pulse does not provide enough heat to reach the FM phase.

In order to reveal the fastest possible phase transition from an antifer-

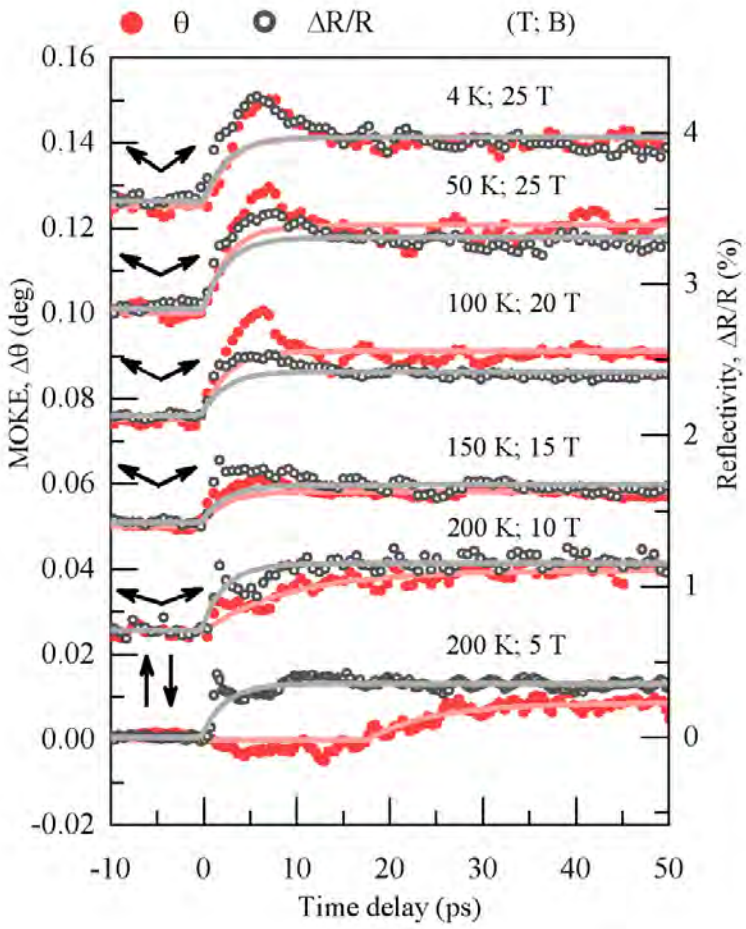

Figure 4.13: Ultrafast kinetics of the magneto-structural transition. The polarization rotation due to the magneto-optical Kerr effect (red) and reflectivity change $\Delta R/R$ (black) at various temperatures and magnetic fields. Open circles represent the experimental data and the solid lines are their respective fits. The curves are plotted with an offset along the y-axis.

romagnetic to a ferromagnetic phase, one should focus on the dynamics without latency and thus explore route type 2 in ever-higher magnetic fields.

Figure 4.13 shows a selection of the typical time traces of the MOKE signal (open red symbols) measured at temperatures down to 4 K and in magnetic fields up to 25 T. While the MOKE signal at 5 T is characterized by a latency, at higher fields, the dynamics changes dramatically and the latency disappears (see also dynamics at fixed $T = 100$ K, Fig. 4.14). We fitted the data obtained for fields above 10 T with the function without latency $\Delta\theta(t) = B_{\mathrm{M}}\left(1 - e^{-\frac{x}{\tau_{\mathrm{M}}}}\right)$ considering only the growing part with the rise time τ_{M}.

Interestingly, the characteristic time τ_{M} hardly depends on the field strength and we can average the obtained τ_{M} for all fields above 15 T. This procedure gives $\tau_{\mathrm{M}} = 2.51 \pm 0.20$ ps. Hence, for the fits shown in Fig.4.13 and in the rest of the curves (see Fig. 4.17), we fixed the time $\tau_{\mathrm{M}} = 2.5$ ps and fitted only the amplitudes.

4.4.3 Ultrafast lattice dynamics and time-resolved reflectivity measurements

Almost 20 years ago it was suggested that ultrafast lattice relaxation resulting from a magneto-structural phase transition in FeRh can be monitored by measuring time-resolved reflectivity changes (Ref. [15]). The reported timescale for the observed lattice expansion was 5-10 ps. Lattice expansion upon a phase transition from an AFM to FM state in FeRh within the first 6 ps was confirmed by time-resolved X-ray diffractometer [20]. In our experiments, time-resolved reflectivity changes were measured simultaneously with the MOKE dynamics. As explained in Ref. [15], the obtained transients (black symbols in Fig. 4.13) contain contributions from the electronic part and the lattice part. For instance, the rapid increase and relaxation of the reflectivity signal in the first 2 ps after ultrafast laser excitation are conventionally assigned to be due to ultrafast heating and cooling of free electrons. Ignoring this first transient, the slower growth is fitted with a similar expression as for the magnetization dynamics: $\frac{\Delta R}{R}(t) = A_{\mathrm{L}}\left(1 - e^{-\frac{t}{\tau_{\mathrm{L}}}}\right)$, where A_{L} and τ_{L} are the amplitude and the characteristic time presumably corresponding to the laser-induced lattice expansion. The fits are shown in the figure by the black solid curves. The rise time τ_{L} does not depend on the magnetic field and therefore we fixed it at $\tau_{\mathrm{L}} = 2.5$ ps.

Fig. 4.14 shows the dynamics at a fixed temperature ($T = 100$ K). Here it can be seen that just an increase of the magnetic field strength induces the corresponding dynamics of Route 2 not only in the MOKE channel but also in reflectivity.

If the observed reflectivity and the MOKE dynamics correspond to the

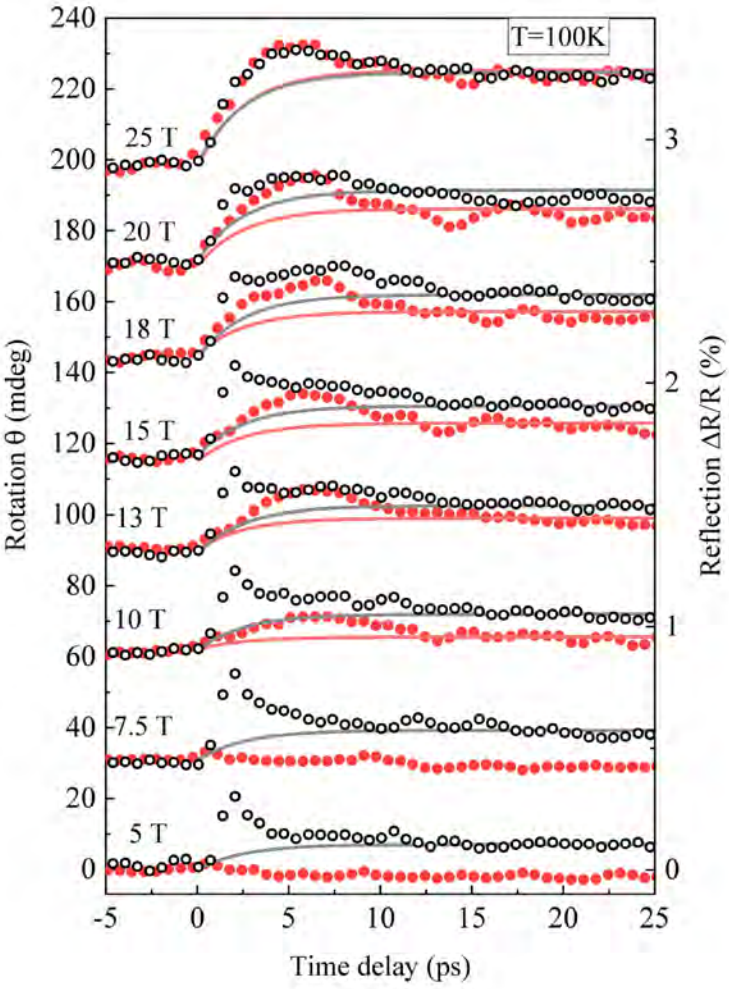

Figure 4.14: Ultrafast kinetics of the magneto-structural transition. (a) The polarization rotation induced by the magneto-optical Kerr effect (red) and reflectivity change $\Delta R/R$ (black) at 100 K and various magnetic fields. The open circles represent the experimental data and the solid lines are their respective fits. The curves are plotted with an offset along the y-axis.

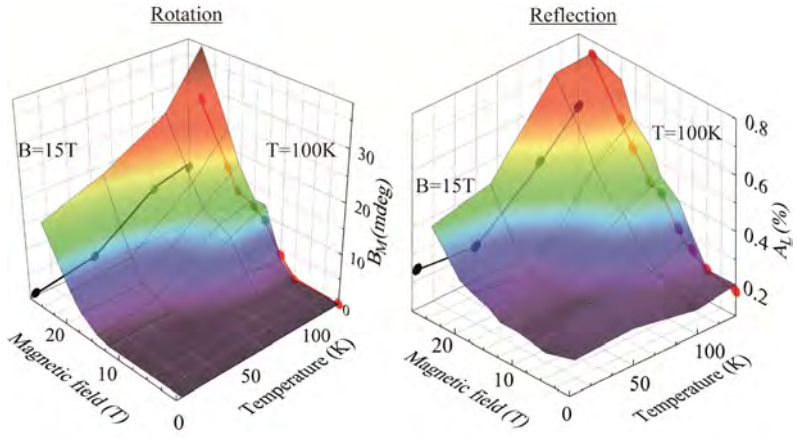

Figure 4.15: Three-dimensional (3D) surface plots showing the amplitudes A_{L} and B_{M} of ultrafast magneto-structural changes. Plane curves correspond to a slice of the surface taken at the fixed temperature $T = 100$ K (red) or the fixed magnetic field $H = 15$ T (black). (a) The MOKE amplitude B_{M} reveals ultrafast laser-induced magnetization. (b) The amplitude of ultrafast laser-induced reflectivity change A_{L} is presumably assigned to the lattice expansion.

magneto-structural phase transition, the amplitudes A_{L} and B_{M} must be proportional to the probability of the nucleation of the FM phase. The latter, in accordance with the Arrhenius equation, must be proportional to $\exp(-\frac{E_{\mathrm{a}}}{k_{\mathrm{B}}T})$, where k_{B} is the Boltzmann constant and E_{a} is the activation energy for the nucleus [62]. In the case of FeRh, E_{a} is a function of the applied magnetic field. Plotting A_{L} and B_{M} as a 3D graph (Fig. 4.15) we see qualitative agreement with the Arrhenius equation - the amplitudes increase with increasing either the temperature or the magnetic field strength. This trend is observed as long as most of the probed FeRh volume is in the AFM state. Approaching the critical magnetic field and temperature, co-existing FM domains will start to dominate the signal and the trend will change completely. All these observations point out that the amplitudes A_{L} and B_{M} serve as a measure of the volume, which undergoes structural and magnetic changes at the phase transition from the AFM to the FM states (comparison for higher temperatures as well is shown in Fig. 4.18).

The rise time $\tau_{\mathrm{L}} = 2.5$ ps is in good agreement with the expected time of expansion of the studied film, which can be estimated as $\tau_{\mathrm{L}} \approx \frac{d_{\mathrm{depth}}}{v}$, where $v \approx 4 \cdot 10^3$ m/s is the speed of sound taken from Ref. [63] and d_{depth} is the penetration depth of the probe light in the film at the probe wavelength. According to Ref. [20], the penetration depth for pump and probe pulses

in our experiment is about 15 nm. However, if one takes into account the thickness of the capping Pt layer, we obtain $d_{\mathrm{depth}} \approx 10$ nm. Note that in the range from 2 ps to 10 ps, the simple fit does not fully reproduce the trend observed experimentally implying that the real lattice dynamics is more complex than a trivial expansion of the lattice.

Nevertheless, it is clear that $\tau_{\mathrm{M}} \approx \tau_{\mathrm{L}}$ i.e. the dynamics of the MOKE and the reflectivity signal correlate very well. Hence if we assume that the dynamics of the reflectivity corresponds to the dynamics of the lattice expansion, it would mean that for sufficiently high magnetic fields the laser-induced magnetization emerges as fast as the lattice expands (see Fig. 4.13). Applying even higher fields does not accelerate either the lattice or the spin dynamics. It suggests that the lattice expansion and the magnetization emergence occur simultaneously on a sub-10 ps timescale defined by the thermal expansion of the lattice. Previous studies of the phase transition with the help of X-ray techniques reported similar characteristic times of the lattice expansion. The latter were shown to be defined by the speed of sound and the thickness of the film. Ref. [20] reported a shift of the Bragg peak already within the first 6 ps for a 47 nm thick film, while in Ref. [64] similar measurements on a film with a thickness of 100 nm showed a shift of the Bragg peak after 18.5 ps. XAS measurements on 30 nm thick demonstrated changes on a sub-10 ps timescale [18]. Thus, in the case of the film with a thickness of 40 nm, the lattice expansion should result in a reflectivity change on a sub-10 ps timescale as well.

The observed magneto-structural dynamic correlations suggest two possible scenarios. As the essence of the net magnetization induced in the ferromagnetic state is the angular momentum, conservation of the angular momentum must play in these scenarios the central role. In the first scenario, the effective antiferromagnetic exchange interaction acting between the two iron sublattices turns into a ferromagnetic one much faster than 2 ps, but the observed magnetization dynamics occurs on the scale of the lattice dynamics and is practically defined by the rate at which the lattice can exchange angular momentum with spins. Note that recent experiments revealed lattice dynamics upon ultrafast demagnetization of ferromagnetic Ni and Fe. The findings imply that the exchange of angular momentum between the lattice and spins at the sub-ps timescale is quite realistic [65, 66]. Hence we rather favour the second scenario, where the effective field of the exchange interaction $\vec{H}_{\mathrm{ex}}$ changes on the scale of the lattice expansion, and the response of the spins as well as the exchange of angular momentum are fast enough to follow these changes.

4.4.4 Latency in time-resolved MOKE

In preparation for the experiments with high magnetic fields, we executed a time-resolved study of the AF to FM transition at room temperature in external magnetic fields up to 1.3 T. The same procedure as discussed

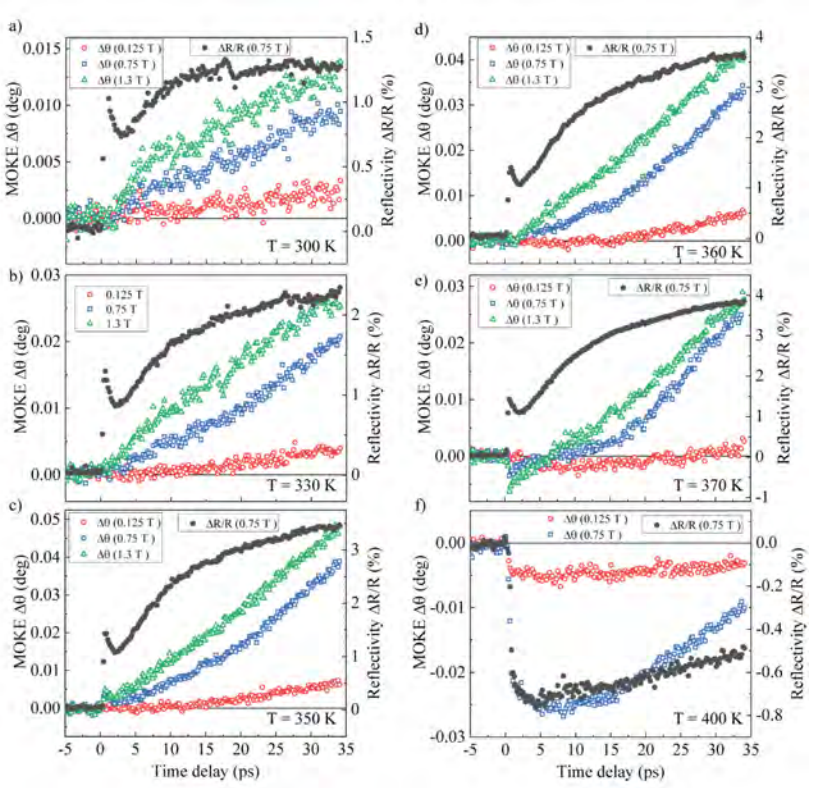

Figure 4.16: Time-resolved polar MOKE and Reflectivity above room temperature (from 300 K to 400 K). The laser-induced reflectivity change (black filled circles) and the polarization rotation as a result of the magneto-optical Kerr effect at applied magnetic fields of 0.125 T (circles), 0.75 T (squares), and 1.3 T (triangles).

in the manuscript was followed. We probed simultaneously both parts of the laser-induced response: P-MOKE and Reflectivity being the differential and summary signals of the p- and s- polarization components respectively.

It has been widely accepted that on a timescale longer than 2 ps, the MOKE is a reliable probe of the magnetization dynamics [15] while the reflectivity change in FeRh is due to both the dynamics of the electrons and the lattice. In particular, it is well accepted that a rapid increase and a partial recovery of the transient reflectivity $\Delta R/R$ on the scale up to 1-2 ps is due to the electron temperature dynamics [67] and the slower dynamics of $\Delta R/R$ with a characteristic time of $\tau_L = 4$ ps can be attributed to the lattice expansion [15, 18]. Although there is a slight discrepancy between τ_{L} estimated for the dynamics below 200 K and at 300 K, one must keep in mind that the sound velocity in compounds with structural transitions is not constant as a function of temperature. In particular, heating the sample towards the transition temperature can result in a decrease of the sound velocity and its non-linear behaviour with a jump at T_{c}, which was observed in materials with a metamagnetic transition from the AF to the FM phase [45, 68].

Figure 4.16 shows the laser-induced dynamics of both the P-MOKE and reflectivity measured in FeRh at room temperature for fields of 0.125 T, 0.75 T, and 1.3 T applied perpendicular to the sample plane. The 800 nm pulse of 4.1 mJ/cm^2 with an excitation spot size of 50 μm in diameter does not lead to sub-picosecond dynamics of the net magnetization. A study of time-domain THz emission spectroscopy on a similar sample showed that the sub-picosecond magnetization dynamics is due to a pump-induced expansion or demagnetization of pre-existing FM domains and not due to the phase transition from the AF to the FM phase [31]. Magnetization probed with the help of the P-MOKE emerges in the medium on a much longer timescale in agreement with Refs. [17, 20] following route type 1 from Fig. 4.11. For all traces from Fig. 4.16 dynamics occurs with a latency similar to what was observed at 5 T and 200 K, where latency in the emergent magnetization is present during the first 18 ps (see Fig. 4.11). Here, its duration decreases from 15 ps to 1.6 ps in 1.3 T. The observed rise in the characteristic time can be connected with the significant temperature difference. Investigating even lower temperatures, e.g. 100 K in magnetic fields up to 25 T (Fig. 4.14), we could not observe any latency. However, according to our estimation of the temperature rise provided by the pump, we were not heating enough to induce ferromagnetism at 5 T. All time-resolved dynamics above 7.5 T occurred according to Route type 2.

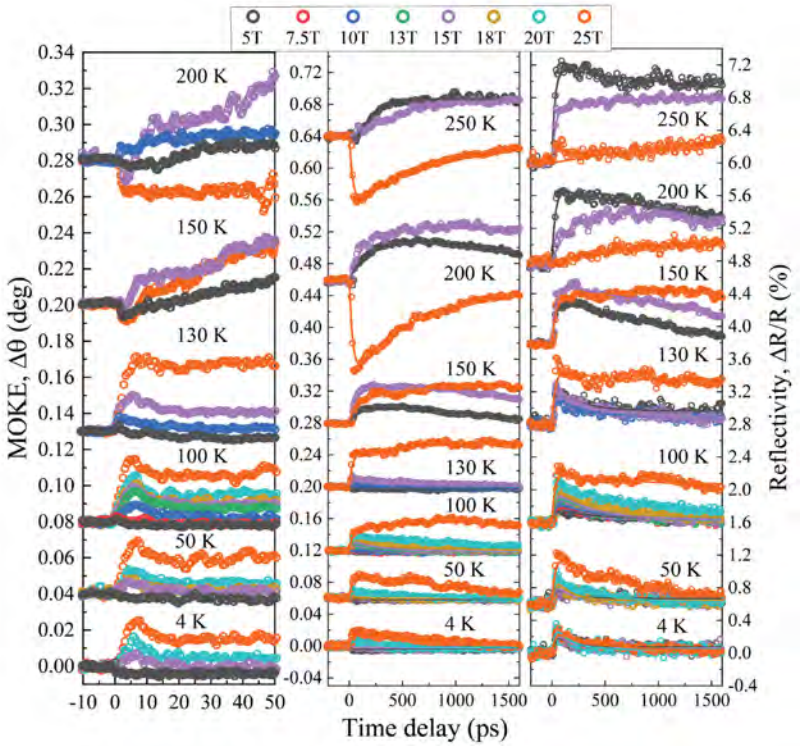

Figure 4.17: Time-resolved Magneto-optical Kerr effect. Panel (a) shows time-resolved MOKE signals for time delays up to 50 ps. This data was used for building the phase diagram shown in Fig. 4.3. Panel (b) shows laser-induced changes in the MOKE signal for delays up to 1.5 ns; Panel (c) shows the changes in reflectivity. The data was obtained in the range of temperatures from 4 K to 250 K. The external magnetic field was varied from 5 T to 25 T. Different colors correspond to different magnetic fields, denoted at the top of the figure.

4.4.5 Long range dynamics of the phase transition in FeRh

Figure 4.17(a) shows the dynamics of the transient polarization rotation of the probe pulse obtained in magnetic fields up to 25 T during the first 50 ps after excitation, and Fig. 4.17(b,c) shows MOKE together with the reflectivity during 1.5 ns after pumping. Both measurements were performed simultaneously using the pump-probe method. The observed dynamics is very sensitive to both the applied magnetic field and the temperature. For instance, at 4 K and for magnetic fields below 20 T we hardly observe any laser-induced polarization rotation. The dynamics of the transient reflectivity measured in fields below 20 T are nearly independent on the field and have a form typical for the case when only an electronic contribution to the transient reflectivity is expected [67]. An increase of the field results in both an increase of the laser-induced polarization rotation and an additional contribution to the transient reflectivity. At higher temperatures, the field influences the laser-induced dynamics in the polarization rotation, and the reflectivity becomes even higher. In the temperature range of 4 K to 150 K, both the laser-induced polarization rotation (probing the net magnetization) and the reflectivity (probing the lattice expansion) increase when approaching the phase transition (Fig. 4.15). At temperatures above 150 K and fields above 20 T, we observe an appreciable change of the laser-induced polarization rotation where the amplitude changes sign. Such a change of sign occurs because the medium is already in the state with co-existing AF and FM phases under these experimental conditions. Ultrafast laser excitation results not only in the transition from the AF to the FM phase but also in the demagnetization of the co-existing FM phase. If the FM phase dominates over the AF phase state, the signal originating from the laser-induced demagnetization will dominate because the sample resides uniformly in the FM phase.

4.5 Comparison of the amplitudes A_L and B_M in wide *H-T* range

Figure 4.4(a,c) shows the MOKE signal strength at the time delay of 100 ps after the ultrafast laser excitation as a function of temperature at fixed fields (Fig. 4.18(a)) and as a function of the field at fixed temperatures (Fig. 4.18(c)). It is seen that up to 150 K the MOKE only increases upon an increase of the field or temperature. A similar trend is also observed in the reflectivity signal (Fig. 4.18(b)). This observation once again confirms that, at least for the measurements up to 150 K, both the transient MOKE and the reflectivity contain information about the ns kinetics of the phase transition from the AF to the FM state. The observed trends measured at 100 ps are in excellent agreement with the trend at the sub-10

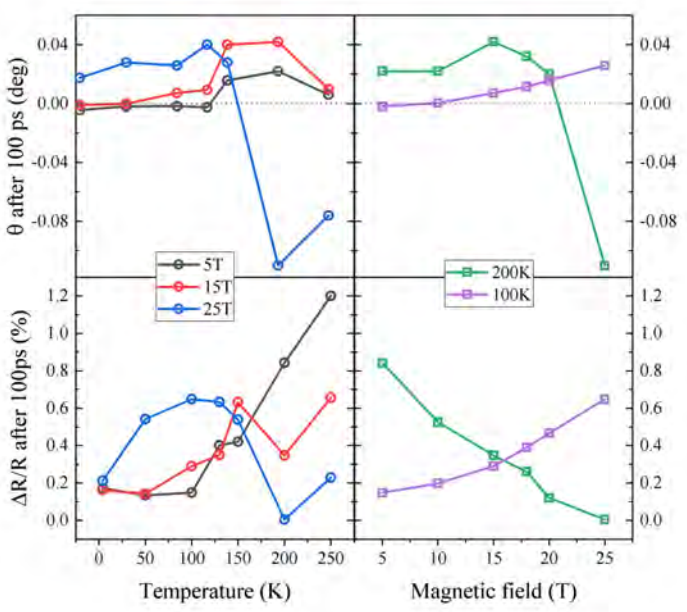

Figure 4.18: The laser-induced polarization rotation and reflectivity change at the time delay of 100 ps extracted from Fig. 4.17. Panels a and c correspond to the polarization rotation at fixed fields and temperatures, respectively; Panels b and d correspond to the reflectivity at fixed fields and temperatures, respectively.

ps timescale. Further increasing the magnetic field and the temperature leads to the change of a sign of θ, which indicates the transition to the FM phase. Besides this, we should take into account the time difference with the process of the phase transition. The response from the FM nucleus is on a sub-picosecond timescale as can be seen from Figure 4.17. Therefore, Fig. 4.18 does not leave any further doubts that the dynamics shown in Fig. 4.13 reveals the ultrafast kinetics of the phase transition from the AF to the FM state.

The dependencies shown in Fig. 4.17 can be fitted with two exponential contributions corresponding to growth with a characteristic time of roughly 0.2 - 0.5 ns and a relaxation with a decay time of 2 ns. The timescale of the growth is in agreement with the data reported earlier and must be due to the expansion process of the FM phase [15, 16, 20]. The characteristic time of the growth weakly depends on the applied magnetic field. Its trend is opposite to the one expected if the growth is due to an alignment of the magnetization of the FM domains. In particular, the characteristic time measured at 250 K and 15 T ($\tau \approx 600$ ps) is even slower than the one measured at 5 T ($\tau \approx 250$ ps). Therefore, it shows that the growth mechanism cannot have a magnetic origin and must be assigned to thermalization and the establishment of thermal equilibrium between phonons and spins. The relaxation corresponds to the timescale of cooling down.

4.6 Summary

Exploring the peculiarities of the $H - T$ diagram of FeRh, we identified possible spin arrangements in this material. Variation of magnetic fields and temperatures allows for obtaining three different types of laser-induced magnetization dynamics in FeRh. These differences are explained by three different initial states of the spin order in FeRh, corresponding to collinear antiferromagnetic, canted antiferromagnetic, and ferromagnetic phases. It is shown that the applied magnetic field can accelerate the emergence of the ferromagnetic phase only to a certain limit. Moreover, we report on the time-resolved measurements of the reflectivity, which contain information about the dynamics of the structural changes in FeRh. We discovered a regime when the magnetization emergence coincides with the changes in reflectivity. It can mean that the spin dynamics is accelerated up to the timescale of the accompanying structural changes. We additionally support this interpretation by simulations showing that the observed changes in the magnetization dynamics are intrinsic even to the simplistic two-spin model and thus must be a general feature of all antiferromagnets and not only FeRh. The revealed dynamics agrees with the proposed interpretation that ultrafast heating of FeRh in the canted antiferromagnetic phase launches the instantaneous emergence of the magnetization with the rate of the lattice expansion. The results show that the magnetism-or-lattice causality

dilemma is resolved by the simultaneous evolution of both actors.

Bibliography

[1] M. Fallot, Annales de Physique **11**, 291 (1938), ISSN 0003-4169, 1286-4838.

[2] L. H. Lewis, C. H. Marrows, and S. Langridge, Journal of Physics D: Applied Physics **49**, 323002 (2016), ISSN 0022-3727, 1361-6463.

[3] M. P. Belov, A. B. Syzdykova, and I. A. Abrikosov, Physical Review B **101**, 134303 (2020), ISSN 2469-9950, 2469-9969.

[4] M. A. de Vries, M. Loving, A. P. Mihai, L. H. Lewis, D. Heiman, and C. H. Marrows, New Journal of Physics **15**, 013008 (2013), ISSN 1367-2630.

[5] N. Pérez, A. Chirkova, K. Skokov, T. Woodcock, O. Gutfleisch, N. Baranov, K. Nielsch, and G. Schierning, Materials Today Physics **9**, 100129 (2019), ISSN 25425293.

[6] T. Zhou, M. Cher, L. Shen, J. Hu, and Z. Yuan, Physics Letters A **377**, 3052 (2013), ISSN 03759601.

[7] C. Kittel, Physical Review **120**, 335 (1960), ISSN 0031-899X.

[8] P. Tu, A. J. Heeger, J. S. Kouvel, and J. B. Comly, Journal of Applied Physics **40**, 1368 (1969), ISSN 0021-8979, 1089-7550.

[9] J. B. McKinnon, D. Melville, and E. W. Lee, Journal of Physics C: Solid State Physics **3**, S46 (1970), ISSN 0022-3719.

[10] O. N. Mryasov, Phase Transitions **78**, 197 (2005), ISSN 0141-1594, 1029-0338.

[11] J. Barker and R. W. Chantrell, Physical Review B **92**, 094402 (2015), ISSN 1098-0121, 1550-235X.

[12] B. R. McGrath, R. E. Camley, and K. L. Livesey, Physical Review B **101**, 014444 (2020), ISSN 2469-9950, 2469-9969.

[13] M. Menarini, R. Medapalli, E. E. Fullerton, and V. Lomakin, AIP Advances **9**, 035040 (2019).

[14] R. M. Vieira, O. Eriksson, A. Bergman, and H. Herper, Journal of Alloys and Compounds **857**, 157811 (2021), ISSN 09258388.

[15] G. Ju, J. Hohlfeld, B. Bergman, R. J. M. van de Veerdonk, O. N. Mryasov, J.-Y. Kim, X. Wu, D. Weller, and B. Koopmans, Physical Review Letters **93**, 197403 (2004), ISSN 0031-9007, 1079-7114.

[16] J.-U. Thiele, M. Buess, and C. H. Back, Applied Physics Letters **85**, 2857 (2004), ISSN 0003-6951, 1077-3118.

[17] B. Bergman, G. Ju, J. Hohlfeld, R. J. M. van de Veerdonk, J.-Y. Kim, X. Wu, D. Weller, and B. Koopmans, Physical Review B **73**, 060407 (2006), ISSN 1098-0121, 1550-235X.

[18] I. Radu, C. Stamm, N. Pontius, T. Kachel, P. Ramm, J.-U. Thiele, H. A. Dürr, and C. H. Back, Physical Review B **81**, 104415 (2010), ISSN 1098-0121, 1550-235X.

[19] J. Cao, N. T. Nam, S. Inoue, H. Y. Y. Ko, N. N. Phuoc, and T. Suzuki, Journal of Applied Physics **103**, 07F501 (2008), ISSN 0021-8979, 1089-7550.

[20] S. O. Mariager, F. Pressacco, G. Ingold, A. Caviezel, E. Möhr-Vorobeva, P. Beaud, S. L. Johnson, C. J. Milne, E. Mancini, S. Moyerman, et al., Physical Review Letters **108**, 087201 (2012), ISSN 0031-9007, 1079-7114.

[21] F. Pressacco, D. Sangalli, V. Uhlíř, D. Kutnyakhov, J. A. Arregi, S. Y. Agustsson, G. Brenner, H. Redlin, M. Heber, D. Vasilyev, et al., Nature Communications **12**, 5088 (2021), ISSN 2041-1723.

[22] C. Baldasseroni, C. Bordel, C. Antonakos, A. Scholl, K. H. Stone, J. B. Kortright, and F. Hellman, Journal of Physics: Condensed Matter **27**, 256001 (2015), ISSN 0953-8984, 1361-648X.

[23] D. J. Keavney, Y. Choi, M. V. Holt, V. Uhlíř, D. Arena, E. E. Fullerton, P. J. Ryan, and J.-W. Kim, Scientific Reports **8**, 1778 (2018), ISSN 2045-2322.

[24] C. Baldasseroni, C. Bordel, A. X. Gray, A. M. Kaiser, F. Kronast, J. Herrero-Albillos, C. M. Schneider, C. S. Fadley, and F. Hellman, Applied Physics Letters **100**, 262401 (2012), ISSN 0003-6951, 1077-3118.

[25] G. Li, R. Medapalli, J. H. Mentink, R. V. Mikhaylovskiy, T. G. H. Blank, S. K. K. Patel, A. K. Zvezdin, Th. Rasing, E. E. Fullerton, and A. V. Kimel, Nature Communications **13**, 2998 (2022), ISSN 2041-1723.

[26] V. L. Moruzzi and P. M. Marcus, Physical Review B **46**, 2864 (1992), ISSN 0163-1829, 1095-3795.

[27] G. Shirane, C. W. Chen, P. A. Flinn, and R. Nathans, Journal of Applied Physics **34**, 1044 (1963), ISSN 0021-8979, 1089-7550.

[28] G. Shirane, R. Nathans, and C. W. Chen, Physical Review **134**, A1547 (1964), ISSN 0031-899X.

[29] L. Zsoldos, physica status solidi (b) **20**, K25 (1967), ISSN 03701972, 15213951.

[30] A. I. Zakharov, A. M. Kadomtseva, R. Z. Levitin, and R. Z. Ponyatovskii, Soviet Physics JETP **19**, 1348 (1964).

[31] R. Medapalli, G. Li, S. K. K. Patel, R. V. Mikhaylovskiy, Th. Rasing, A. V. Kimel, and E. E. Fullerton, Applied Physics Letters **117**, 142406 (2020), ISSN 0003-6951, 1077-3118.

[32] R. Fan, C. J. Kinane, T. R. Charlton, R. Dorner, M. Ali, M. A. de Vries, R. M. D. Brydson, C. H. Marrows, B. J. Hickey, D. A. Arena, et al., Physical Review B **82**, 184418 (2010), ISSN 1098-0121, 1550-235X.

[33] S. Maat, J.-U. Thiele, and E. E. Fullerton, Physical Review B **72**, 214432 (2005), ISSN 1098-0121, 1550-235X.

[34] S. Kouvel and C. C. Hartelius, Journal of Applied Physics **33**, 1343 (1962).

[35] A. M. Chirkova, K. P. Skokov, Y. Skourski, F. Scheibel, A. Y. Karpenkov, A. S. Volegov, N. V. Baranov, K. Nielsch, L. Schultz, K.-H. Müller, et al., Physical Review Materials **5**, 064412 (2021), ISSN 2475-9953.

[36] Y. Ohtani and I. Hatakeyama, Journal of Magnetism and Magnetic Materials **131**, 339 (1994), ISSN 0304-8853.

[37] I. Suzuki, T. Koike, M. Itoh, T. Taniyama, and T. Sato, Journal of Applied Physics **105**, 07E501 (2009), ISSN 0021-8979.

[38] R. B. Flippen and F. J. Darnell, Journal of Applied Physics **34**, 1094 (1963), ISSN 0021-8979, 1089-7550.

[39] N. V. Baranov and E. A. Barabanova, Journal of Alloys and Compounds **219**, 139 (1995), ISSN 0925-8388.

[40] R. Barua, I. McDonald, F. Jiménez-Villacorta, D. Heiman, and L. H. Lewis, Journal of Alloys and Compounds **689**, 1044 (2016), ISSN 0925-8388.

[41] G. C. Han, J. J. Qiu, Q. J. Yap, P. Luo, D. E. Laughlin, J. G. Zhu, T. Kanbe, and T. Shige, Journal of Applied Physics **113**, 17C107 (2013), ISSN 0021-8979, 1089-7550.

[42] A. K. Zvezdin, in *Handbook of Magnetic Materials* (Elsevier, 1995), vol. 9, pp. 405–543.

[43] I. A. Dolgikh, T. G. H. Blank, A. G. Buzdakov, G. Li, K. H. Prabhakara, S. K. K. Patel, R. Medapalli, E. E. Fullerton, O. V. Koplak, J. H. Mentink, et al., *Ultrafast Emergence of Ferromagnetism in Antiferromagnetic FeRh in High Magnetic Fields* (2023), 2202.03931.

[44] S. B. Palmer, P. Dentschuk, and D. Melville, physica status solidi (a) **32**, 503 (1975), ISSN 1521-396X.

[45] C. Bordel, J. Juraszek, D. W. Cooke, C. Baldasseroni, S. Mankovsky, J. Minár, H. Ebert, S. Moyerman, E. E. Fullerton, and F. Hellman, Physical Review Letters **109**, 117201 (2012), ISSN 0031-9007, 1079-7114.

[46] D. Odkhuu, Physical Review B **93**, 064412 (2016), ISSN 2469-9950, 2469-9969.

[47] E. Mancini, F. Pressacco, M. Haertinger, E. E. Fullerton, T. Suzuki, G. Woltersdorf, and C. H. Back, Journal of Physics D: Applied Physics **46**, 245302 (2013), ISSN 0022-3727.

[48] T. A. Ostler, C. Barton, T. Thomson, and G. Hrkac, Physical Review B **95**, 064415 (2017), ISSN 2469-9950, 2469-9969.

[49] B. T. Thole, P. Carra, F. Sette, and G. van der Laan, Physical Review Letters **68**, 1943 (1992).

[50] P. Carra, B. T. Thole, M. Altarelli, and X. Wang, Physical Review Letters **70**, 694 (1993), ISSN 0031-9007.

[51] V. M. T. S. Barthem, A. Rogalev, F. Wilhelm, M. M. Sant'Anna, S. L. A. Mello, Y. Zhang, P. Bayle-Guillemaud, and D. Givord, Physical Review Letters **109**, 197204 (2012).

[52] J. Vogel, A. Fontaine, V. Cros, F. Petroff, J.-P. Kappler, G. Krill, A. Rogalev, and J. Goulon, Physical Review B **55**, 3663 (1997).

[53] C. Stamm, J.-U. Thiele, T. Kachel, I. Radu, P. Ramm, M. Kosuth, J. Minár, H. Ebert, H. A. Dürr, W. Eberhardt, et al., Physical Review B **77**, 184401 (2008).

[54] M. Wilke, G. M. Partzsch, R. Bernhardt, and D. Lattard, Chemical Geology **213**, 71 (2004), ISSN 0009-2541.

[55] A. Smekhova, D. Ciuculescu, P. Lecante, F. Wilhelm, C. Amiens, A. Rogalev, and B. Chaudret, IEEE Transactions on Magnetics **44**, 2776 (2008), ISSN 1941-0069.

[56] F. E. Hoare and J. C. Walling, Proceedings of the Physical Society. Section B **64**, 337 (1951), ISSN 0370-1301.

[57] A. Rogalev and F. Wilhelm, The Physics of Metals and Metallography **116**, 1285 (2015), ISSN 1555-6190.

[58] A. G. Buzdakov, I. A. Dolgikh, K. A. Zvezdin, A. K. Zvezdin, K. Rubi, U. Zeitler, P. C. M. Christianen, Th. Rasing, S. K. K. Patel, R. Medapalli, et al., Physical Review B **108**, 184420 (2023).

[59] B. Koopmans, M. van Kampen, J. T. Kohlhepp, and W. J. M. de Jonge, Physical Review Letters **85**, 844 (2000), ISSN 0031-9007, 1079-7114.

[60] J. Becker, A. Tsukamoto, A. Kirilyuk, J. C. Maan, Th. Rasing, P. C. M. Christianen, and A. V. Kimel, Physical Review Letters **118**, 117203 (2017), ISSN 0031-9007, 1079-7114.

[61] A. M. Stoffel, Journal of Applied Physics **40**, 1238 (1969), ISSN 0021-8979, 1089-7550.

[62] A. T. W. Kempen, F. Sommer, and E. J. Mittemeijer, Journal of Materials Science **37**, 1321 (2002), ISSN 1573-4803.

[63] J. A. Ricodeau and D. Melville, Journal of Physics F: Metal Physics **2**, 337 (1972), ISSN 0305-4608.

[64] F. Quirin, M. Vattilana, U. Shymanovich, A.-E. El-Kamhawy, A. Tarasevitch, J. Hohlfeld, D. von der Linde, and K. Sokolowski-Tinten, Physical Review B **85**, 020103 (2012), ISSN 1098-0121, 1550-235X.

[65] C. Dornes, Y. Acremann, M. Savoini, M. Kubli, M. J. Neugebauer, E. Abreu, L. Huber, G. Lantz, C. A. F. Vaz, H. Lemke, et al., Nature **565**, 209 (2019), ISSN 0028-0836, 1476-4687.

[66] S. R. Tauchert, M. Volkov, D. Ehberger, D. Kazenwadel, M. Evers, H. Lange, A. Donges, A. Book, W. Kreuzpaintner, U. Nowak, et al., Nature **602**, 73 (2022), ISSN 1476-4687.

[67] P. M. Oppeneer and A. Liebsch, Journal of Physics: Condensed Matter **16**, 5519 (2004), ISSN 0953-8984.

[68] A. V. Andreev, S. Yasin, Y. Skourski, A. A. Zvyagin, S. Zherlitsyn, and J. Wosnitza, Physical Review B **87**, 214409 (2013), ISSN 1098-0121, 1550-235X.

Chapter 5

Ultrafast dynamics of the antiferromagnetic to ferromagnetic phase transition in strained FeRh films

We report that strain significantly affects the laser-induced dynamics of the antiferromagnetic (AFM) to ferromagnetic (FM) phase transition in a 40 nm thick FeRh film at 100 K and in applied magnetic fields up to 30 T. This transition evolves via a nucleation-growth pathway and is monitored by femtosecond magneto-optical Kerr effect (MOKE) and reflectivity contrast measurements. We found that strain does not alter the speed of the nucleation of the FM domains in an applied magnetic field above 5 T, maintaining a characteristic time of approximately 3 ps. The volume fraction of the FM phase (both of the nuclei and the domains) is reduced (enhanced), under compressive (tensile) strain, which we attribute to the modification of the critical field and temperature of the phase transition by strain. Both tensile and compressive strain lead to a delay in the built-up of the MOKE signal, which is attributed to the presence of FM domains, stabilized by defects in the strained layers, exhibiting a characteristic negative demagnetization MOKE signal in addition to the magnetic response of the nucleation-growth of the FM domains. Qualitatively, no effect of strain on the growth speed of the ferromagnetic phase was seen. Tensile strain resulted in the appearance of latency in the built-up of the FM phase at low fields, indicative of a collinear antiferromagnetic initial state, in agreement with an enhanced spin-flop field under tensile strain. Finally, compressively strained FeRh layers showed damped oscillatory behaviour on short timescales, associated with the AFM-to-FM phase transition.

5.1 Introduction

The understanding of the magneto-structural phase transition in FeRh from a low temperature antiferromagnetic (AFM) phase to a high temperature ferromagnetic (FM) phase remains an intriguing research topic. In the previous chapter, we reported that the magnetic and lattice systems are so closely interconnected that their mutual interaction dominates the dynamics of the phase transition. Specifically, the characteristic time for the nucleation of the magnetization in the FM phase is limited by the timescale of the structural changes. It is, therefore, interesting to investigate whether the timescale of the emergence of the FM phase can be modified by structural means, for example by varying the degree of strain in the FeRh layer.

Numerous studies have been performed, both experimentally and theoretically, to investigate the effect of strain in FeRh on the transition temperature T_C of the AFM-FM phase transition [1–8]. Research from [2] indicates that tensile and compressive strain respectively reduces and increases T_C, because the change in the interatomic distance either promotes or restricts the lattice expansion. This effect is schematically shown in Figure 5.1 by the blue (tensile strain) and green (compressive strain) arrows. This leads to a reduced (enhanced) T_C with tensile (compressive) strain in the absence of an applied magnetic field and a reduced (enhanced) critical magnetic field H_C for tensile (compressive) strain in the presence of an external magnetic field.

Applying strain to FeRh not only affects the lattice parameter by altering its size but also influences the exchange interaction. Early theories, like the one proposed by Kittel [9], considered the exchange magnetoelastic energy and suggested that the sign of this term should change at the phase transition. The order parameter here is the lattice parameter, leading to the inversion of the magnetoelastic energy at some critical value. This theory is indeed able to reproduce the observed phase transition, although some experimental investigations have rejected it [10]. Furthermore, high-pressure experiments have revealed the existence of a triple point where the FM phase disappears, which underlines the magnetoelastic origin of the transition [11].

Additionally, strain increases the crystal anisotropy in the film, compounded by the Poison effect, which further alters the lattice parameters. Given the connection between the lattice parameter and the magnetic order in FeRh, strain results in distortions of the lattice [4] and an increased magnetocrystalline anisotropy [6]. This becomes crucial for the spin-flop transition, as it defines the critical field at which the spin alignment in the antiferromagnetic phase is no longer collinear [12]: $H_{SF} \sim \sqrt{(H_{an} H_{ex})}$. Here, H_{an} represents the effective field of the uniaxial magnetic anisotropy, and H_{ex} signifies the effective field of the inter-sublattice exchange interaction, both of which are sensitive to the lattice parameter. At this critical field, the spin reorientation process changes as shown in [13] and our pre-

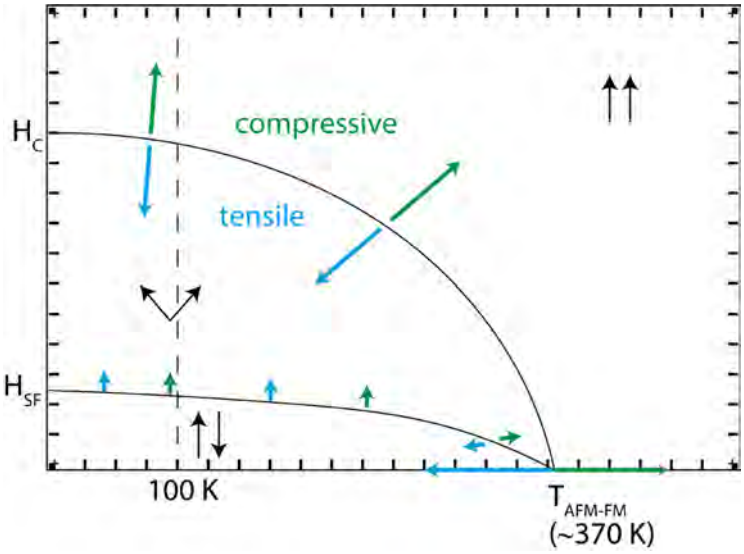

Figure 5.1: Qualitative sketch of the modification of the (H,T) phase diagram under the influence of uniaxial strain. The blue and green arrows schematically show the influence of tensile and compressive strain on the phase AFM-FM phase transition (T_C, H_C) and spin flop transition (H_{SF})

vious findings (Chapter 4), where we observed a latency between the laser excitation and the onset of spin reorientation in the collinear phase. This latency disappears above the spin-flop transition. As schematically shown in Figure 5.1 we expect that H_{SF} increases for both an applied tensile and compressive strain. So, the application of any type of strain should allow us to observe the latency over a wider magnetic field range. The spin-flop transition has not been observed for FeRh, but the effect of strain on the magnetocrystalline anisotropy was pointed out for Cr_2O_3, for which the spin-flop transition was induced by strain [14]. In antiferromagnetic NiO, the application of strain provoked the change in the anisotropy from easy-axis to easy-plane and led to the increase of the coercitivity [15]. Thus, strain can indeed influence the size and direction of the anisotropy in antiferromagnets.

Our prior work [16] revealed that the characteristic time of the AFM to FM phase transition in FeRh saturates in an external magnetic field to a 2-3 ps timescale. This current study aims to determine whether the limiting speed is modified in a strained FeRh film and whether the volume fraction of the emerging FM domains is affected by strain.

5.2 Experimental conditions

5.2.1 Sample

For our study of the effect of strain on the dynamics of the AFM-FM phase transition, we used the same sample as in Chapter 4. This 40 nm thick FeRh film was grown on a MgO single crystal through magnetron sputtering. The FeRh film was capped with a 5 nm layer of Pt, to ensure the stability of the sample. The sample was characterized by X-ray reflectometry and X-ray diffraction [17]. The orientation of the $Fe_{50}Rh_{50}$ crystal was found to be (001). The magnetization of this particular sample was determined by means of SQUID and MOKE, the results of which have been reported in Chapter 4.

5.2.2 Setup

The experiments were performed in the High Field Magnet Laboratory in Nijmegen (HFML-FELIX). The setup and the procedure that we used have been described in detail in Chapter 2. Briefly, the ultrafast dynamics was measured using a pump-probe technique. The energy provided by the pump pulse, at a wavelength of 800 nm (1.55 eV), was kept constant at 4.1 mJ/cm^2 throughout the whole set of measurements. As described in [16] this amount of pump energy was estimated to heat the irradiated area of the FeRh film for about 230 K. To probe the changes in the magnetic state of the sample a beam at a different wavelength, 660 nm (1.9 eV), was used obtained from an optical parametric amplifier (OPA). The signal was detected using a balanced photodetector (Chapter 2). It allowed us to measure simultaneously the polar MOKE signal and the change in the reflectivity of the sample. The last signal is considered to contain contributions to the dynamics of both electrons and the lattice [18].

The samples investigated were cooled down to 100 K in a cryostat filled with liquid nitrogen and inserted in a Florida-Bitter magnet that can produce magnetic fields along the normal to the sample up to 37.5 T. This temperature was chosen following the diagram schematically shown in Fig. 5.1, because at 100 K FeRh is supposed to be fully antiferromagnetic up to 25-30 T, allowing us to observe the AFM-to-FM transition up to high applied magnetic fields. Moreover, as will become clear in the following, at 100 K we are able to separate the dynamics of the phase nucleation from that of the phase growth and alignment.

5.2.3 Application of strain

For the application of strain, we used the mechanical holder described in Chapter 2. In this holder, the sample is clamped between two walls. Rotation of the screw moves one of the walls, leading to an external force (stress)

on the sample and resulting in the development of strain in the film. The rotation direction determines the type of strain (tensile or compressive), whereas the rotation angle determines the change in the distance between the clamp walls and therefore the strain level. Leveraging the elastic coefficients of MgO (as outlined in [19]) and brass (105 GPa), corresponding to the screw and wall respectively, we estimated that our first set of measurements induced a tensile strain of 0.7%, while the second set reached 1.4%. To safeguard the integrity of the sample during compression, we limited the strain in that experiment to 0.7%. As a result, we have been able to obtain data from these three strained FeRh films (-0.7%, 0.7%, and 1.4%) and compared it to the unstrained sample, which was glued to the metal holder at its side (nominally 0% strain). It is important to note that also in this nominally unstrained layer, some degree of strain might exist. First of all, thin films grown on a substrate can develop an additional strain due to the mismatch between the crystallographic lattice parameter between the alloy and the substrate, as outlined in [1]. Furthermore, during sample mounting, for instance, by clamping or adhesive bonding on the holder, some strain might appear, in particular when experiments take place at reduced temperatures. The differences in the thermal coefficients of the holder, substrate, and thin film can generate additional strains, potentially leading to shifts in the parameters of the phase transitions. Although these effects are estimated to be much smaller than those of the mechanically strained samples, care has to be taken in comparing the results of the ultrafast dynamics in different experimental runs and sample mountings.

5.3 Experimental results

In the following, we will present the experimental results of the different mechanically strained FeRh samples, relative to the traces of the nominally unstrained sample at the same temperature of 100 K and external magnetic fields. The traces of the unstrained sample will be indicated by black curves. We will show the transients in two panels, at short (up to 20 ps) and longer (up to 300 ps) timescales, the latter of which was measured immediately after each corresponding short-term measurement, but with bigger steps in the time delay between the pump and probe pulses.

5.3.1 Tensile strain

0.7% tensile strain

The blue (black) lines in Fig. 5.2 show the time-dependent MOKE signal of the 0.7% tensile strained (unstrained) sample at 100 K and for a number of magnetic field strengths. The reflectivity signal recorded at the same time is shown by the dotted curves. For fields below 30 T the MOKE signals of the two samples are clearly different at short time delays, with a slower rise of

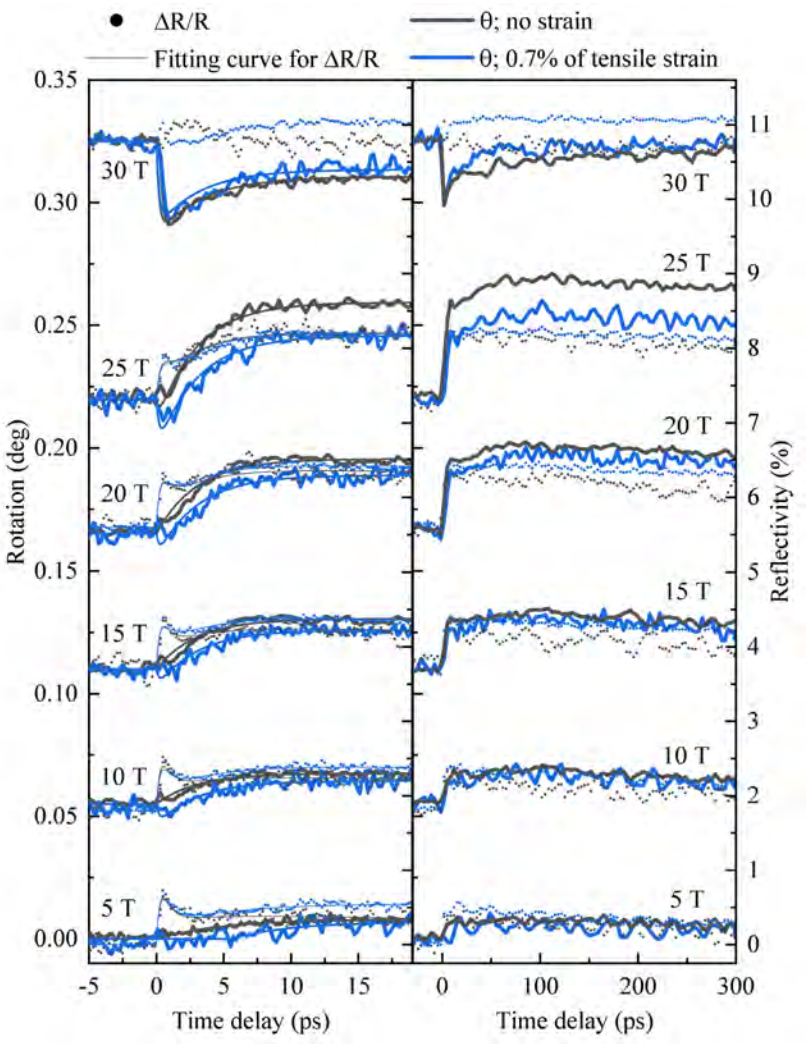

Figure 5.2: The laser-induced polar MOKE signals for 0.7% tensile strained (blue lines) and unstrained (black lines) FeRh films for external magnetic fields up to 30 T at temperature $T = 100$ K. The data were fitted with exponential decay functions, shown by the solid lines of the corresponding colour. The pump-induced reflectivity changes are indicated by the dotted lines, with the corresponding fitting curves as thin lines in blue (0.7% tensile strain) and black (no strain). For clarity, the data and fits at different fields are vertically offset.

the overall signal for the strained film, relative to the unstrained film. At 30 T, the MOKE signal changes sign and the two films show a similar MOKE response, indicative of the fact that at this field the FeRh film is in the FM phase. At longer timescales, the two samples exhibit comparable MOKE responses. The laser-induced changes in the reflectivity signal are quite similar for the two samples at all timescales. At 5 T the strained sample does not show a laser-induced MOKE signal during the first 5.6 ± 0.7 ps (latency), whereas the signal from the unstrained film rises immediately after pump-laser excitation. Remarkably, at 30 T, when FeRh is in the FM phase, for both samples the reflectivity does not show any changes at all as a function of pump-probe delay.

With increasing magnetic field the amplitudes of the signals for both samples increase, which is reasonable considering the fact that at higher fields FeRh is brought closer to the boundary of the AFM-FM phase transition. At higher fields, the MOKE transient of the 0.7% strained sample shows a slight initial drop, which is absent in the signal of the unstrained sample. This negative signal slightly increases when approaching the phase transition. Most of the MOKE and reflectivity signals built up occurs on a short timescale (< 10 ps), after which their amplitudes do not grow significantly further. The curves below 15 T already slightly relax in the 300 ps time window. The MOKE data obtained at 25 T (and to a lesser extent also the 20 T data) show some slow rise up to 100 ps. This slower signal is indicative of the growth and further alignment of FM domains, clearly distinctive from the fast nucleation of the FM domains in the first 10 ps after the heating of the pump pulse.

1.4% tensile strain

Fig. 5.3 shows the results of the 1.4% tensile strained FeRh thin film (red curves). Clearly, the differences in the response relative to the unstrained sample are much more pronounced than for the 0.7% tensile strained sample. Also for this sample, on short timescales, the response is delayed with respect to the unstrained sample (black curves). The latency at 5 T is still visible (3.0 ± 0.3 ps), but it decreased in comparison with the 0.7% tensile strained sample (5.6 ± 0.7 ps, see Fig. 5.2).

The MOKE signal shows an initial negative contribution immediately after laser excitation, for magnetic fields of 10 T and higher, which indicates a demagnetization contribution, which for the unstrained sample is only visible at 30 T. However, after this initial negative component, the MOKE signal rises quickly to above the signal of the unstrained film, already after 5-15 ps. At 30 T the MOKE transient of the strained sample becomes more negative. At lower magnetic fields, the reflectivity of the strained sample is significantly higher than the one without strain. And also in this case the reflectivity signal at 30 T does not show any time-dependence, indicating that in the FM phase, the reflectivity is insensitive to the effects of the

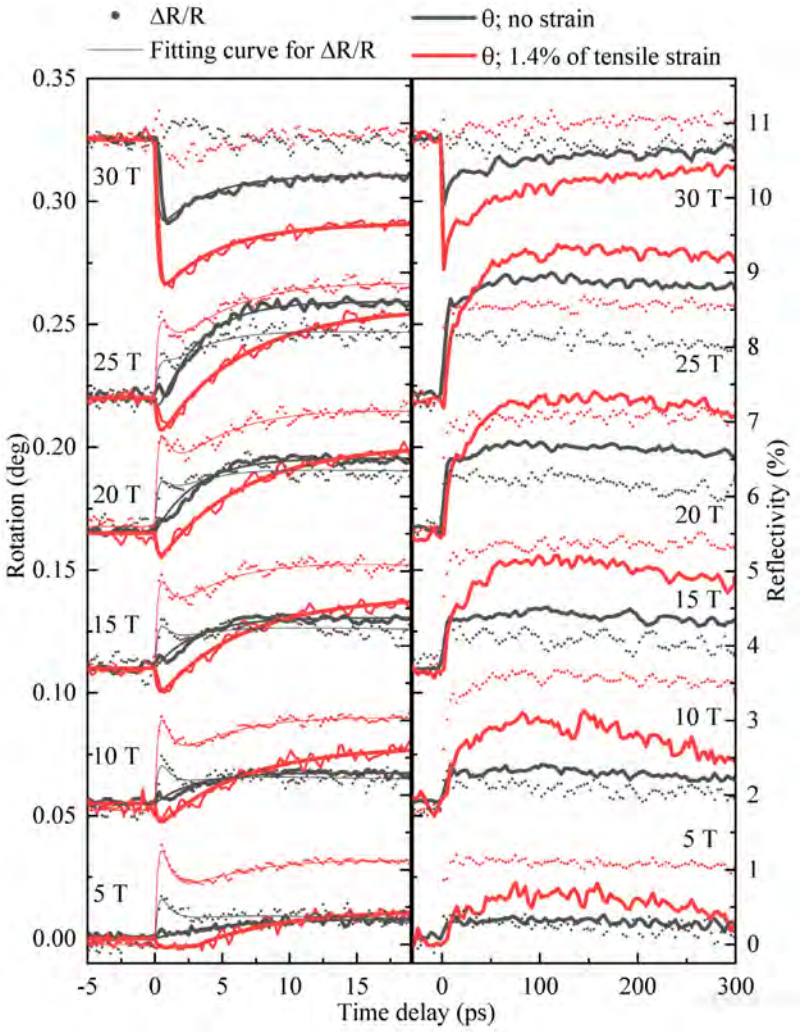

Figure 5.3: The laser-induced polar MOKE signals for 1.4% tensile strained (red lines) and unstrained (black lines) FeRh films for external magnetic fields up to 30 T at temperature $T = 100$ K. The data were fitted with exponential decay functions, shown by the solid lines with the corresponding colour. The pump-induced reflectivity changes are indicated by the dotted lines, with the corresponding fitting as thin lines in red (1.4% tensile strain) and black (no strain). For clarity, the data and fits at different fields are vertically offset.

pump pulse heating.

The rise of the overall magnetization signal dynamics occurs on a much longer timescale and does not reach saturation anymore at 20 ps. The fast rise of the MOKE signal (domain nucleation) is still present, but clearly, a slower growth is visible at long timescales at all magnetic field strengths (right panel Fig. 5.3). The growth is saturating before 100 ps and does not accelerate in an external magnetic field. At 5 T the signal almost relaxes within 300 ps and at higher magnetic fields the relaxation time increases until at 25 T - 30 T a stable plateau is observed within the measured timescale.

5.3.2 Compressive strain

Fig. 5.4 displays the results for the compressively strained FeRh film, which are remarkably different from those of the tensile strained and unstrained samples. We observe an initial negative step in the MOKE transient, which does not depend on the magnetic field strength. With increasing magnetic field, and approaching the phase transition, the signal exhibits a heavily damped oscillation in addition to the regular exponential rise. The amplitudes of the exponential rise and oscillation get more pronounced with increasing field, and are most prominent at 20 T and 25 T. Generally, for this compressively strained sample, a positive MOKE signal starts to be observed above 15 T. All of those features are not visible in the reflectivity transients, which for the compressively strained sample are roughly the same as for the unstrained and 0.7% tensile strained samples. When comparing the magnetic response from the unstrained and compressed sample on the longer timescale, the effect of compression becomes especially significant. At 15 T, for example, in the unstrained film, a stabilization of the positive MOKE signal was observed. In contrast, under the same conditions, no laser-induced changes in the MOKE signal of the compressed sample were observed. Generally speaking, the application of compressive strain resulted in an opposite effect in the MOKE signal relative to that of tensile strain and a substantially decreased laser-induced MOKE amplitude. Despite the low signal at 20 T - 25 T, relaxation does not occur within 300 ps.

5.4 Fitting procedures and results

In order to develop a more detailed understanding of the onset of the FM phase after ultrafast laser heating we have fitted the MOKE and reflectivity traces in the first 20 ps after the laser pulse (left panels in Fig. 5.2, 5.3 and 5.4). We did not attempt to fit the full curves at longer time delays, although as described below in some cases it was difficult to disentangle the first nucleation stage of the process from the subsequent domain

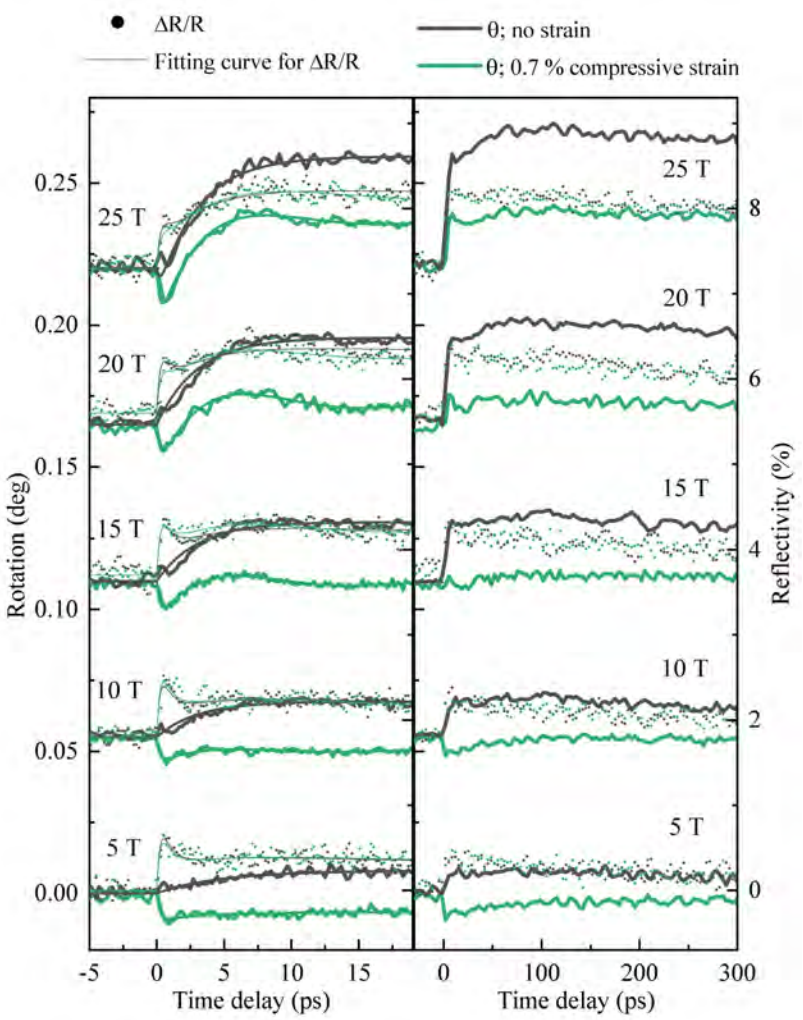

Figure 5.4: The laser-induced polar MOKE signals for 0.7% compressively strained (green lines) and unstrained (black lines) FeRh films for external magnetic fields up to 30 T at temperature $T = 100$ K. The data were fitted with exponential decay functions and damped oscillation, shown by the solid lines with corresponding colour. The pump-induced reflectivity changes are indicated by the dotted lines, with the corresponding fitting as thin lines in green (0.7% compressive strain) and black (no strain). For clarity, the data and fits at different magnetic fields are vertically offset.

growth stage. Given the profound differences in the ultrafast response of the samples with the different levels of strain, we have used different fitting functions for each type of sample.

5.4.1 Fitting function for the unstrained sample

To obtain information about the characteristic time of the laser-induced phase transition in the lattice and spin systems we fitted the transients with the following exponential functions:

$$\begin{aligned} \frac{\Delta R}{R}(t) &= A_{\mathrm{L}} \cdot (1 - \mathrm{e}^{-t/\tau_{\mathrm{L}}}) \\ \theta(t) &= B_{\mathrm{M}} \cdot (1 - \mathrm{e}^{-t/\tau_{\mathrm{M}}}), \end{aligned} \tag{5.1}$$

where A_{L} and B_{M} are the amplitudes of the laser-induced reflectivity and MOKE signals respectively; τ_{L} and τ_{M} are the corresponding rise times. As the polarization rotation signals are subject to significant amplitude changes we first normalized all the transients and fitted only the rise times.

In addition to the exponential rise, the reflectivity signal also contains a fast response from the electronic system, which we fitted by [20]:

$$\begin{aligned} \frac{\Delta R_{\mathrm{el}}}{R}(t) = A_{\mathrm{e1}} \cdot (1 - \mathrm{e}^{-t/\tau_{\mathrm{e1}}}) \cdot \mathrm{e}^{-t/\tau_{\mathrm{e2}}} + \\ A_{\mathrm{e2}} \cdot (1 - \mathrm{e}^{-t/\tau_{\mathrm{e2}}}) \cdot \alpha \cdot \mathrm{e}^{-t/\tau_{\mathrm{dif}}}. \end{aligned} \tag{5.2}$$

This formula represents the combination of several exponential functions. The component with amplitude A_{e1} and time constant τ_{e1} describes the effect on the reflectivity of the laser-induced heating of the electron system, leading to the presence of hot electrons. The component with amplitude A_{e2} and time constant τ_{e2} describes the cooling of the electron system due to the relaxation of heat to the phonon system. The cooling starts immediately after laser excitation so it also modifies the first term. The component with characteristic time τ_{dif} is due to the thermal diffusion on longer timescales, which affects the second term describing the cooling of the electron system. In practice we determined A_{e1}, τ_{e1}, A_{e2}, τ_{e2} and τ_{dif} for the data at the lowest external magnetic field and a temperature of 4 K. For those conditions the signal from the phase transition is negligible. This resulted in the following values: $A_{\mathrm{e1}} = 1.3 \pm 0.6\%$, $A_{\mathrm{e2}} = 0.26 \pm 0.01\%$, $\tau_{\mathrm{e1}} = 0.42 \pm 0.25$ ps, $\tau_{\mathrm{e2}} = 0.68 \pm 0.16$ ps and $\tau_{\mathrm{dif}} = 59 \pm 10$ ps, approximately consistent with previously published time constants for fast processes during the laser-excitation [20–22]. Subsequently, these parameters were kept fixed for all other measured transients, where the factor α was used as a scaling factor to accommodate the changes in the reflectivity response of the electronic system with varying experimental conditions.

5.4.2 Fitting function for the tensile strained samples

For the tensile strained samples, the observed MOKE transients were found to be more complex than for the unstrained FeRh film; under certain conditions, a negative MOKE signal was observed at short time delays, as well as a latency at low temperatures. Therefore, to describe the MOKE signal we included, in addition to the exponential rise (equation 5.1), a negative demagnetization part for the data above 5 T in the form of double exponential decay. To account for the latency in the MOKE signal at 5 T, we added a delay τ_o, as was described in the previous Chapter 4.

The latency delay and the negative signal were not present in the reflectivity signal. So the expression for $\frac{\Delta R_{el}}{R}(t)$ (equation 5.2) remained the same, whereas we used the following expression for $\theta(t)$:

$$\theta(t) = B_M \cdot (1 - e^{-(t-\tau_o)/\tau_M}) - D \cdot (1 - e^{-t/\tau_D}) + D_{relax} \cdot (1 - e^{-t/\tau_{D_{relax}}}). \quad (5.3)$$

The first term is the regular exponential rise due to the nucleation of the FM phase, but with a delay τ_o due to the latency. The second term (rise with amplitude D and time constant τ_D) and the third term (relaxation with amplitude D_{relax} and time constant τ_{Drelax}) are describing a demagnetization process. This part of the signal was fitted on the signal at 30 T, when FeRh is in the ferromagnetic phase and when the first term is absent. The time constants found $\tau_D = 0.210 \pm 0.015$ ps and $\tau_{Drelax} = 3.47 \pm 0.20$ ps, agree well with the expected values for an iron-based ferromagnet [20]. These time constants were then fixed during the fitting of all other curves. To reduce the number of free parameters, we fixed the ratio D/D_{relax} to 3.34, in the fitting process.

At the higher value of tensile strain (1.4%), the signal did not saturate within 20 ps (see right panel Fig. 5.3). This particular response introduced a challenge in the discrimination between the first-stage (nucleation of the FM domains) and the second-stage (subsequent growth, alignment and relaxation of the FM domains) processes. In the discussion of the fitting results below, we will describe what are the consequences for the fitted parameters of this feature of the data.

5.4.3 Fitting function for the compressively strained sample

The ultrafast transients for the FeRh films under compression revealed a characteristic oscillatory behaviour (Fig. 5.5), quite distinct in appearance from the responses of the tensile strained and unstrained films. As a result, we had to include an additional, damped, harmonic oscillation term in the fitting functions for both the reflectivity and MOKE signals:

$$\theta_F(t) = C_M \cdot \cos(2\pi F t - \pi/2) e^{-\gamma t}, \quad (5.4)$$

with C_M the amplitude of the wave in MOKE, F is the frequency of the oscillation and γ is the decay rate of the damped oscillator. The oscillations were most clearly present in the MOKE measurement, but under some circumstances, the oscillations were also seen in the laser-induced reflectivity signal, most clearly at 15 T and higher. For these circumstances, we included the oscillatory term with the same frequency and damping parameter and free amplitude C_L in the fitting of the reflectivity.

The value of the frequency was determined for those transients which showed the most pronounced oscillations. The oscillatory behaviour appeared to be highly damped and could be described by using $\gamma = 0.1$ ps^{-1}, independent of the magnetic field. The frequency was found to be roughly independent of the magnetic field strength, resulting in an average value of $F = 0.046 \pm 0.003$ THz. Fixing F and γ left the amplitude as the only free fitting parameter to describe the oscillation of the signal, which was crucial in order to distinguish between the gradual magnetization growth and the nucleation. A typical resulting fitting curve is plotted in Figure 5.5, together with the corresponding raw MOKE data. Although the total expression of the MOKE signal has several terms, using the fitting procedure as described we could fix quite some of the parameters. The demagnetization (purple curve, D and τ_D) and its relaxation (yellow curve, D_{relax}, τ_{Drelax}) were fitted on the signal at 30 T, which consists only of a negative demagnetization signal. This resulted in fixed time constants $\tau_D = 0.210 \pm 0.015$ ps and $\tau_{Drelax} = 3.47 \pm 0.20$ ps and one fitting parameter D with $D/D_{relax} = 3.34$. The oscillation was determined for those transients which showed the most pronounced oscillations, resulting in a fixed frequency $F = 0.046$ THz and damping $\gamma = 0.1$ ps^{-1}, leaving the amplitude of the oscillation as a free parameter. This way it was possible to obtain reasonable good fits of the total data (see the red curve in Fig. 5.5) with a consistent set of fitting parameters.

5.4.4 Results of the fitting

For the unstrained sample, the fitting of the MOKE data resulted in the τ_M values given by the open black points in Fig. 5.6(a). We see a gradual decrease of the rise time with increasing field strength, which indicates that the nucleation speeds up with the field until it saturates, as described in the previous chapter. However, the data point at 5 T has only a slightly larger value and a larger error bar due to the low amplitude of the MOKE signal under those conditions. So strictly speaking, within the experimental uncertainty of the fit procedure, τ_M is roughly constant as a function of the magnetic field. Averaging τ_M over the different field values gave a characteristic rise time of the magnetic signal as $\tau_M = 3.6 \pm 0.8$ ps. The error here represents the standard deviation of the averaging. Similarly, τ_L shows no field dependence within the experimental error, leading to an average value of $\tau_L = 2.8 \pm 0.5$ ps. Both time constants are comparable to

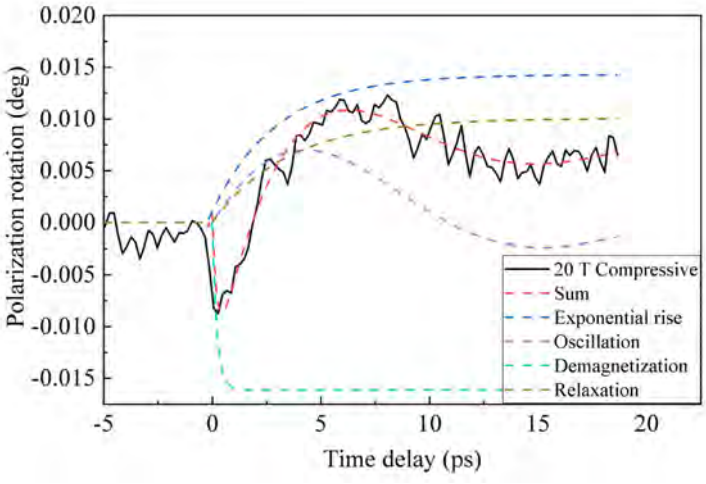

Figure 5.5: Illustration of the fitting for the MOKE signal (solid black line) of the compressively strained FeRh sample at 20 T and 100 K. Dashed lines represent the final fit (red) and its contributions: Exponential magnetization growth from eq. 5.1 (green); oscillatory part term from eq. 5.4 (blue); Demagnetization and its relaxation included in all strained data as in eq. 5.3 (purple and yellow).

those reported in the previous chapter.

Most remarkably, the τ_M values found for the samples with 0.7% tensile and compressive strain are similar to those for the unstrained sample, despite the profound delay of the built-up of the overall MOKE signal relative to the unstrained sample. Apparently, for these strain levels, the timescale of the nucleation of the FM domains at high magnetic fields does not depend on strain. In contrast, the fitted τ_M values for the 1.4% tensile strained sample shows a different behaviour. At 5 T τ_M of the 1.4% tensile strained sample is still the same as for the other samples, but with increasing magnetic field it increases towards much higher values. However, as described above, the MOKE signal does not reach saturation at 20 ps for this sample (Fig. 5.3) and continues to grow at longer time delays. This effect grows in importance with increasing magnetic field. As described in detail in the discussion section, for high magnetic fields it is not possible for this sample to discriminate between the first stage (nucleation of the FM domains) and the second stage (subsequent growth, alignment and relaxation of the FM domains) of the AFM to FM phase transition. Indeed, the fitting routine finds much longer rise times, increasing to 6-7 ps at high fields, to better describe the growth of the MOKE signal on all timescales, but which is not related to the pure τ_M anymore, that is introduced to describe the initial

increase of the magnetic signal due to FM domain nucleation.

In a next step of the fitting process, we focused on the relative amplitudes of the different terms in the signals. Here we note that, within the experimental error, τ_M is magnetic field independent, and τ_L is roughly constant for fields of 10 T and higher. So we fixed both characteristic times to 3 ps for the samples with strains -0.7%, 0% and +0.7%. The transients measured for high tensile strain were fitted with a characteristic times of 6.6 ps. We have carefully verified that this left the actual trends of the different amplitudes unchanged, but that it only resulted in a smoother behaviour of the amplitudes, because of the reduction in the number of free fitting parameters. The results of this fitting process are shown by the thick and thin solid lines in the left panels of Fig. 5.2, 5.3 and 5.4. In all cases the experimental curves could be properly described by a consistent set of fitting parameters, the results of which can be found in Figure 5.6 (c-f). The overall behaviour of the fitting parameters is remarkably similar for the unstrained sample and the 0.7% tensile and compressively strained samples. In contrast, the results for the 1.4% tensile strained sample clearly deviate from this behaviour. Although, the fitted curves reasonably describe the data on a 20 ps timescale (Fig. 5.3), our fitting procedure is flawed for this sample because the transients do not show saturation after 20 ps, but continue to grow. This does not only lead to enhanced values for τ_M (6.6 ± 0.5 ps), but also to values for the A_L and B_M amplitudes that cannot be compared to those of the other samples. In the following, we, therefore, disregard the fitting parameters A_L and B_M for the 1.4% tensile strained sample and we will come back to the results of this sample in the discussion section.

Like in our previous study, Chapter4, the amplitude in MOKE (Fig. 5.6c), increases with increasing magnetic field and this occurs for all samples. The actual value of B_M at each field depends on the strain level that is introduced in the system. In particular, with compressive strain the B_M values are the smallest at each field. The reflectivity signal appears to be sensitive to the magnetic phase as well, which leads to larger A_L values with increasing fields (Fig. 5.6(d)).

Fig. 5.6e shows the magnetic field dependence of the scaling parameter α describing the ultrafast response of the electronic system in the reflectivity. α decreases with increasing magnetic field strength for all samples, until at the highest magnetic fields (in the FM phase) no ultrafast electronic response is seen, leading to flat reflectivity curves at 30 T. α does not depend on the strain level of the samples, except for the 1.4% tensile strained film, which exhibits considerably higher α values.

The amplitudes of the oscillation component in the response of the compressively strained FeRh film grows with increasing magnetic field in both reflectivity, C_L and MOKE C_M (Fig. 5.6(f)). At high fields the oscillation component in the MOKE signal even makes up half of the signal (left panel

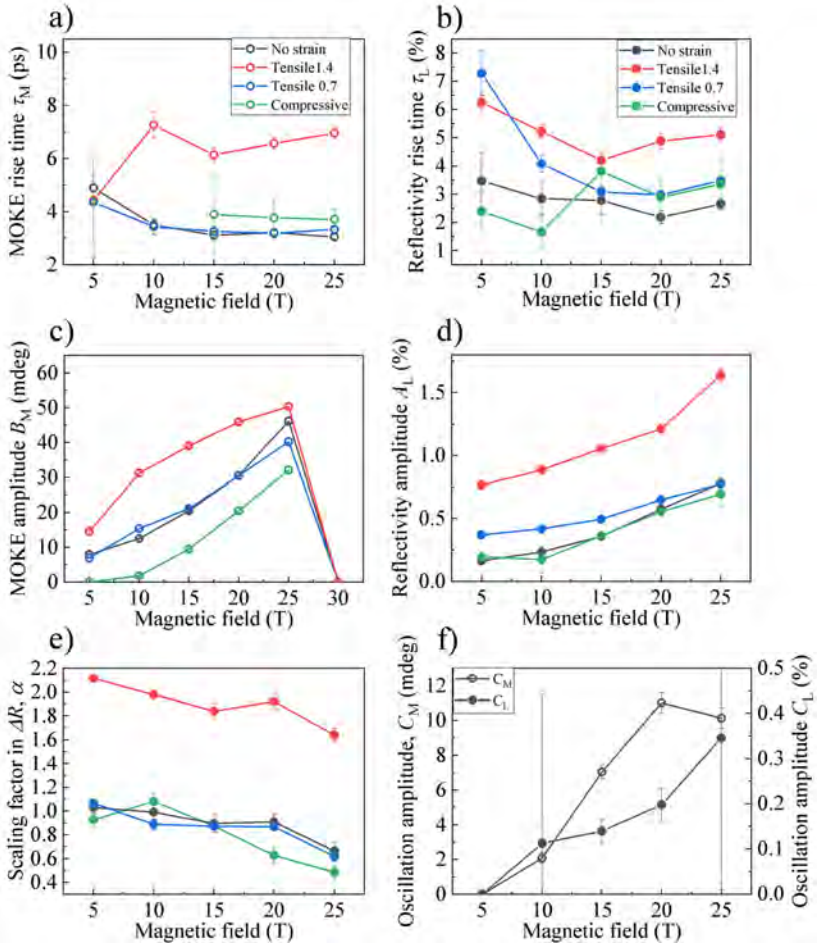

Figure 5.6: Results of fitting the MOKE and reflectivity data from Figs. 5.2, 5.3 and 5.4 for the different samples. Exponential rise times τ_M in MOKE (a) and τ_L in Reflectivity (b) from Eq. 5.1. The dependence of the amplitudes B_M (c) and A_L (d) on the external magnetic field. (e) Field dependence of the scaling factor α of the fast electronic contribution in the reflectivity from Eq. 5.2; (f) The amplitudes of the oscillations in the compressively strained sample from Eq. 5.4 present in the MOKE signal (C_M) and in the reflectivity (C_L).

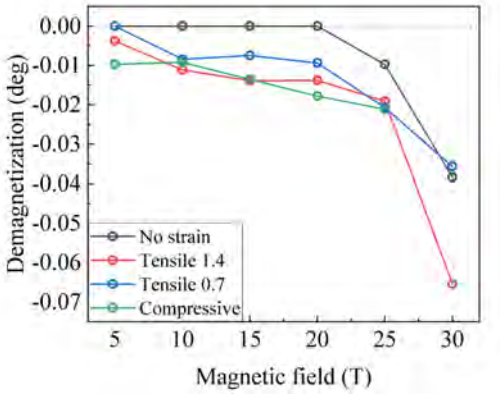

Figure 5.7: The amplitude D of the demagnetization contribution to the MOKE response of the different samples as a function of magnetic field strength, obtained by fitting the data with Eq. 5.3. The ratio between D and D_{relax} was kept fixed at 3.34.

Fig. 5.3). The oscillation component is less visible in the reflectivity signal, because most of this signal consists of the ultrafast electronic response.

All samples, and in particular the strained films, exhibit a negative contribution to the overall signal, which is accounted for by the demagnetization term in equation 5.3. The amplitudes of this term for the different samples are shown in Fig. 5.7. At low fields D is zero for the unstrained sample, until at 30 T the sample enters the FM phase and the MOKE signal only consists of the negative demagnetization part. For the strained films, we observed a finite D value for a certain field range, until also for these samples the signal is entirely negative in the FM phase at 30 T.

5.5 Discussion

We will interpret our results in terms of the well established picture of the AFM-to-FM phase evolution after non-equilibrium laser excitation, which involves the nucleation of the FM phase, and its subsequent growth and alignment as a function of the time delay between the pump and the probe pulses [23, 24]. This process is schematically drawn in Fig. 5.8. For negative time delays (panel a) the probe pulse arrives at the sample in the AFM phase and in which some FM domains might be present. When the pump pulse arrives it heats the electrons, and eventually the lattice, in the film, changes the magnetic state of the FM domains already present (panel b) and it drives the nucleation of new FM domains (panel c). With increasing time delay, the FM domains grow and align along the field direction

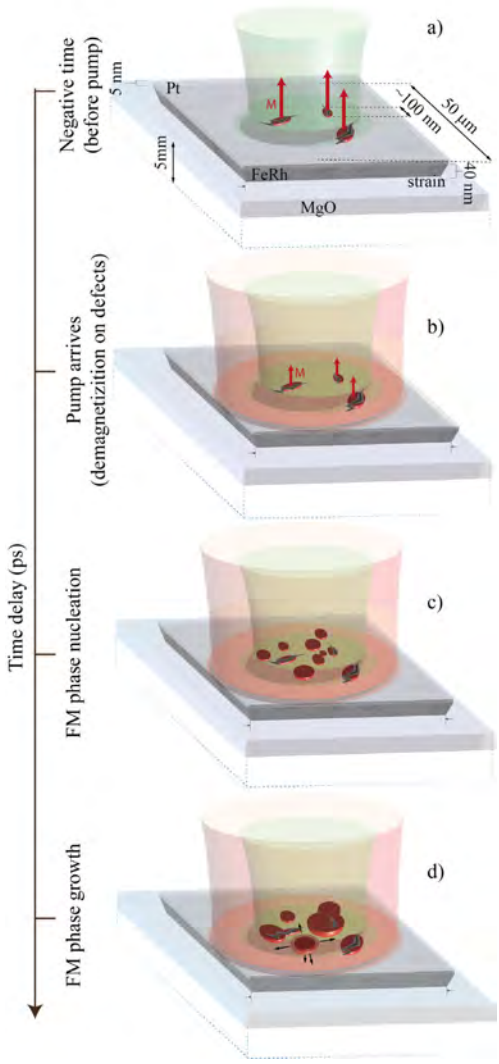

Figure 5.8: Schematic overview of the pump-probe experiment detecting the laser induced nucleation and growth of the FM phase starting from an AFM phase. See text for a detailed description of the different stages of the process.

(panel d), until at a much longer timescale they relax back to the equilibrium AFM phase (not shown). We assume that our technique is fully stroboscopic, such that the sample fully relaxes back to the AFM phase (with potentially some FM domains) in between the consecutive laser pump pulses, allowing us to repeatedly measure the nucleation and growth of FM domains from the AFM phase after each exciting pulse. The diameter of the probe beam (approximately 30 μm) is significantly larger than the typical domain size of the order of 100 nm, as reported in domain imaging experiments [25–29]. The signal measured by the probe beam therefore corresponds to the response of several domains simultaneously. The diameter of the pump beam (approximately 50 μm) is larger than that of the probe. The optical pulses penetrate up to 10 nm into the FeRh film after propagating through the capping lay, exciting the phase near the sample surface (Figure 5.8).

5.5.1 Nucleation and growth

Let us first concentrate on the nucleation step of the phase transition. It is completed in roughly 10 ps and its characteristic timescale τ_{M} equals approximately 3 ps for all samples (Fig. 5.6(a)). This nucleation phase is also observable in the reflectivity difference signal (Fig. 5.6(b)). At the lowest magnetic fields used, τ_{M} is slightly higher than at high field, which is consistent with the conclusion of the previous chapter, that the nucleation phase accelerates with increasing field until it saturates at higher field strengths. However, this acceleration is relatively small and falls within the experimental error of our experiment. Most importantly, our results show that the speed of the nucleation phase does not depend on the degree of strain in the FeRh film.

This finding seems to be counter-intuitive as the strain state changes the speed of sound. The speed of sound is usually defined from Young's modulus E and density ρ: $v_s = \sqrt{E/\rho}$. Strain can modify both the elastic modulus and the density, however, it is not clear what change it induces in FeRh. It was shown that the sound velocity follows the expansion of the lattice in FeRh [30]. So strain might be expected to change the nucleation time when it is limited by the speed of the lattice expansion. However, this is not happening or the changes are below our experimental resolution. It means that the speed of sound doesn't play a role here, but rather the time needed for the heat redistribution to the lattice system. The last one does not depend on either the magnetic field or the strain state and is defined by the electron-phonon coupling time. The following timescale of the domain growth is afterwards defined by the thermal conduction of the alloy.

The amplitudes of the MOKE and reflectivity components that are associated with the nucleation and growth of the phase increase with the magnetic field strength for all samples (Fig. 5.6(c,d)). We interpret these amplitudes as measures of the volume fraction of the FM phase, i.e. the

sum of the magnetization of the FM domains within the probe beam. So the volume fraction of the nucleating domains becomes higher when the initial conditions are closer to the AFM-to-FM phase transition border, i.e. with increasing external magnetic field strength (Fig. 5.1). It is remarkable though that the value of these amplitudes, and in particular B_{M}, strongly depends on the strain inside the FeRh film. For instance, for the compressively strained sample, B_{M} is the lowest for all samples at each field and by a significant amount. This finding aligns with earlier equilibrium results and simulations that demonstrate that compressive strain hampers the phase transition and pushes up the FM phase boundary (H_{C}, T_{C}), see green arrows in Fig. 5.1 [2, 3, 7]. Following this reasoning, we expect that, since under tensile strain the phase boundary shifts to lower fields (blue arrows in Fig. 5.1), the volume fraction of the FM domains increases with increasing tensile strain. Surprisingly, this effect is not so much visible during the nucleation phase in our experiments, but rather in the growth and alignment of the FM phase at longer pump-probe delay times. This effect is not included in our fitting functions, but it is clearly visible in the raw experimental data (right panels of Figs. 5.2, 5.3 and 5.4). For the compressively strained film (Fig. 5.4) the MOKE amplitude is low and saturates within 20 ps, as described above. For the unstrained and 0.7% tensile strain samples (Fig. 5.2) the MOKE signal amplitude rapidly increases within 10 ps (nucleation), and also shows some modest further growth at longer timescales for the highest magnetic fields, indicating that in those samples the final volume fraction of the FM phase is higher than in the compressively strained sample. By far the biggest effect is observed in the 1.4% tensile strained sample (Fig. 5.3), which shows a very large MOKE amplitude at longer timescales, which we therefore attribute to the fact that tensile strain facilitates the AFM-to-FM phase transitions.

The transients for longer time delays show that the maximum of the MOKE amplitudes occurs around 70-100 ps for all samples and at all fields, so the characteristic growth time seems to be independent of the field. Subsequently, the MOKE signal relaxes back to zero on much longer timescales, which takes longer at higher magnetic fields.

The origin of the growth of the net magnetization can be in principle connected with the spin reorientation process. However, this speed should depend on the strength of the external field as according to the Landau and Lifshitz equation (Eq.1.26 from Chapter 1) the magnetization vector can move faster in a higher effective field. In the experiment, we observe predominantly the other contribution to the growth of the net magnetization - the domain growth. Then the spread of the magnetic phase in this case depends on the heat distribution within the thin film and cannot be controlled with the external magnetic field. Further work is, however, necessary to completely describe and understand the full nucleation-growth process of FeRh films with various degrees of strain.

5.5.2 Demagnetization of FM domains below the phase transition

All samples exhibit a negative MOKE signal in the FM phase at 30 T, which results from the demagnetization transient after intense pulsed laser excitation [31, 32]. Remarkably, in particular the tensile and compressively strained samples also display a clear negative contribution to the MOKE signal at lower magnetic fields, which we attribute to the demagnetization of FM domains at 100 K and below H_C. We argue that the FeRh films might contain defects, which have been shown to play a crucial role in stabilizing FM domains, as they act as nucleation sites for ferromagnetism [25, 27, 28]. FM domains can be present in the (strained) samples in the AFM phase, even before the arrival of the pump pulse (Fig. 5.8(a)). Stabilized near the defects the FM phase will demagnetize under pulsed laser excitation (Fig. 5.8(b)), which results in the negative MOKE signal. The time dependence of this demagnetization signal is found to be almost independent of the sign of strain in the film (Fig. 5.7). Application of the magnetic field slightly increases the amount of demagnetization until the phase transition border is reached. The amplitude of the demagnetization is highest for the strained samples, consistent with the presence of a higher number of defects in the strained samples [8, 33]. With increasing magnetic field strength the amplitude of the magnetization signal remains more or less constant (see a plateau in D in Fig. 5.7) indicating that a magnetic field does not impact the further development of the FM domains stabilized at the defects until the phase co-existence region is reached at higher fields and only the negative demagnetization MOKE signal remains in the FM phase (Chapter 4 and Fig. 5.1) at 30 T. The demagnetization contribution is similar for the films under tensile and compressive strain and is absent in the unstrained sample, which is an indication that this signal is not related to the demagnetization of canted sublattices. According to our study in Chapter 4, the canting angle should increase with increasing magnetic field strengths and strain should then create an offset for the initial net magnetization and, correspondingly, for the demagnetization. Since we have no indication that this happens in our experiment, we rule out that the negative signal originates from the canted AFM phase and fully attribute it to the existence of FM domains at defects.

Remarkably, the main difference between the magnetization responses of the different samples at low field is given by this negative term. Indeed, the rise of the magnetic signal (value of τ_M) is similar for all samples, so the apparent delay in the growth of the MOKE signal for the strained films can be attributed to the occurrence of this demagnetization part. In fact, the trends of the behavior of the demagnetization term in the signal of the different samples, resemble the trends observed for the scaling parameter α for those samples.

5.5.3 Ultrafast oscillation

The compressively strained thin FeRh film is the only sample in which we have observed a strongly damped oscillation. The frequency F of this oscillation was found to be 46 ± 3 GHz, similar to the frequencies measured in FeRh using Brillouin light scattering due to magnons [34]. However, since the frequency and damping constant of our oscillation were found to be independent of the field strength, we can rule out a magnetic origin. This conclusion is supported by the fact that for this sample the volume fraction of the FM domains is relatively small (reduced values of B_{M}) and we would expect oscillations of magnetic origin coming from ferromagnetism or associated AFM-to-FM spin reorientation to be more profound in the the unstrained and tensile strained samples. Instead, the oscillations might be related to laser induced lattice vibrations or expansion waves, leading to fast fluctuations in the refractive index that cause oscillatory MOKE transients. However, this refractive index variation alone cannot explain the significant difference in the MOKE channel and the minimal contribution in the reflectivity channel. Intense pulsed laser excitation generates a substantial amount of heat that results in an increase of the lattice parameter provoking the AFM-FM phase transition in FeRh and a change in the magnetic state visible in MOKE. A rise in the temperature typically extends the unit cell in solids even without a phase transition [35]. We speculate that in the case of tensile strain, the excitation relaxes without further significant change in the lattice parameter, whereas under compression the expansion of the lattice parameter is reduced [36], restricting the growth of the FM domain. As a result, the FM nucleus, once excited by the laser, shrinks back to the stable size allowed with this lattice parameter change. This behaviour is consistent with the decreased amplitude of MOKE signals. The process of equilibration leads to an oscillatory behaviour.

In Chapter 4, we reported the observation of a similar oscillation in both the MOKE and reflectivity signals of a 40 nm thick unstrained FeRh film. In the current chapter, the unstrained film does not show an oscillation, which clearly points to an apparent difference between those two experiments on nominally the same sample. A possible explanation could be the different ways of sample mounting used in the two separate experiments. The experiment reported in Chapter 4 was conducted on a tightly glued sample, whereas in this chapter the sample was only glued partly on one side. For a tightly glued sample, upon cool down strain can develop due to the different thermal expansion coefficients of the sample, the substrate and the sample holder. Given the expansion coefficients of the different materials, where the thermal coefficient of brass significantly exceeds the ones of FeRh and MgO [37–39], we estimate that cooling of the sample holder leads to compressive strain in the FeRh film and to the appearance of the oscillation in the MOKE signal. Alternatively, for the truly unstrained sample studied in this chapter, we do not see any oscillation in fields of 5

T and higher.

5.5.4 Latency

A latency arises in the MOKE signal, when the system is in the collinear antiferromagnetic phase and the magnetic response is zero for some time τ_o after pump pulse excitation, whereas the reflectivity signal does not show this delay. The latency disappears above the spin-flop field H_{SF} in the canted AFM phase (Chapter 4) [13]. The unstrained sample of the current chapter does not show a latency, suggesting that this film is in the non-collinear phase at all magnetic fields measured ($\geq$ 5 T) and $H_{SF} <$ 5 T. With increasing strain, we expect an enhanced spin-flop field (Fig. 5.1), so the observation of latency for both tensile strained films is an agreement with this expectation 5 T $< H_{SF} <$ 10 T. However, the situation is more complicated. At 5 T, the latency τ_o increases from 0 ps for the unstrained sample to 5.6 ± 0.7 ps for the 0.7% tensile strained sample, as expected, but it decreases to 3.0 ± 0.3 ps for the 1.4% tensile strained film. We argue that indeed H_{SF} increases with strain, but at the same time H_C reduces with strain (Fig. 5.1). As such, the same external field of 5 T is not equivalent for the two strain states and the FM phase becomes accessible at lower fields. To understand how exactly these changes in the phase diagram determine the actual value of the latency requires dedicated experiments as a function of temperature and magnetic field. In particular, because the compressively strained sample did not show any latency under the conditions measured, whereas following the reasoning above this was expected to occur. From the experiment, we see no growth at all below 15 T in the compressively strained film. We cannot judge whether the latency is present just because we do not reach the phase transition boundary at all for these conditions. Also, we were limited to the strain levels of 0.7% in compression. At this strain level for the tensile strained sample, the latency was less pronounced as well. Moreover, according to the theoretical study [6], it is possible that the strain can change the anisotropy type from out-of-plane to in-plane.

Finally, also in the case of the observation of latency a difference in the ultrafast response is observed between the nominally unstrained samples in this chapter and Chapter 4. The tightly glued sample of that chapter showed both latency at low fields, which is consistent with the presence of (compressive) strain in that film, in agreement with the observation of the ultrafast oscillation, discussed in the previous section.

Clearly, the discrepancy in the measured behaviour, the observation of latency and ultrafast oscillations, of the unstrained and tightly glued samples demonstrate that it is essential to take into account the effects of the sample preparation techniques on the presence of internal strain in the FeRh films and care should be taken in the analysis of the results.

5.6 Conclusions

We have investigated the effect of strain on the laser-induced phase dynamics in FeRh. The emergence of a net magnetization deep in the antiferromagnetic phase at 100 K was observed in external magnetic fields up to 30 T. By mechanically applying 0.7% and 1.4% of tensile strain and 0.7% of compressive strain we were able to compare the behaviour of the same FeRh thin film with different levels of strain.

Both compressive and tensile strain modify the dynamics substantially. However, strain does not lead to a change in the speed of the nucleation of FM domain or their subsequent growth. The typical characteristic time for nucleation is approximately 3 ps, whereas the time to reach the largest volume fraction of the FM phase is roughly 70-100 ps. Strain affects the volume of the induced FM nuclei as well as the amount of the total FM volume in the probed area. Under tensile (compressive) strain, the phase transition is supported (suppressed), resulting in the generation of a larger (smaller) volume fraction of the FM phase.

Introducing mechanical strain likely leads to the creation of defects in the FeRh layer and the generation of FM domains in their vicinity, even deep in the AFM phase. This was demonstrated by the presence of a negative signal MOKE at temperatures and magnetic field strengths far below the phase transition.

Incorporating tensile strain into the system induces latency in the response of the magnetic signal at 5 T, and as the strain is increased, the latency time progressively diminishes, which is indicative of a higher spin-flop field for higher levels of tensile strain.

Finally, compressive strain induces an unstable behavior, manifesting itself as an underdamped oscillation in both the lattice and magnetic systems. This oscillation is observed only in tandem with the occurrence of the phase transition. The amplitude of these oscillations parallels the growth of net magnetization.

Bibliography

[1] C. W. Barton, T. A. Ostler, D. Huskisson, C. J. Kinane, S. J. Haigh, G. Hrkac, and T. Thomson, Scientific Reports **7**, 44397 (2017), ISSN 2045-2322.

[2] M. G. Loving, R. Barua, C. Le Graët, C. J. Kinane, D. Heiman, S. Langridge, C. H. Marrows, and L. H. Lewis, Journal of Physics D: Applied Physics **51**, 024003 (2018), ISSN 0022-3727, 1361-6463.

[3] H. Kumar, D. R. Cornejo, S. L. Morelhao, S. Kycia, I. M. Montellano, N. R. Álvarez, G. Alejandro, and A. Butera, Journal of Applied Physics **124**, 085306 (2018), ISSN 0021-8979, 1089-7550.

[4] J. A. Arregi, O. Caha, and V. Uhlíř, Physical Review B **101**, 174413 (2020), ISSN 2469-9950, 2469-9969.

[5] J. A. Arregi, F. Ringe, J. Hajduček, O. Gomonay, T. Molnár, J. Jaskowiec, and V. Uhlíř, Journal of Physics: Materials **6**, 034003 (2023), ISSN 2515-7639.

[6] C. Bordel, J. Juraszek, D. W. Cooke, C. Baldasseroni, S. Mankovsky, J. Minár, H. Ebert, S. Moyerman, E. E. Fullerton, and F. Hellman, Physical Review Letters **109**, 117201 (2012), ISSN 0031-9007, 1079-7114.

[7] A. Ceballos, Z. Chen, O. Schneider, C. Bordel, L.-W. Wang, and F. Hellman, Applied Physics Letters **111**, 172401 (2017), ISSN 0003-6951, 1077-3118.

[8] W. Griggs, B. Eggert, M. O. Liedke, M. Butterling, A. Wagner, U. Kentsch, E. Hirschmann, M. Grimes, A. J. Caruana, C. Kinane, et al., APL Materials **8** (2020).

[9] C. Kittel, Physical Review **120**, 335 (1960), ISSN 0031-899X.

[10] M. P. Annaorazov, S. A. Nikitin, A. L. Tyurin, K. A. Asatryan, and A. Kh. Dovletov, Journal of Applied Physics **79**, 1689 (1996), ISSN 0021-8979, 1089-7550.

[11] G. T. Dubovka, Soviet Journal of Experimental and Theoretical Physics **38**, 1140 (1974), ISSN 1063-7761.

[12] A. K. Zvezdin, in *Handbook of Magnetic Materials* (Elsevier, 1995), vol. 9, pp. 405–543.

[13] G. Li, R. Medapalli, J. H. Mentink, R. V. Mikhaylovskiy, T. G. H. Blank, S. K. K. Patel, A. K. Zvezdin, Th. Rasing, E. E. Fullerton, and A. V. Kimel, Nature Communications **13**, 2998 (2022), ISSN 2041-1723.

[14] J. W. Allen, Physical Review B **7**, 4915 (1973).

[15] A. Kozioł-Rachwał, M. Ślęzak, M. Zając, P. Dróżdż, W. Janus, M. Szpytma, H. Nayyef, and T. Ślęzak, APL Materials **8**, 061107 (2020), ISSN 2166-532X.

[16] I. A. Dolgikh, T. G. H. Blank, A. G. Buzdakov, G. Li, K. H. Prabhakara, S. K. K. Patel, R. Medapalli, E. E. Fullerton, O. V. Koplak, J. H. Mentink, et al., *Ultrafast Emergence of Ferromagnetism in Antiferromagnetic FeRh in High Magnetic Fields* (2023), 2202.03931.

[17] R. Medapalli, G. Li, S. K. K. Patel, R. V. Mikhaylovskiy, Th. Rasing, A. V. Kimel, and E. E. Fullerton, Applied Physics Letters **117**, 142406 (2020), ISSN 0003-6951, 1077-3118.

[18] J. Hohlfeld, S. S. Wellershoff, J. Güdde, U. Conrad, V. Jähnke, and E. Matthias, Chemical Physics **251**, 237 (2000), ISSN 0301-0104.

[19] B. B. Karki, L. Stixrude, S. J. Clark, M. C. Warren, G. J. Ackland, and J. Crain, American Mineralogist **82**, 51 (1997), ISSN 1945-3027.

[20] E. Carpene, E. Mancini, C. Dallera, M. Brenna, E. Puppin, and S. De Silvestri, Physical Review B **78**, 174422 (2008).

[21] N. Thielemann-Kühn, D. Schick, N. Pontius, C. Trabant, R. Mitzner, K. Holldack, H. Zabel, A. Föhlisch, and C. Schüßler-Langeheine, Physical Review Letters **119**, 197202 (2017), ISSN 0031-9007, 1079-7114.

[22] F. Pressacco, D. Sangalli, V. Uhlíř, D. Kutnyakhov, J. A. Arregi, S. Y. Agustsson, G. Brenner, H. Redlin, M. Heber, D. Vasilyev, et al., Nature Communications **12**, 5088 (2021), ISSN 2041-1723.

[23] S. O. Mariager, F. Pressacco, G. Ingold, A. Caviezel, E. Möhr-Vorobeva, P. Beaud, S. L. Johnson, C. J. Milne, E. Mancini, S. Moyerman, et al., Physical Review Letters **108**, 087201 (2012), ISSN 0031-9007, 1079-7114.

[24] B. Bergman, G. Ju, J. Hohlfeld, R. J. M. van de Veerdonk, J.-Y. Kim, X. Wu, D. Weller, and B. Koopmans, Physical Review B **73**, 060407 (2006), ISSN 1098-0121, 1550-235X.

[25] C. Baldasseroni, C. Bordel, A. X. Gray, A. M. Kaiser, F. Kronast, J. Herrero-Albillos, C. M. Schneider, C. S. Fadley, and F. Hellman, Applied Physics Letters **100**, 262401 (2012), ISSN 0003-6951, 1077-3118.

[26] C. Baldasseroni, C. Bordel, C. Antonakos, A. Scholl, K. H. Stone, J. B. Kortright, and F. Hellman, Journal of Physics: Condensed Matter **27**, 256001 (2015), ISSN 0953-8984, 1361-648X.

[27] D. J. Keavney, Y. Choi, M. V. Holt, V. Uhlíř, D. Arena, E. E. Fullerton, P. J. Ryan, and J.-W. Kim, Scientific Reports **8**, 1778 (2018), ISSN 2045-2322.

[28] Y. Ahn, M. J. Cherukara, Z. Cai, M. Bartlein, T. Zhou, A. DiChiara, D. A. Walko, M. Holt, E. E. Fullerton, P. G. Evans, et al., Proceedings of the National Academy of Sciences **119**, e2118597119 (2022).

[29] X. Zhou, F. Matthes, D. E. Bürgler, and C. M. Schneider, AIP Advances **6**, 015211 (2016), ISSN 2158-3226.

[30] S. B. Palmer, P. Dentschuk, and D. Melville, physica status solidi (a) **32**, 503 (1975), ISSN 1521-396X.

[31] P. M. Oppeneer and A. Liebsch, Journal of Physics: Condensed Matter **16**, 5519 (2004), ISSN 0953-8984.

[32] N. Awari, A. Semisalova, J.-C. Deinert, K. Lenz, J. Lindner, E. Fullerton, V. Uhlíř, J. Li, B. Clemens, R. Carley, et al., Applied Physics Letters **117**, 122407 (2020), ISSN 0003-6951, 1077-3118.

[33] I. Gray, G. M. Stiehl, J. T. Heron, A. B. Mei, D. G. Schlom, R. Ramesh, D. C. Ralph, and G. D. Fuchs, Physical Review Materials **3**, 124407 (2019).

[34] Y. Jin, Y. Tian, H. Wu, Y. Zhang, C. Li, F. Liu, G. Chai, and C. Jiang, Journal of Physics D: Applied Physics **55**, 355301 (2022), ISSN 0022-3727.

[35] M. Hunkel, H. Surm, and M. Steinbacher, in *Handbook of Thermal Analysis and Calorimetry*, edited by S. Vyazovkin, N. Koga, and C. Schick (Elsevier Science B.V., 2018), vol. 6 of *Recent Advances, Techniques and Applications*, pp. 103–129.

[36] R. Fan, C. J. Kinane, T. R. Charlton, R. Dorner, M. Ali, M. A. de Vries, R. M. D. Brydson, C. H. Marrows, B. J. Hickey, D. A. Arena, et al., Physical Review B **82**, 184418 (2010), ISSN 1098-0121, 1550-235X.

[37] P. D. Merica and L. W. Schad, *Thermal Expansion of Alpha and of Beta Brass Between 0 and 600© C: In Relation to the Mechanical Properties of Heterogeneaous Brasses of the Muntz Metal Type* (U.S. Department of Commerce, Bureau of Standards, 1919).

[38] D. K. Smith and H. R. Leider, Journal of Applied Crystallography **1**, 246 (1968), ISSN 0021-8898.

[39] M. R. Ibarra and P. A. Algarabel, Physical Review B **50**, 4196 (1994).

Chapter 6

Thickness dependence of the ultrafast magnetostructural phase transition in FeRh

We report on a study of the dynamics of the laser induced antiferromagnetic (AFM) to ferromagnetic (FM) phase transition in FeRh films of varying thickness d = 20 - 40 nm. We find that the timescale of the initial nucleation of the FM domains is roughly independent of the film thickness and can be described by a 3 ps rise time of the time-resolved MOKE signal. The thinnest film measured exhibits a large volume of the induced FM phase, stabilized over 2 ns timescales, especially under higher magnetic fields. This response possibly results from 1) the presence of stable FM domains at the interface of the FeRh film and the MgO substrate of the samples or 2) the presence of tensile strain in the films, arising from the difference in lattice constants of FeRh and MgO. The latter scenario is supported by a strong temperature dependence of the response at longer timescales, due to the difference in thermal expansion coefficients of film and substrate, which might cause changes in the magnetocrystalline anisotropy. The important role of strain (waves) is also exemplified by the observation of ultrafast oscillations in the MOKE response, stressing the intricate interplay between the spin and lattice subsystems in FeRh.

6.1 Introduction

This chapter is devoted to the investigation of the phase transition from the antiferromagnetic (AFM) to ferromagnetic (FM) phase in FeRh films. Despite multiple studies on this matter [1], the nature of the phase transition in this material remains unclear. After 60 years of debates, using the

results of numerous experimental and theoretical studies, it is clear that to uncover the processes happening during this magneto-structural transformation, we need more sophisticated experimental tools and measurements under different and even more extreme conditions, such as low temperatures and high magnetic fields. In the previous chapters 4 and 5 we addressed the non-equilibrium dynamics of this phenomenon, using experiments, for the first time for this material, in external magnetic fields up to 30 T. It was found that the speed of the initial nucleation of the FM domains upon ultrafast heating does not depend on the external magnetic field (chapter 4) and strain state (chapter 5). At the same time, the lattice and spin systems have been shown to be highly interconnected, in agreement with the results in literature [1–6]. In addition, in chapter 5 we found out that the volume of the induced FM domains is highly sensitive to the strain present in the FeRh layer.

Clearly, the phase transition is complex and involves the mutual interplay of a number of different subsystems, including the lattice and the spins of Fe and Rh, which makes it necessary to investigate separately different experimental dependencies. To this end, this chapter focuses on the dependence on the thickness of the FeRh film. Thin films with a thickness d in the range of 2 - 200 nm have been thoroughly investigated using magnetostatics and it was found that for $d < 50$ nm, the actual thickness of the layer influences different aspects of the magnetoelastic phase transition, which might be relevant for the laser-induced ultrafast dynamics. For example, strain in the FeRh layer induced by the underlying substrate can constrain the expansion of the in-plane lattice parameters, as demonstrated in [7]. When this limitation affects the reorientation of the spins, it could manifest itself in the first nucleation of FM domains, as well as in the growth of the FM phase at a later stage of the transition. In addition, reducing the film thickness has been found to decrease the transition temperature [8, 9] and to cause lattice asymmetry [8, 10], broadening of the range of the transition temperatures [8, 9, 11] and changes in grain size [8, 10]. Notably, ultrathin films, with thicknesess below 5 - 10 nm, may even lose the stability of the antiferromagnetic phase [10, 12]. Finally, to which extent the lattice parameter increases at the phase transition also varies between bulk FeRh and thin FeRh films [7, 13].

Several time-resolved XRD [6, 14, 15] and XAS experiments [16], have claimed that ultrafast lattice expansion creates a standing wave that travels from the surface of the FeRh film to its substrate and back after reflection, thereby defining the characteristic time of the lattice expansion and the magnetostructural phase transition in the film based on its thickness. However, recent work [17] observed a lattice contraction on a 5 ps timescale in a 500 nm thick film, much faster than 200 ps, which is expected for the standing wave given the velocity of sound of $v_s \sim 5$ nm/ps. In chapter 5 we observed a characteristic oscillation in a 40 nm thick FeRh film under

compressive strain. By investigating the thickness dependence of the period of this type of oscillations we will be able to investigate whether they are caused by standing waves.

Most of the existing works attribute the effects found in the thin films to the presence of strain at the interface of the FeRh layer and its substrate ([10, 18, 19] and other above-mentioned works). However, the impact on the speed and the dynamics of the phase transition under these conditions remains unexplored. Indeed, as demonstrated in the previous chapter 5, the amount of strain significantly affects the volume of the excited domains. So, a thickness dependent study will gain insight in to what extent the substrate-induced strain influences the nucleation and growth of FM domains after ultrafast laser heating.

As in the previous chapters, we will trigger the AFM-to-FM phase transition by 100 fs laser pulses. By using appropriate conditions of low temperatures and high magnetic fields, we are able to distinguish the nucleation and growth regime of the phase transition and investigate the effect of varying film thickness on both regimes. This chapter is organized as follows. The next section describes the composition of the 20 and 30 nm thick FeRh samples and the experimental conditions used, followed by section 6.3 that describes the magnetic characterization of the 20 nm thick sample. The results of the ultrafast experiments are given in section 6.4, followed by the data analysis in section 6.5. The effect of the layer thickness on the ultrafast nucleation and growth of the FM domains, as well as the oscillatory response in MOKE is discussed in section 6.6. The overall conclusion is given in the final section.

6.2 Sample and experimental details

We conducted a magneto-optical study of FeRh films with thicknesses of 20 nm and 30 nm. The films were grown on a MgO single crystal through magnetron sputtering and capped by a 5 nm layer of Au, to ensure the stability of the sample. The details of the manufacturing procedure and properties of the produced films are described in Ref. [20]. Throughout the chapter the results of the 20 and 30 nm thick films will be compared to those of the 40 nm thick films described in chapters 4 and 5.

We characterized the magnetization state of the 20 nm sample as a function of applied magnetic field by static MOKE, using a continuous laser beam with 632 nm wavelength, chopped at a frequency of 500 Hz and measured through a balanced photodetector scheme in the same way as is done in the pump-probe experiment for the probe pulse (Chapter 2).

Utilizing the magnetic field installation in the HFML-FELIX laboratory, the ultrafast dynamics of the AFM-to-FM phase transition was measured by means of a two-coloured pump-probe scheme in a wide temperature range (5 K - 250 K) for magnetic fields up to 30 T. The setup and the

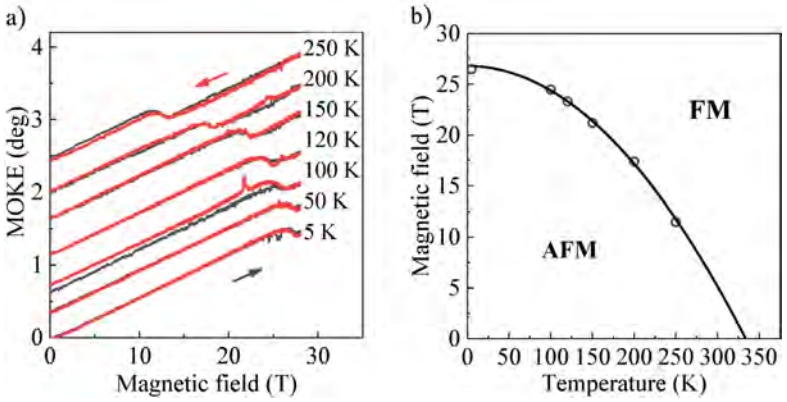

Figure 6.1: (a) Polar MOKE from a 20 nm thick FeRh film for a set of temperatures from 5 K to 250 K. The magnetic field was swept from 0 T to 30 T and back. Both up- and down-sweeps are shown. The data taken at different temperatures are vertically shifted for clarity. (b) Temperature dependence of the magnetic field at which the phase transition occurs, obtained by taking the derivative of the curves in (a) and plotting the peak position of the derivative. The solid line is a fit with the formula proposed by [22]. Below the line (bottom left corner) the 20 nm layer is in the antiferromagnetic phase, whereas above the line (top right corner) it is in the ferromagnetic phase.

procedure that we used have been described in detail in Chapter 2. Briefly, the pump fluence, at a wavelength of 800 nm (1.55 eV), was kept constant at 4.1 mJ/cm^2 throughout the whole set of measurements, corresponding to a temperature increase of the FeRh film of about 230 K [21]. To probe the changes in the magnetic state of the sample a beam at a different wavelength, 660 nm (1.9 eV), was used obtained from an optical parametric amplifier (OPA). The signal was detected using a balanced photodetector (Chapter2). It allowed us to measure simultaneously the polar MOKE signal and the change in the reflectivity of the sample.

The samples were positioned, next to one another, on a movable mount from Attocube to ensure that they were measured under the same experimental conditions. As described in the previous chapters, how the samples are fixed to the holder is important for the amount of residual strain that is present in the FeRh films at each temperature used, as a result of the difference in the thermal expansion of the FeRh film, the MgO substrate and the sample holder. The samples were mounted in a He-4 bath cryostat in cell 2 of HFML-FELIX, and two resistive heaters were employed to change the temperature.

6.3 Magnetic characterization

For thin FeRh films, the AFM phase might disappear, as evident from studies on ultrathin films [10, 12] and nanoparticles [23]. To this end we have determined the magnetization state of the 20 nm thick FeRh film across the temperature range, using steady-state MOKE. Unfortunately, the MOKE response of the 30 nm thick film could not be measured due to an increased magnetic torque causing the sample to be dislocated at high fields. Figure 6.1(a) shows the resulting MOKE traces of the 20 nm sample for various temperatures in between 5 K and 250 K. Each curve shows a linearly increasing signal, coming from the diamagnetic background of our set-up, which was not subtracted. On top of this background, all traces show a drop in signal at a certain field strength, indicative of the AFM-to-FM phase transition, which moves to lower fields with increasing temperature. Interestingly, this phase transition is of 1st order and is usually accompanied by a wide hysteresis. In this case, however, the measurements do not show any hysteresis, in contrast to the MOKE results for the 40 nm thick FeRh film shown in Chapter 4.

To determine the critical magnetic field of the magnetostructural phase transition as a function of temperature, we differentiated all MOKE traces and interpreted their peak positions as the critical fields (symbols in Figure 6.1(b)). The solid line corresponds to a fit of the data points with the experimental law (eq.4.1), as was done in Chapter 4. This resulted in $T_C = 333 \pm 3$ K, the critical temperature without external magnetic field and $H_C = 26.7 \pm 0.2$ T, the critical magnetic field at zero kelvin. The 20 nm FeRh film is in the AFM phase below this line (low magnetic fields and temperatures) and in the FM phase above this line (at higher fields and temperatures). Remarkably, these values of T_C and H_C are lower than the values found for the 40 nm film ($T_C = 378 \pm 2$ K, $H_C = 31.7 \pm 0.6$ T) in Chapter 4. These findings qualitatively agree with the results from thickness dependent experiments reported in literature [9, 19] and predicted by calculations assuming the change in the exchange interaction constants due to the presence of an interface [24].

6.4 Ultrafast dynamics experiments

6.4.1 Magnetic field dependence

Figure 6.2 shows the magnetic field dependence of the ultrafast MOKE and reflectivity change signals for the 20 nm (purple) and 30 nm (yellow) thick FeRh films, recorded at a temperature $T = 100$ K. This specific temperature was chosen, because under these conditions the FeRh samples are in the AFM phase across a large magnetic field range, and the nucleation and growth processes can be observed separately (like in Chapter 5). Focusing

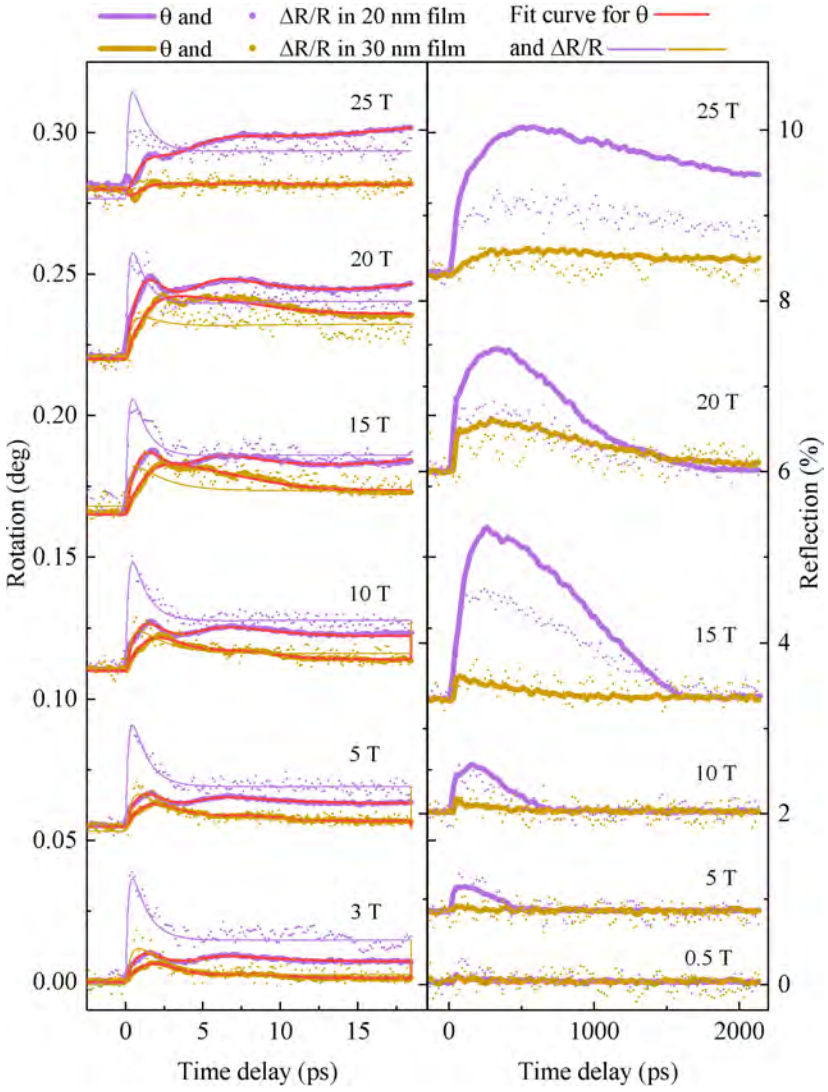

Figure 6.2: Laser-induced polar MOKE (solid lines) and reflectivity change (dotted symbols) signals for the 20 nm (purple) and 30 nm (yellow) thick FeRh films, for selected external magnetic fields up to 25 T and at temperature $T = 100$ K. For clarity the data at the different magnetic fields are vertically offset. The red solid lines and the thin lines correspond to the fits of respectively the MOKE and reflectivity data with exponential decay functions and two damped oscillations, as described in the text. The left (right) panel shows the time-resolved traces up to 18 ps (2 ns).

first on the dynamics on a 20 ps timescale (left panel Fig. 6.2), we see that both films display an overall similar response, i.e. a steep rise of the MOKE and reflectivity signals on a timescale of about 5 ps, roughly comparable to the traces of the 40 nm thick films reported in chapters 4 and 5. Closer inspection reveals, however, marked differences between the samples. First of all, the MOKE traces exhibit clear oscillatory behaviour, similar to the response of the 40 nm film under compressive strain (Chapter 5) and the 40 nm film in Chapter 4. The 20 nm sample shows visibly quicker dynamics and a slightly higher magneto-optical effect. However, we do not observe any latency or negative signal at low magnetic fields in this set of measurements. Also, at 25 T the 20 nm film still undergoes a laser-induced phase transition while in the 30 nm sample, it is already suppressed. Finally, the reflectivity signal has a similar appearance for both samples, although the 20 nm film has a twice higher signal, relative to the 30 nm film.

Interestingly, the response at a longer timescale (right panel Fig. 6.2) demonstrates entirely different dynamics between the two samples. The MOKE and Reflectivity signals of the 20 nm film do not relax immediately after the pump excitation, but continue to grow over a timescale of 500 ps, exhibiting remarkably high amplitudes, especially at larger magnetic fields. The maximum amplitude reached shows a non-monotonic behaviour with varying field, first increasing with field up to 15 T and subsequently decreasing somewhat in amplitude. At the highest field (25 T) the time-dependent MOKE and Reflectivity signals remain substantially high for time delays as long as 2 ns. This behaviour is absent in the 30 nm film, which behaves more or less comparable to the response of the 40 nm thick films, reported in the previous chapters.

6.4.2 Temperature dependence

To gain more insight in the ultrafast response of the thinner FeRh films, the experiment was repeated for other temperatures in the range of 5 K to 250 K. Figure 6.3 shows the MOKE and reflectivity transients at an external field of 5 T. Remarkably, several features of the MOKE and reflectivity data show a marked temperature dependence. First of all, the oscillatory behaviour in the MOKE signal at short timescales (left panel) decreases significantly in amplitude with increasing temperature. Whereas the oscillations are clearly visible at the lower temperatures for both samples, they can be hardly be observed at elevated temperatures of 200 and 250 K. In addition, the response at longer timescales (right panel) strongly depends on temperature. For the 20 nm thick sample the amplitudes of the MOKE and reflectivity data are quite substantial at 5 K, decrease with temperature up to 100 K, and subsequently increase again for higher temperatures. Whereas the long timescale component for the 30 nm sample is absent for the lower temperatures, it appears at a temperature of 250 K, exhibiting a

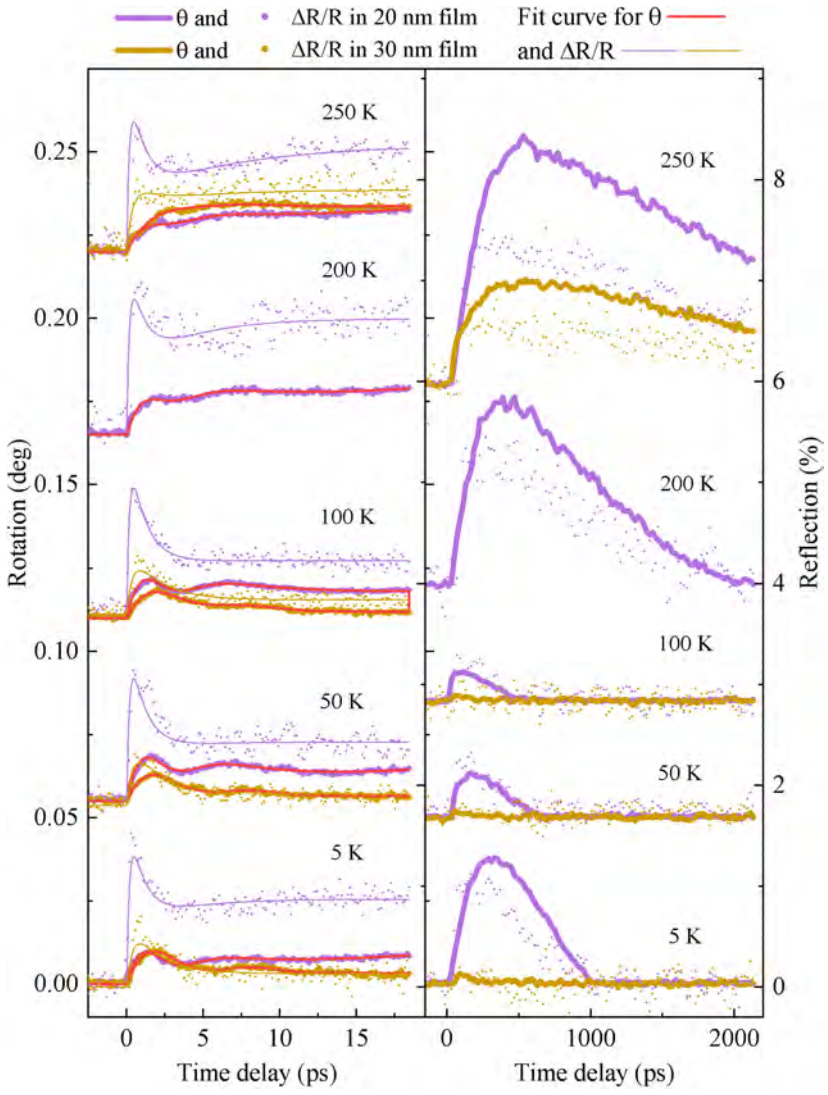

Figure 6.3: Laser-induced polar MOKE (solid lines) and reflectivity change (dotted symbols) signals for the 20 nm (purple) and 30 nm (yellow) thick FeRh films, for selected temperatures between 5 K and 250 K at a magnetic field of 5 T. For clarity the data at the different temperatures are vertically offset. The red solid lines and the thin lines correspond to the fits of respectively the MOKE and reflectivity data with exponential decay functions and two damped oscillations, as described in the text. The left (right) panel shows the time-resolved traces up to 18 ps (2 ns).

high response up to 2 ns time delays, comparable to the 20 nm thick film.

6.5 Data analysis

6.5.1 Fitting procedure and results for the dynamics at a 20 ps timescale

To compare the results of the samples with various thicknesses, we have fitted the short-term time-resolved traces up to 20 ps using the procedures described in the previous chapters. Overall, the data obtained from the 20 and 30 nm thick films are comparable to that of the 40 nm sample described in the previous chapters. In fact, the MOKE signals of the two thinner samples did not show any sign of latency or negative demagnetization signal, so those terms have not been used. Instead, only a set of exponential functions and damped oscillations proved sufficient to describe the full datasets. As before, the rise of the MOKE and reflectivity signals is decribed by exponential functions:

$$\begin{aligned} \frac{\Delta R}{R}(t) &= A_{\mathrm{L}} \cdot (1 - \mathrm{e}^{-t/\tau_{\mathrm{L}}}) \\ \theta(t) &= B_{\mathrm{M}} \cdot (1 - \mathrm{e}^{-t/\tau_{\mathrm{M}}}). \end{aligned} \tag{6.1}$$

This term describes the emergence of the net magnetization with amplitude B_{M} and time constant τ_{M}, as measured by MOKE, and the contribution from the lattice dynamics in the reflectivity response, given by amplitude A_{L} and time constant τ_{L}. In the previous chapter the rise times τ_{M} and τ_{L} were found to be magnetic field and strain independent. Also in the present data sets no strong variation in the rise times was observed, so in the further fitting procedure the rise times where not used as a free parameter, but fixed to 3.0 ps.

The reflectivity signal contains several terms resulting from the complex electron-lattice dynamics:

$$\frac{\Delta R_{\mathrm{el}}}{R}(t) = A_{\mathrm{e1}} \cdot (1 - \mathrm{e}^{-t/\tau_{\mathrm{e1}}}) - A_{\mathrm{e2}} \cdot (1 - \mathrm{e}^{-t/\tau_{\mathrm{e2}}}). \tag{6.2}$$

The first term corresponds to the effect on the reflectivity of the laser induced heating of the electron system, leading to the presence of hot electrons. The second term describes the cooling of the electron system due to the relaxation of heat to the phonon system. Our starting point was to fit the reflectivity at conditions far from the phase transition (low magnetic fields and temperatures), to determine the bare parameters of the reflectivity signal without influence of the phase transition. For the 30 nm sample this resulted in $A_{\mathrm{e1}} = 0.70 \pm 0.08\%$, $\tau_{\mathrm{e1}} = 0.38 \pm 0.09$ ps, $A_{\mathrm{e2}} = 0.59 \pm 0.08\%$, $\tau_{\mathrm{e2}} = 2.0 \pm 0.3$ ps, and for the 20 nm film this gave $A_{\mathrm{e1}} = 1.89 \pm 0.09\%$,

$\tau_{e1} = 0.18 \pm 0.02$ ps, $A_{e2} = 1.37 \pm 0.09\%$, $\tau_{e2} = 1.01 \pm 0.04$ ps. Subsequently, the reflectivity traces for other fields and temperatures were fitted with these parameters fixed and with an exponential rise due to the AFM-to-FM phase transition.

In the polarization rotation signal, besides the exponential rise, we observe oscillatory behaviour, which was fitted with a damped harmonic oscillator function:

$$\theta_F(t) = C_M \cdot \cos(2\pi F t - \pi/2) e^{-\gamma t}, \tag{6.3}$$

with amplitude C_M, frequency F and damping γ. It turned out, however, that the ultrafast transients could not be properly described using only one oscillatory function with a certain frequency. To resolve this issue, we included two oscillations of the form of Eq. 6.3 each with a different frequency. A typical example of the fitting result for the 30 nm film is shown in Fig. 6.4(b), which plots the MOKE signal at 5 T, consisting of the exponential rise with a time constant of 3 ps, and two damped oscillations with two different frequencies. To describe the MOKE signal of the 20 nm thick film we had to include an additional exponential function to account for the slow rise of the magnetic signal due to the further domain growth and alignment at longer timescales (Fig. 6.2 right). The characteristic time constant of this component was taken to be 150 ps and is shown by the green dashed curve in Fig. 6.4(a), which describes the MOKE transient of the 20 nm sample at 15 T.

Using this procedure, all data transients were fitted, the results of which are shown by the red solid and thin lines in Figs.6.2 and 6.3. The decay rates γ were found to be independent of the magnetic field strength and temperature. For the 20 nm sample we found $\gamma = 0.61 \pm 0.07$ ps^{-1} for the fast oscillation and $\gamma = 0.183 \pm 0.022$ ps^{-1} for the slow one. The 30 nm film gave $\gamma = 0.310 \pm 0.027$ ps^{-1} and $\gamma = 0.319 \pm 0.012$ ps^{-1} respectively for the fast and slow oscillations.

Fig. 6.5 shows that the frequencies F of the oscillations for both sample thicknesses are roughly independent of the magnetic field. Averaging the frequencies over the entire magnetic field range, leads to the values plotted in Fig.6.6(a). The fast and slow oscillations are characterized by time constants of approximately 6 and 30 ps respectively, independent of the sample thickness (Fig.6.6(b)). These results also show that the oscillation detected in the MOKE signal of the 40 nm thick film (chapter4) corresponds to the slow oscillation in the thinner samples.

Fig. 6.6(c) shows the amplitudes of the oscillations in both samples, which reveals two interesting trends. The first trend we observe is a significant thickness dependence. For the 20 nm thick sample, the amplitudes of both fast and slow oscillations are about the same. In contrast, for the 30 nm thick film, the slow oscillation has a much higher amplitude than the fast one. And finally, the 40 nm samples of chapters 4 and 5 only show

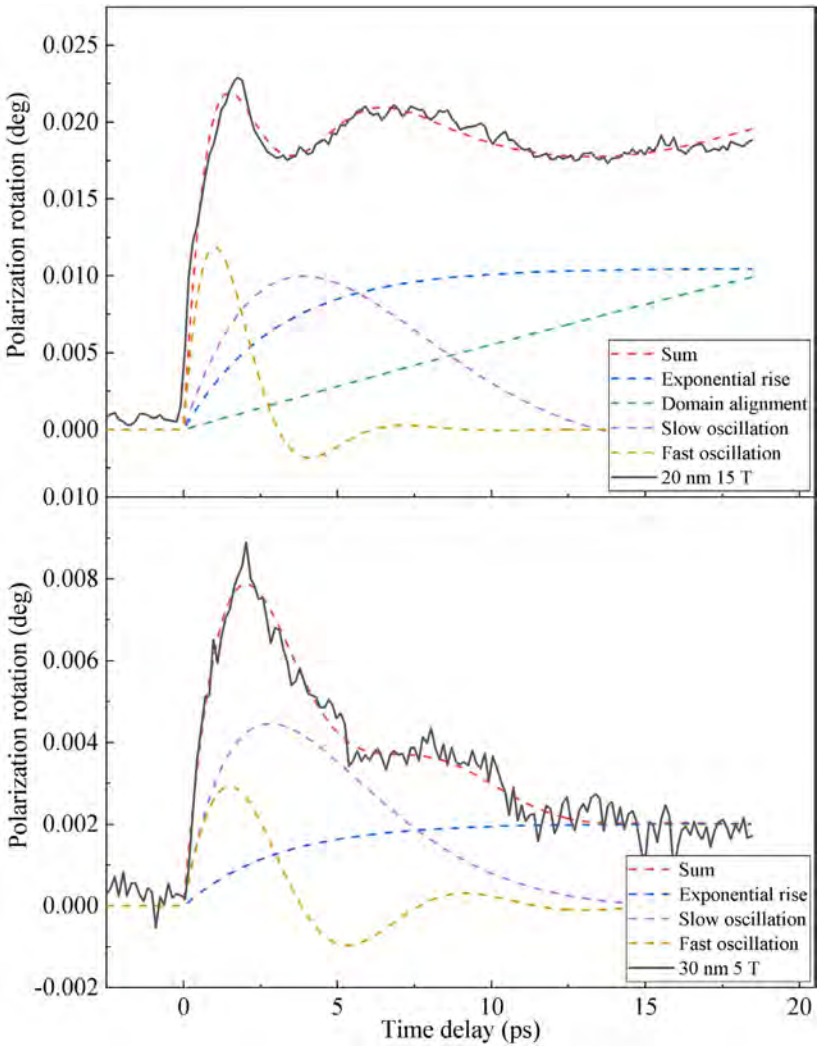

Figure 6.4: Illustration of the fitting procedure for the MOKE signal of the 20 nm FeRh film at 15 T (top panel) and the 30 nm film at 5 T (bottom panel). The data is shown by the solid black lines. The dashed lines represent the final fits (red) and its contributions: Exponential magnetization growth from eq. 6.1 (blue); further domain growth and alignment (green); oscillatory part from eq. 6.3 with different frequencies (yellow and purple).

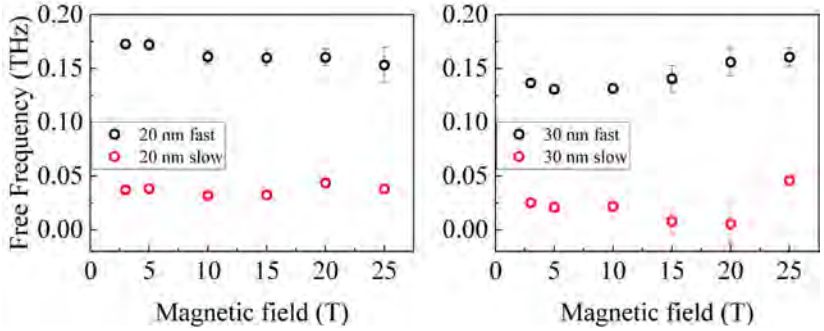

Figure 6.5: Fitted frequencies (F) of the fast and slow oscillations in the MOKE signals of the 20 and 30 nm thick FeRh films.

the slow oscillation. Clearly, the fast oscillation only appears in thin FeRh films and is absent in thicker samples. The second trend we observe is the magnetic field dependence of the oscillation amplitudes. In almost all cases the oscillation amplitude increases with magnetic field, with the only exception the fast oscillation of the 30 nm sample, which is small anyway. A growing oscillation amplitude with increasing field strength was also observed for the compressively strained 40 nm thick film in chapter 5 (Fig. 5.6(f)). Finally, at the highest field used, approaching the AFM-to-FM phase transition, the oscillation amplitudes reduce in size (Fig. 6.6(c)). This behaviour of initial field-induced growth of the amplitude and a subsequent decline at higher fields, resembles the behaviour of the amplitude of the exponential rise of the MOKE and reflectivity signals in the 20 and 30 nm thick samples (Fig. 6.6(d)) and the 40 nm samples (Fig. 5.6(c,d) in chapter 5), suggesting that the appearance of the slow oscillation is directly connected to the appearance of the FM domains in the AFM phase. Indeed, the trend shows that the oscillation is associated with the phase transition rather than represents a separate phenomenon of a breathing film or another pure lattice excitation.

Figure 6.7 shows the fitted parameters for the temperature dependent data set of Fig. 6.3. Remarkably, the amplitude of both the fast and slow oscillation components go down with increasing temperature.

6.5.2 Analysis of the dynamics at a 2 ns timescale

As described in the experimental section, the ultrafast MOKE response of the samples with different thicknesses particularly differ from each other on the longer timescale up to 2 ns (right panels in Figs. 6.2 and 6.3). To visualize the most important trends we performed a rough analysis of the data without fitting the full curves. Fig. 6.8(a,b) shows the magnetic field and temperature dependence of the maximum value of the MOKE amplitude

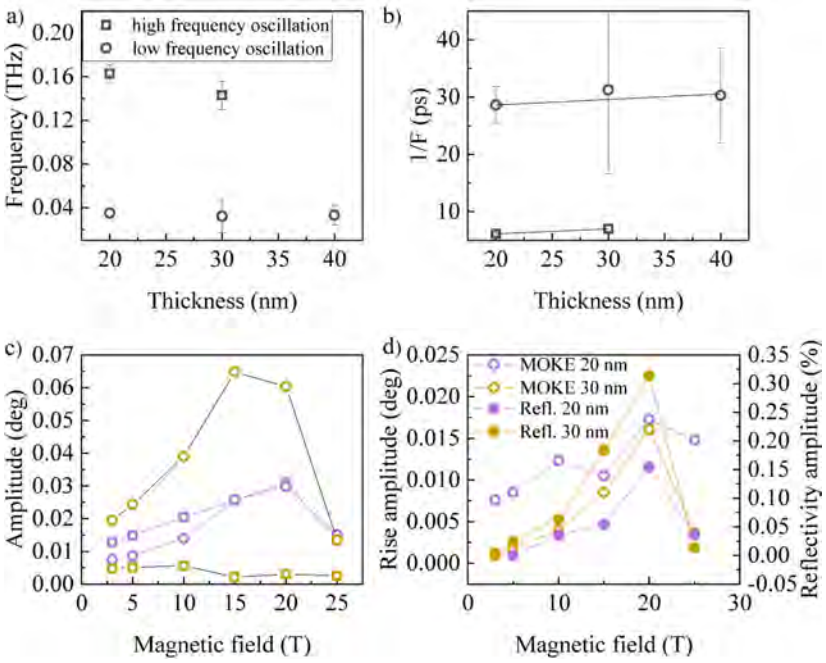

Figure 6.6: Fitted parameters of the data shown in Fig.6.2. Open and closed symbols correspond to respectively the oscillation and exponential components of the fits of the MOKE data. Open squares (fast) and circles (slow) denote the different oscillation terms. The symbol colors indicate the results for the 20 nm (purple) and 30 nm (yellow) thick FeRh films. (a) Frequencies of the two damped oscillations in the polar MOKE. (b) Inverse frequency of the oscillations for the different samples. The lines are guides to the eye. (c) Amplitudes of the oscillatory parts as a function of magnetic field. (d) Field dependence of the amplitudes of the exponential rise in MOKE (open circles) and reflectivity (closed circles) with $\tau = 3$ ps.

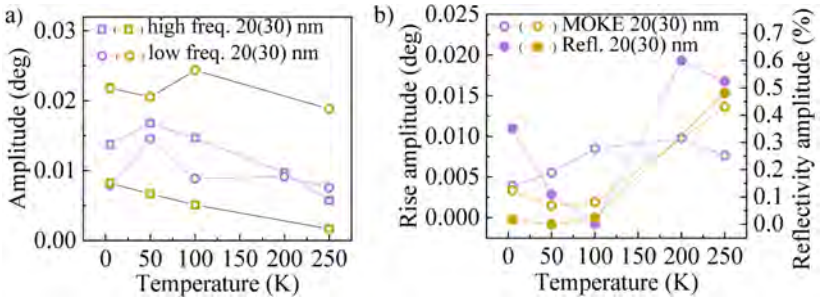

Figure 6.7: Fitted parameters of the data shown in Fig.6.3. Open and closed symbols correspond to respectively the oscillation and exponential components of the fits of the MOKE data. The symbol colors indicate the results for the 20 nm (purple) and 30 nm (yellow) thick FeRh films. (a) Amplitudes of the two oscillatory parts in as a fucntion of temperature. (b) Temperature dependence of the amplitudes of the exponential rise in MOKE (open circles) and reflectivity (closed circles) with $\tau = 3$ ps.

($A_{\theta_{\max}}$) that is reached after a certain time ($\tau_{\max}$) after the pump pulse, which is plotted in Fig. 6.8(c,d). Indeed, at all experimental conditions the 20 nm film develops much higher amplitude values that are reached at times in excess of 100 ps. Instead, the MOKE amplitudes of the 30 nm film stay relatively low and their maxima are reached at delay times smaller than 100 ps, which means that no long-term growth occurs. Only, at high temperatures (250 K) and at magnetic fields of 20 T or above, some long-term dynamics is observed for this sample.

These results confirm that the behaviour of the 30 nm thick film is practically identical to that of the 40 nm film. The 20 nm film shows an entirely different response, which furthermore depends in a non-monotonic way on the temperature and field strength. For this thin sample, for all fields the maximum MOKE amplitude at 5 K is high, to reduce significantly in size at 50 K, after which it recovers to high values at temperatures above 100 K (Fig. 6.8(a)). At the same time, the MOKE signal grows with increasing magnetic field strength. A similar non-monotonic behaviour is seen for $\tau_{\max}$ (Fig. 6.8(c)). Finally, the time for the signal to return back to the baseline is longer in the 20 nm film, as follows from Panel 6.8(e,f). The recovery at low temperatures occurs much faster and completes within a nanosecond, but as the sample is heated even at 2 ns the signal did not recover to zero. At higher magnetic fields the recovery time can not be defined. Also, at higher temperatures (250 K) the transition already occurs at a lower magnetic field (10 T), and no positive signal is present.

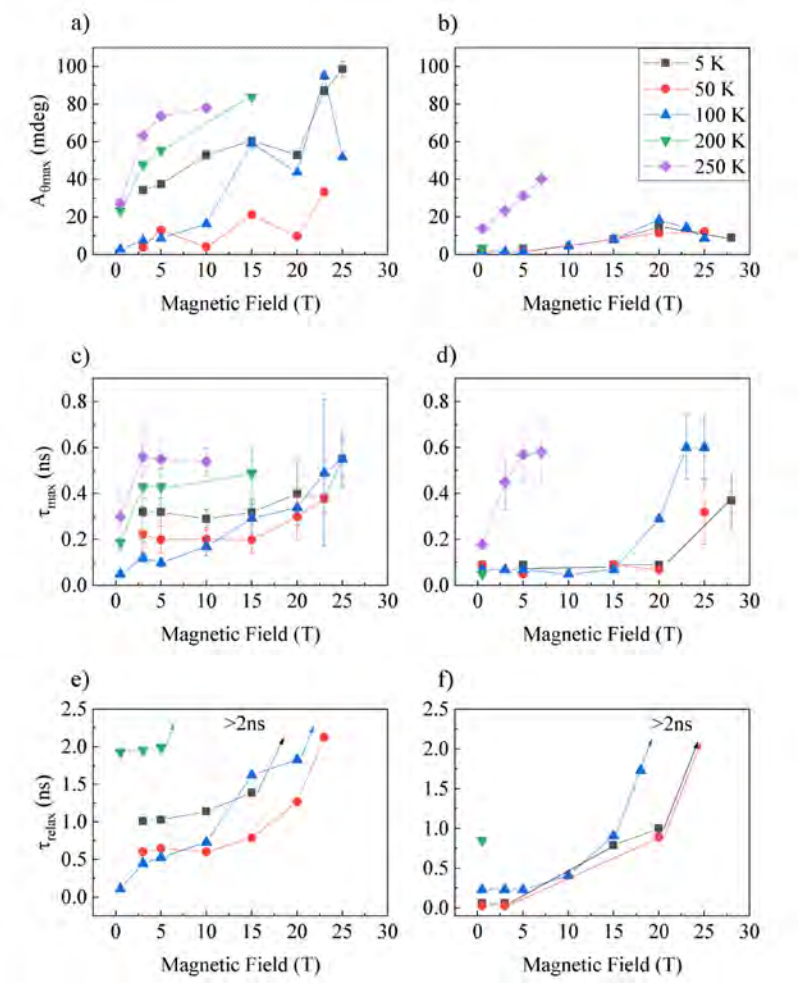

Figure 6.8: Analysis of the long-term dynamics of the MOKE signal of the 20 nm (left panel) and 30 nm (right panel) FeRh films. (a,b) The amplitude maximum reached at the indicated temperature and magnetic field strength. (c,d) Time in nanoseconds when this amplitude maximum is reached. (e, f) Time required for the signal to recover after reaching the maximum. Note: The data for the 30 nm film at 200 K is included only for a magnetic field of 0.5 T.

6.6 Discussion

Like in chapter 5, we will interpret our results in terms of the nucleation-growth model described in section 5.5 and schematically drawn in Fig. 5.8. Non-equilibrium laser heating of the FeRh film in the AFM phase induces the nucleation of the FM phase, and its subsequent growth and alignment as a function of the time delay between the pump and the probe pulses. At much longer times scale the film relaxes back to the equilibrium AFM phase. We assume that our technique is fully stroboscopic, such that the sample fully relaxes back to the AFM phase in between the consecutive laser pump pulses, allowing us to repeatedly measure the nucleation and growth of FM domains from the AFM phase after each exciting pulse.

The measured ultrafast dynamics of FeRh shows an extremely rich and complex behaviour that strongly depends on temperature and applied magnetic field, film thickness and strain, as well as on experimental details such as temperature cycling history of the sample and how the sample is mounted. The traces themselves always consist of an exponential rise (and decay) of the polar MOKE and reflectivity signal, possibly accompanied by a negative $\Delta\theta/\theta$ signal corresponding to demagnetization, oscillations, a delayed response because of latency, and a long-term growth and alignment term, all depending on the experimental and sample conditions. In addition, the reflectivity contains ultrafast transients because of the laser induced electron dynamics, i.e. the heating and cooling of the free electrons. This complexity prohibits that the time-resolved traces can be fully described at all timescales by fits, because essentially the fitting functions contain to many free parameters. Nevertheless, by looking at the raw data and how the responses depend on the external magnetic field and temperature, given the known $H - T$ phase diagram, a consistent experimental picture emerges how to understand the dynamics of the AFM-to-FM phase transition. This picture is in all cases confirmed by the results of the fitting of the ultrafast dynamics on a 20 ps timescale. In the following paragraphs we discuss the different stages of the phase transition, mainly focusing on the thickness dependence of the observations.

6.6.1 Nucleation

The nucleation step of the phase transition is found to be completed in roughly 10 ps and its characteristic timescale τ_{M} equals approximately 3 ps for all samples measured in this thesis. This nucleation phase is also observable in the reflectivity difference signal. The results on the thinner films described in the present chapter are an important experimental confirmation that the speed of the nucleation phase does not depend on the thickness of the FeRh film and its degree of strain. Furthermore, also the capping layer does not seem to play a big role, because the 20 and 30 nm thick samples studied in this chapter were capped by a 5 nm Au layer,

whereas the 40 nm thick samples of the previous chapters were capped by a 5 nm Pt layer.

6.6.2 Growth at longer timescales

The main difference between the results of the 20 and 30 nm thick FeRh films is the response at longer timescales. In this regard, the 30 nm film behaves roughly similarly to (unstrained) 40 nm films. Indeed, the oscillatory behaviour of the MOKE signal at low temperatures, the demagnetization of the FM domains in the vicinity of the phase transition boundary and the saturation of the signal after the first nuclei generation were seen also in 40 nm samples reported in Chapters 4 and 5. The 20 nm sample exhibits a similar response at short timescales but behaves differently at longer timescales, where it shows a pronounced growth of the FM phase. This behaviour has a certain similarity to the results of the 1.4% tensile strained 40 nm thick sample, reported in the previous chapter. For both samples, it turned out to be extremely difficult to disentangle the first nucleation phase from the subsequent growth and alignment process. As described in the previous paragraph, the first fast nucleation of the FM domains still occurs, but it is overwhelmed by the large signal on longer timescales.

The similarity of the results of the 20 nm FeRh layer and the 40 nm sample with high tensile strain might indicate that the thin sample accompanies some degree of tensile strain. Due to the lattice mismatch between FeRh and the MgO substrate a reduction in film thickness is expected to introduce tensile strain in the out-of-plane direction. The increase of the c lattice parameter was already measured several times with the shift of the corresponding Bragg peak. The release of the strain in that direction was also indicated to happen together with the changes in the magnetic order of FeRh[10, 19, 24]. Indeed, the magnetic characterisation using polar MOKE in section 6.3, shows that for this sample T_C and H_C are lowered with respect to a 40 nm think FeRh layer, as expected for tensile strain (see Fig. 5.1 and the results in chapter 5).

However, there are also some differences between the results of the 20 nm film and the 40 nm film with high tensile strain. First of all, the 20 nm sample does not exhibit latency in the MOKE channel and demagnetization far below the phase transition, as was seen in the 1.4% tensile strained 40 nm sample in chapter 5. The absence of latency could be the consequence of the high sensitivity to strain and layer thickness of the sign of the magnetic anisotropy in the antiferromagnetic phase [25]. When the anisotropy is in-plane, any out-of-plane external magnetic field would cant the sublattices leading to a non-collinear antiferromagnetic state, where latency is not present [26]. Secondly, the 20 nm layer also doesn't show the negative demagnetization signal that was detected in the mechanically strained 40 nm thick samples, deep in the AFM phase. The occurrence of this negative signal was attributed to the presence of defects in the layer, which might

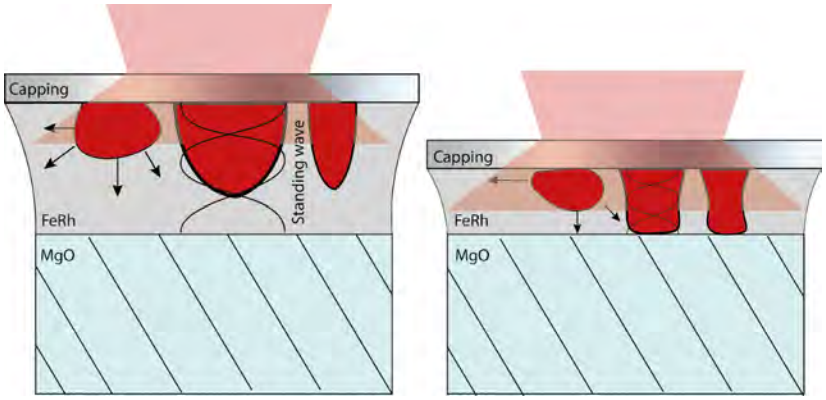

Figure 6.9: Schematic of laser pulse induced nucleation of FM domains in thick (left panel) and thin (right panel) FeRh films. When the laser penetration depth is smaller than the film thickness the domains remain at the top interface, whereas for thinner film the domains can be formed throughout the film.

stabilize FM domains in the AFM phase (see chapter 5). We expect that those defects are only present in mechanically strained samples, and are not formed in layers with a small amount of strain due to the lattice mismatch between FeRh and the MgO substrate. But clearly, based on the present data set we can not conclude to what extent (tensile) strain the 20 nm layer affects the ultrafast magnetic response, also because there might be other factors that play a dominant role.

Magnetization studies reveal the formation of FM domains preferentially at the substrate interface [18, 27, 28]. Our magnetization study shown in Figure 4.1 of chapter 4 showed a ferromagnetic response at low fields, which was attributed to the response of the atomic FeRh layers, closest to the substrate. The effect of those few atomic layers can be expected to be larger for thinner films, possibly resulting in a lowering of the phase boundary, i.e. a reduction of H_C and T_C. In addition, for thin samples ultrafast laser excitation might induce FM order throughout the entire film, a process that is schematically depicted in Figure 6.9. We anticipate that under such conditions ultrafast laser heating results in the creation of larger FM volumes and stronger signals, that are more stable and therefore last longer. Strikingly, this dynamics on longer timescales shows a peculiar temperature dependence that is discussed in the next paragraph.

6.6.3 Temperature dependence

For the 20 nm thick FeRh sample the MOKE amplitude is lowest at a temperature of 100 K (Fig. 6.3). Strikingly, with decreasing temperature

the magnetic signal significantly increases, demonstrating that a bigger FM volume is created, despite the fact that at lower temperature the system is brought further away from the phase transition. For temperatures above 100 K, the maximal MOKE amplitude increases again, but this can considered as regular behaviour, because with increasing temperature the system approaches the AFM-to-FM phase transition boundary. Indeed, for the thicker FeRh films measured, the MOKE amplitude increases with temperature until it vanishes beyond the phase transition.

The precise reason for this behaviour is currently not clear and as mentioned above it is unlikely that it can be explained by the phase diagram. A possible explanation can be found in the difference in the thermal expansion coefficients of the FeRh film [13, 29] and the MgO substrate [30]. With lattice constants of $a_{\mathrm{FeRh}} = 2.986\,\text{Å}$ [13] and $a_{\mathrm{MgO}} = 4.213\,\text{Å}$ at room temperature a mismatch arises, inducing strain at the interface [9]. This dissimilarity leads to in-plane compression and out-of-plane extension. On top of that the lattice parameter mismatch changes with temperature as $\alpha_{\mathrm{FeRh}} < \alpha_{\mathrm{MgO}}$ ($\approx 9.5 \times 10^{-6} K^{-1}$ in the AFM phase of FeRh versus $\approx 10.4 \times 10^{-6} K^{-1}$ for MgO). Given that $\sqrt{2} a_{\mathrm{FeRh}}$ exceeds a_{MgO} at room temperature, a cross-point emerges upon cooling, at which the strain undergoes a change in sign. This strain effect might be responsible for the changes in the long-term dynamics as a function of temperature. The thermal expansion coefficient of MgO lattice starts to grow linearly with temperature and becomes even larger than that of FeRh above 250 K.

As a result of the distinct thermal expansion rates of FeRh and MgO and the corresponding temperature-dependent strain levels, it is also possible that the magnetocrystalline anisotropy within the antiferromagnetic (AFM) phase varies in the different experiments. As indicated in Ref. [25], this anisotropy is sensitive to the strain imposed by the substrate. The interplay of such differences in thermal expansion, along with nonlinear behaviour near the transition, might lead to anomalous behaviour as a function of temperature. This could provide insights into the absence of latency observed in the current study even at 0.5 T, in contrast to previous observations. Nevertheless, the phase transition itself could be tracked and does not show any peculiarity around 100 K (Fig. 6.1). Usually, hysteresis in static measurements points to the co-existence of FM and AFM domains during the phase transition. In the considered thin film, the absence of a hysteresis loop in the $\theta(H)$ curve, which reflects $M(H)$ dependence, doesn't cancel out the possibility of thermal hysteresis and domain nucleation due to laser heating.

The contribution of demagnetization at 25 T indicates the existence of FM domains. The demagnetization alongside growth implies the transition occurs concurrently with domain formation, even under non-equilibrium conditions. A two-step process is evident: rapid nucleation within sub-5 ps, followed by prolonged expansion over 150 ps. FM phase emergence at

25 T is detected solely in the 20 nm sample within the short timescale, in line with our phase diagram placing FeRh close to the transition border under these conditions. However, assuming that the lowering of the critical temperature leads to the same trend of the critical field MOKE suppression at 25 T due to high demagnetization contribution in the 30 nm film contradicts previous experimental observation of reduced critical temperature with film thickness[19]. At the same time simulations from Ref. [24] demonstrate that a change of the transition temperature required to explain such changes is expected for a film thickness below 10 nm.

The proximity-induced strain gradient alteration can explain similarities observed in strain-induced and thin-film lattice waves. The observed oscillation is associated with surface-tracked parameters affected by strain propagation and lattice expansion.

6.6.4 Oscillations

The polar MOKE traces of the 20 and 30 nm thick samples show oscillatory behaviour at short timescales (see eg. the experimental traces in Fig. 6.4). We can distinguish two types of oscillations: a high frequency oscillation (period of about 6 ps) is clearly visible in the 20 nm film, barely seen in the 30 nm sample and absent in the 40 nm films. A low frequency oscillation is seen in all films measured (20, 30 and 40 nm thick) with a period of about 30 ps, independent of film thickness (fig. 6.4 and type of capping layer (Pt or Au)). Both oscillations are heavily damped. The oscillation period is independent of magnetic field strength (left panel Fig. 6.2 and Fig. 6.5). Yet, the amplitude of the oscillations increases with field strength, similar to the field behaviour of the MOKE signal, which demonstrates that the occurrence of the oscillations is directly related to the formation of the FM domains upon ultrafast laser heating. The oscillation frequencies are independent of the sample temperature (left panel Fig. 6.3), although their amplitudes decrease with increasing temperature (left panel Fig. 6.7).This is in contrast to the rise in amplitude with temperature of the MOKE signal (right panel Fig. 6.7), but the oscillations are only seen simultaneously with the FM domains. The origin of the oscillations is currently unknown. The independence of the frequency on the magnetic field strength rules out a purely magnetic origin. More likely the oscillation is related to a strain pulse upon ultrafast laser heating. Surprisingly, the period of the oscillations does not depend on the layer thickness, so we can also rule out the occurrence of a standing strain waves in between the top surface of the film and the interface with the substrate. The observation of oscillations of similar frequencies have been observed in FeRh films [6, 14, 15], using time-resolved X-Ray Diffaction experiments. Those experimental observations were explained in terms of strain waves traveling back and forth through the film with a period $T = 2d/v_s$ where d is the thickness of the film and $v_s \approx 5$ km/s ($= 5$ nm/ps) is the sound velocity [31], [32]. For our samples this type

of oscillations would lead to a sample dependent oscillation period of about 8, 12 and 16 ps. Thus, in our case the laser-induced excitation cannot be assigned to the standing waves proposed previously in literature and further theoretical work is required to understand the origin of the oscillations observed. This should occur for the conditions shown in Fig. 6.9, i.e. the local ultrafast creation of FM domains that have a different lattice constant then their environment. Possible other effects that may play a role are the internal properties of the thin FeRh films such as modification of the exchange constants due to strain [24], differences in grain size, defect distribution [10, 12, 33] or morphology [34].

6.7 Conclusions

This work demonstrates the impact of the thickness of the FeRh film on the magnetoelastic phase transition. We find that the nucleation step of the phase transition is found to be independent of the film thickness and capping layer, and is completed in roughly 10 ps with a characteristic timescale of $\tau_{\mathrm{M}} = 3$ ps. The main effect observed in thinner FeRh films is the occurrence of large magnetic signal at longer timescales up to 2 ns, with a pronounced temperature- and magnetic field dependence. This response is attributed to a higher created volume of the ferromagnetic phase, stable on longer timescales, in thinner samples. Possible causes of this effect are the presence of FM domains primarily at the FeRh/MgO interface and/or the presence of tensile strain in the film. This strain arises from the (temperature dependent) difference in lattice constants of FeRh and the MgO substrate. The significant dependence on the temperature of the long timescale dynamics strongly suggests that the main effect is the substrate induced strain, given by the difference in the thermal expansion coefficients of film and substrate. Finally, pronounced oscillations are seen in the MOKE signal, caused by laser induced strain pulses in the FeRh films. Surprisingly, the period of these pulses are found to be independent of the layer thickness, which rules out the common explanation that the oscillations are due to standing waves in the film with a period of $T = 2d/v_{\mathrm{s}}$. More experimental and theoretical work is needed to clarify the origin of the oscillations.

In summary, this study highlights the significance of film thickness and strain engineering in controlling the magnetoelastic properties of FeRh. The findings contribute to a deeper understanding of the phase transition dynamics and have implications for the design and optimization of magnetoelastic devices and materials. However, further investigations are required to fully elucidate the underlying mechanisms and to explore the potential of strain engineering in other magnetic systems.

Bibliography

[1] L. H. Lewis, C. H. Marrows, and S. Langridge, Journal of Physics D: Applied Physics **49**, 323002 (2016), ISSN 0022-3727, 1361-6463.

[2] C. Kittel, Physical Review **120**, 335 (1960), ISSN 0031-899X.

[3] A. I. Zakharov, A. M. Kadomtseva, R. Z. Levitin, and R. Z. Ponyatovskii, Soviet Physics JETP **19**, 1348 (1964).

[4] R. C. Wayne, Physical Review **170**, 523 (1968), ISSN 0031-899X.

[5] V. L. Moruzzi and P. M. Marcus, Physical Review B **46**, 2864 (1992), ISSN 0163-1829, 1095-3795.

[6] S. O. Mariager, F. Pressacco, G. Ingold, A. Caviezel, E. Möhr-Vorobeva, P. Beaud, S. L. Johnson, C. J. Milne, E. Mancini, S. Moyerman, et al., Physical Review Letters **108**, 087201 (2012), ISSN 0031-9007, 1079-7114.

[7] R. Fan, C. J. Kinane, T. R. Charlton, R. Dorner, M. Ali, M. A. de Vries, R. M. D. Brydson, C. H. Marrows, B. J. Hickey, D. A. Arena, et al., Physical Review B **82**, 184418 (2010), ISSN 1098-0121, 1550-235X.

[8] J. A. Arregi, O. Caha, and V. Uhlíř, Physical Review B **101**, 174413 (2020), ISSN 2469-9950, 2469-9969.

[9] A. Ceballos, Z. Chen, O. Schneider, C. Bordel, L.-W. Wang, and F. Hellman, Applied Physics Letters **111**, 172401 (2017), ISSN 0003-6951, 1077-3118.

[10] C. W. Barton, T. A. Ostler, D. Huskisson, C. J. Kinane, S. J. Haigh, G. Hrkac, and T. Thomson, Scientific Reports **7**, 44397 (2017), ISSN 2045-2322.

[11] I. Suzuki, T. Koike, M. Itoh, T. Taniyama, and T. Sato, Journal of Applied Physics **105**, 07E501 (2009), ISSN 0021-8979.

[12] G. C. Han, J. J. Qiu, Q. J. Yap, P. Luo, D. E. Laughlin, J. G. Zhu, T. Kanbe, and T. Shige, Journal of Applied Physics **113**, 17C107 (2013), ISSN 0021-8979, 1089-7550.

[13] L. Zsoldos, physica status solidi (b) **20**, K25 (1967), ISSN 03701972, 15213951.

[14] F. Quirin, M. Vattilana, U. Shymanovich, A.-E. El-Kamhawy, A. Tarasevitch, J. Hohlfeld, D. von der Linde, and K. Sokolowski-Tinten, Physical Review B **85**, 020103 (2012), ISSN 1098-0121, 1550-235X.

[15] M. Mattern, J. Jarecki, J. A. Arregi, V. Uhlíř, M. Rössle, and M. Bargheer, *Disentangling nucleation and domain growth during a laser-induced phase transition* (2023), 2305.02094.

[16] I. Radu, C. Stamm, N. Pontius, T. Kachel, P. Ramm, J.-U. Thiele, H. A. Dürr, and C. H. Back, Physical Review B **81**, 104415 (2010), ISSN 1098-0121, 1550-235X.

[17] M. Grimes, H. Ueda, D. Ozerov, F. Pressacco, S. Parchenko, A. Apseros, M. Scholz, Y. Kubota, T. Togashi, Y. Tanaka, et al., Scientific Reports **12**, 8584 (2022), ISSN 2045-2322.

[18] J. Hong, T. Yang, A. N'Diaye, J. Bokor, and L. You, Nanomaterials **9**, 574 (2019), ISSN 2079-4991.

[19] C. Q. Yu, H. Li, Y. M. Luo, L. Y. Zhu, Z. H. Qian, and T. J. Zhou, Physics Letters A **383**, 2424 (2019), ISSN 0375-9601.

[20] R. Medapalli, G. Li, S. K. K. Patel, R. V. Mikhaylovskiy, Th. Rasing, A. V. Kimel, and E. E. Fullerton, Applied Physics Letters **117**, 142406 (2020), ISSN 0003-6951, 1077-3118.

[21] I. A. Dolgikh, T. G. H. Blank, A. G. Buzdakov, G. Li, K. H. Prabhakara, S. K. K. Patel, R. Medapalli, E. E. Fullerton, O. V. Koplak, J. H. Mentink, et al., *Ultrafast Emergence of Ferromagnetism in Antiferromagnetic FeRh in High Magnetic Fields* (2023), 2202.03931.

[22] J. B. McKinnon, D. Melville, and E. W. Lee, Journal of Physics C: Solid State Physics **3**, S46 (1970), ISSN 0022-3719.

[23] A. Hillion, A. Cavallin, S. Vlaic, A. Tamion, F. Tournus, G. Khadra, J. Dreiser, C. Piamonteze, F. Nolting, S. Rusponi, et al., Physical Review Letters **110**, 087207 (2013).

[24] T. A. Ostler, C. Barton, T. Thomson, and G. Hrkac, Physical Review B **95**, 064415 (2017), ISSN 2469-9950, 2469-9969.

[25] C. Bordel, J. Juraszek, D. W. Cooke, C. Baldasseroni, S. Mankovsky, J. Minár, H. Ebert, S. Moyerman, E. E. Fullerton, and F. Hellman, Physical Review Letters **109**, 117201 (2012), ISSN 0031-9007, 1079-7114.

[26] A. G. Buzdakov, I. A. Dolgikh, K. A. Zvezdin, A. K. Zvezdin, K. Rubi, U. Zeitler, P. C. M. Christianen, Th. Rasing, S. K. K. Patel, R. Medapalli, et al., Physical Review B **108**, 184420 (2023).

[27] T. P. Almeida, D. McGrouther, R. Temple, J. Massey, Y. Li, T. Moore, C. H. Marrows, and S. McVitie, Physical Review Materials **4**, 034410 (2020).

[28] W. Griggs, B. Eggert, M. O. Liedke, M. Butterling, A. Wagner, U. Kentsch, E. Hirschmann, M. Grimes, A. J. Caruana, C. Kinane, et al., APL Materials **8** (2020).

[29] M. R. Ibarra and P. A. Algarabel, Physical Review B **50**, 4196 (1994).

[30] D. K. Smith and H. R. Leider, Journal of Applied Crystallography **1**, 246 (1968), ISSN 0021-8898.

[31] J. A. Ricodeau and D. Melville, Journal of Physics F: Metal Physics **2**, 337 (1972), ISSN 0305-4608.

[32] S. B. Palmer, P. Dentschuk, and D. Melville, physica status solidi (a) **32**, 503 (1975), ISSN 1521-396X.

[33] L. Benito, L. Clark, T. P. Almeida, T. A. Moore, D. McGrouther, S. McVitie, and C. H. Marrows, Physical Review Materials **4**, 123402 (2020).

[34] J. L. Warren, C. W. Barton, C. Bull, and T. Thomson, Scientific Reports **10**, 4030 (2020), ISSN 2045-2322.

Summary

Fundamental interest in spin dynamics in magnetic materials has long been driven by the ever-increasing demands of modern information technology for faster magnetic data writing and processing. The development of ultrafast lasers and pump-probe techniques has enabled investigations into regimes where the timescales of the observed processes align with those of fundamental interactions responsible for the very existence of magnetic order.

The pioneering demonstration of ultrafast laser-induced demagnetization of ferromagnetic Ni, which initiated the field of ultrafast magnetism nearly 30 years ago, has since been complemented by many experimental observations, that challenge state-of-the-art theories in magnetism. Among the most appealing and fundamentally intriguing phenomena in ultrafast magnetism are the discoveries of the fastest-ever laser-induced spin reorientation, ultrafast inverse Faraday and all-optical switching. Remarkably, all these phenomena were observed in materials with an antiferromagnetic coupling, such as ferri - and antiferromagnets.

For a deeper understanding of ultrafast spin dynamics in ferri- and antiferromagnets, the role of high magnetic fields can't be ignored. This tool allows us to explore ultrafast magnetism across the extensive $H - T$ phase diagram of these materials. In this thesis, we benefit from the unique installation at HFML-FELIX allowing us to perform time-resolved measurements with femtosecond temporal resolution at record-high magnetic fields up to 38 T.

In particular, this work examines ultrafast magnetism under high magnetic fields. Using femtosecond laser pulses as ultrafast heaters we rapidly elevate the temperature of ferrimagnetic iron garnet across its compensation temperature and antiferromagnetic FeRh across its transition temperature to the ferromagnetic state. In both cases, such rapid heating triggers ultrafast spin dynamics, analysed as a function of an applied magnetic field and temperature.

Our experiments consistently reveal the common feature of ultrafast magnetism in ferri- and antiferromagnetic materials: spins in a collinear phase are significantly less susceptible to laser-induced heating. Even when in non-eqilibrium states, that do not correspond to a thermodynamic minimum, these spins only reorient towards the equilibrium after a consider-

able delay compared to their non-collinear initial arrangements. The delay is given by the timescale at which spins, through fluctuations, acquire a canted configuration. This characteristic timescale is defined by the spin-lattice interaction at the center of the Brillouin zone and can extend up to several ns, as is observed in iron garnet.

At the same time, spin dynamics in materials with canted spins are not limited by these constraints, enabling the observation of the fastest possible spin reorientation from the antiferromagnetic to the ferromagnetic phase in FeRh. The timescale of spin reorientation appears to be in the same ballpark as the lattice expansion accompanying the phase transition from antiferromagnetic to ferromagnetic phase. Hence, our experiments suggest that during this phase transition, spin and lattice degrees of freedom evolve in step with one another.

Moreover, we studied strain effects on the laser-induced phase dynamics in FeRh. External mechanical strain, either tensile or compressive, influenced the dynamics by altering the volume of the induced ferromagnetic nuclei. Tensile strain supported the phase transition but with longer stabilization times. Strain also redistributed defects, generating ferromagnetic domains at low temperatures and magnetic fields below the transition. Tensile strain introduced latency in the response, decreasing with increased strain, indicating a higher spin flop field. Compression induced oscillations in both the lattice and magnetic systems, paralleling magnetization growth, but strain did not affect the speed of ferromagnetic nucleation.

Furthermore, our study showcased how strain engineering significantly impacted magnetoelastic phase transitions in FeRh. External strain and reduced sample thickness influence the magnetic behaviour. The observed acceleration of magnetization emergence was attributed to internal properties rather than external factors. Overall, this work demonstrates that by manipulating the studied parameters, it is possible to finetune the phase transition temperature, control the amount of generated phase volume, and stabilize the new state. However, further research in other magnetic systems is required to define the other unique properties able to accelerate the spin dynamics.

6.7.1 Outlook

Our study acknowledges the need for further investigations to fully comprehend the underlying mechanisms of phase transitions similar to the one in FeRh. Future research can delve deeper into the specific factors influencing strain-induced magnetization dynamics and explore their applicability in diverse magnetic systems. Additionally, exploring the potential of strain engineering in other magnetic materials remains an exciting avenue for research.

Generally, more parameters in FeRh system can influence the way this phase transition takes place that we haven't considered. Particularly, it

is still unclear what role the change in anisotropy can have on the spin dynamics during the transition. The theoretical predictions of the existence of such a change haven't been fully validated experimentally. In this work, we considered a single-crystal FeRh alloy. However, more easily achievable polycrystalline structure and the morphology variation may significantly impact the transition. Also, not only the reduced thickness can lead to the shift in transition temperature and stabilization of the FM phase, but nanofabrication as well. All questions related to the size and shape of the nanostructures that are important for the AFM-to-FM phase transition in equilibrium are still open for the time-resolved magnetization dynamics.

The current thesis considers mainly dissipative ways of triggering phase transitions and spin reorientations. The heating energy of the laser pulse is used to elevate temperature, which stabilizes the alternative magnetic state. The possibility of non-dissipative ways such as coherent phonon excitation or inverse effects to trigger these processes hasn't been explored. Their interconnection and the underlying mechanism of the magnetocrystalline phase transition in FeRh remain unresolved.

The findings in laser-induced dynamics in canted antiferromagnets could inspire the design of faster and more efficient spintronic devices, contributing to the development of high-speed data processing and storage technologies. Precise control of the spin orientation is essential for the development of high-speed spintronic devices. Canted antiferromagnets introduce faster switching speeds as was partially demonstrated in this thesis. In addition, there is less energy dissipation compared to traditional magnetic materials as the energy directly goes to trigger the reorientation rather than all sorts of fluctuations.

Samenvatting

Fundamentele interesse in spindynamica in magnetische materialen wordt al lange tijd gedreven door de steeds hogere eisen van de moderne informatietechnologie voor het sneller schrijven en verwerken van magnetische gegevens. De ontwikkeling van ultrasnelle lasers en pump-probe technieken heeft onderzoek mogelijk gemaakt naar regimes waar de tijdschalen van de waargenomen processen overeenkomen met die van fundamentele interacties die verantwoordelijk zijn voor het bestaan van magnetische orde.

De baanbrekende demonstratie van ultrasnelle lasergeïnduceerde demagnetisatie van ferromagnetisch nikkel, die bijna 30 jaar geleden de aanzet gaf tot ultrasnel magnetisme, is sindsdien aangevuld met vele experimentele waarnemingen die de allernieuwste theorieën over magnetisme uitdagen. Tot de meest aansprekende en fundamenteel intrigerende verschijnselen in het ultrasnelle magnetisme behoren de ontdekking van de snelste lasergeïnduceerde spinreoriëntatie ooit, ultrasnelle omgekeerde Faraday en volledig optisch schakelen. Opmerkelijk is dat al deze verschijnselen zijn waargenomen in materialen met een antiferromagnetische koppeling, zoals ferri- en antiferromagneten.

Voor een beter begrip van ultrasnelle spindynamica in ferri- en antiferromagneten kan de rol van hoge magneetvelden niet worden genegeerd. Dit hulpmiddel stelt ons in staat om het ultrasnelle magnetisme in het uitgebreide $H - T$ fasediagram van deze materialen te onderzoeken. In dit proefschrift profiteren we van de unieke installatie op HFML-FELIX die ons in staat stelt tijdgeresolveerde metingen uit te voeren met een temporele resolutie van femtoseconden bij recordhoge magneetvelden tot 38 T.

Dit werk onderzoekt in het bijzonder ultrasnel magnetisme onder hoge magnetische velden. Met behulp van femtoseconde laserpulsen als ultrasnelle verwarmers verhogen we snel de temperatuur van ferrimagnetisch ijzergranaat over zijn compensatietemperatuur en antiferromagnetisch FeRh over zijn overgangstemperatuur naar de ferromagnetische toestand. In beide gevallen veroorzaakt zo'n snelle verhitting ultrasnelle spindynamica, geanalyseerd als functie van een toegepast magnetisch veld en temperatuur.

Onze experimenten onthullen consistent het gemeenschappelijke kenmerk van ultrasnel magnetisme in ferri- en antiferromagnetische materialen: spins in een collineaire fase zijn aanzienlijk minder gevoelig voor lasergeïnduceerde verhitting. Zelfs in niet-evenwichtstoestanden, die niet

overeenkomen met een thermodynamisch minimum, heroriënteren deze spins zich pas na een aanzienlijke vertraging ten opzichte van hun niet-collineaire beginopstellingen. De vertraging wordt gegeven door de tijdschaal waarop de spins door fluctuaties een gekantelde configuratie verwerven. Deze karakteristieke tijdschaal wordt bepaald door de spin-roosterinteractie in het centrum van de Brillouinzone en kan oplopen tot enkele ns, zoals wordt waargenomen in ijzergranaat.

Tegelijkertijd wordt de spindynamica in materialen met gekantelde spins niet beperkt door deze beperkingen, waardoor de snelst mogelijke spinreoriëntatie van de antiferromagnetische naar de ferromagnetische fase in FeRh kan worden waargenomen. De tijdschaal van spinreoriëntatie blijkt in dezelfde buurt te liggen als de roosteruitzetting die gepaard gaat met de faseovergang van de antiferromagnetische naar de ferromagnetische fase. Onze experimenten suggereren dus dat tijdens deze faseovergang de spin- en roostervrijheidsgraden gelijke tred met elkaar houden.

Bovendien bestudeerden we vervormingseffecten op de lasergeïnduceerde fasedynamica in FeRh. Externe mechanische rek, trekkend of drukkend, beïnvloedde de dynamica door het volume van de geïnduceerde ferromagnetische kernen te veranderen. Trekspanning ondersteunde de faseovergang, maar met langere stabilisatietijden. Trek herverdeelde ook defecten, waardoor ferromagnetische domeinen ontstonden bij lage temperaturen en magnetische velden onder de overgang. Trekrek introduceerde latentie in de respons, die afnam met toenemende rek, wat duidt op een hoger spinflopveld. Compressie induceerde oscillaties in zowel het rooster als het magnetische systeem, parallel aan de magnetisatiegroei, maar rek had geen invloed op de snelheid van ferromagnetische nucleatie.

Verder liet onze studie zien hoe vervorming een significante invloed had op magneto-elastische faseovergangen in FeRh. Externe rek en gereduceerde dikte van het monster beïnvloeden het magnetische gedrag.

De waargenomen versnelling van het ontstaan van magnetisatie werd toegeschreven aan interne eigenschappen in plaats van externe factoren. In het algemeen toont dit werk aan dat het door het manipuleren van de bestudeerde parameters mogelijk is om de temperatuur van de faseovergang nauwkeurig af te stellen, de hoeveelheid gegenereerd fasevolume te regelen en de nieuwe toestand te stabiliseren. Verder onderzoek in andere magnetische systemen is echter nodig om de andere unieke eigenschappen te bepalen die de spindynamica kunnen versnellen.

Research Data Management

This thesis research has been caried out in accordance with the research data management policy of the High Field Magnet Laboratory and FELIX Laboratory (HFML-FELIX) of Radboud University, the Netherlands[1]. Data sets for the results presented in this thesis are deposited in the Radboud Data Repository as a data sharing collection with the unique digital object identifier (DOI) 10.34973/te74-2122. It can be accessed via https://doi.org/10.34973/te74-2122 upon request to the promotor or the HFML-FELIX data steward.

[1] http://www.ru.nl/rdm/vm/policy-documents/policy-imm/

List of Publications

[1] **I. A. Dolgikh**, K. Mikhuti, S. K. K. Patel, R. Medapalli, E. E. Fullerton, P. C. M. Christianen, and A. V. Kimel, "Ultrafast dynamics of the antiferromagnetic to ferromagnetic phase transition in strained ferh films," (in preparation).

[2] **I. A. Dolgikh**, K. Mikhuti, S. K. K. Patel, R. Medapalli, E. E. Fullerton, P. C. M. Christianen, and A. V. Kimel, "Thickness dependence of the ultrafast magnetostructural phase transition in ferh," (in preparation).

[3] **I. A. Dolgikh**, T. G. H. Blank, A. G. Buzdakov, G. Li, K. H. Prabhakara, S. K. K. Patel, R. Medapalli, E. E. Fullerton, O. V. Koplak, J. H. Mentink, K. A. Zvezdin, A. K. Zvezdin, P. C. M. Christianen, and A. V. Kimel, "Ultrafast emergence of ferromagnetism in antiferromagnetic ferh in high magnetic fields," ArXiv (2023), 10.48550/arXiv.2202.03931.

[4] A. Buzdakov, **I. A. Dolgikh**, K. A. Zvezdin, A. K. Zvezdin, K. Rubi, U. Zeitler, P. C. M. Christianen, Th. Rasing, S. K. K. Patel, R. Medapalli, E. E. Fullerton, E. T. Dilmieva, and A. V. Kimel, "Phase diagrams for magnetic field and temperature induced ferromagnetism in antiferromagnetic ferh," Physical Review B **108**, 184420 (2023).

[5] **I. A. Dolgikh**, F. Formisano, K. H. Prabhakara, M. V. Logunov, A. K. Zvezdin, P. C. M. Christianen, and A. V. Kimel, "Spin dynamics driven by ultrafast laser-induced heating of iron garnet in high magnetic fields," Applied Physics Letters **120**, 012401 (2022).

Curriculum Vitae

Name: Irina Alexeevna Dolgikh
Date of birth: 03/05/1994
Nationality: Russian
E-mail: irinadolgikh94@gmail.com

2018 – 2023 PhD in Physics,
FOM/Radboud University Nijmegen

2016 – 2018 MSc in Physics
Moscow, Moscow State University

2012 – 2016 BSc in Physics
Moscow, Moscow State University

2005 – 2012 School
Gymnasium №26, Naberezhnie Chelny, Tatarstan, Russian Federation

2001 – 2005 School
Gymnasium №94, Kazan, Tatarstan, Russian Federation